THE DESIGN OF VASCULAR-TARGETED CARRIERS FOR ENHANCED INTERACTIONS WITH DISEASED ENDOTHELIUM VIA BLOOD FLOW

by

Alex J. Thompson

A dissertation submitted in partial fulfillment
of the requirements for the degree of
Doctor of Philosophy
(Chemical Engineering)
in The University of Michigan
2015

Doctoral Committee:

Associate Professor Omolola Eniola-Adefeso, Chair
Professor Joseph L. Bull
Professor Erdogan Gulari
Assistant Professor Sunitha Nagrath

To my family and friends

Thanks for all the love, support, laughs, and good times

ACKNOWLEDGMENTS

First and foremost, I offer my sincerest thanks to my advisor, Professor Omolola Eniola-Adefeso, for having me as a member in her research lab throughout my time as a graduate student. Working with Lola has been a great experience that has allowed me to grow as a researcher and professional, and my time as a graduate student would not have been as enjoyable had I not been in her lab. I look forward to seeing the great research that is produced from her lab in the future.

I would like to thank Professor Joe Bull, Professor Sunitha Nagrath, and Professor Erdogan Gulari for serving as members of my defense committee, and for their insights which have allowed me to produce this work. I wish them all continued success in the future, and given their accomplishments that is a wish likely to be fulfilled.

Thanks to all the past and current members of the Eniola Lab. Ryan Huang, Mike Heslinga, Ploy Charoenphol, Supriya Mocherla – thanks so much for your guidance during my first few years of graduate work, it was a pleasure working with all of you. Peter Onyskiw, Katawut Namdee, Daniel Sobczynski, Margaret Fish, Mariana Carrasco-Teja, Ted Zaroff III, and the many others I've been able to work with – I've thoroughly enjoyed working with all of you, thanks so much for making the lab a fun place to work.

Special thanks to all my close friends that I've met and spent some very fun times with as a graduate student. I'm thankful to have so many great memories and great friends to take away

from Ann Arbor. I know the future holds many more fun times and great memories for all of us.

Finally, thanks to my family for all the love and support over the years. I hope you know how much it has always meant to me.

TABLE OF CONTENTS

LIST OF TABLES

LIST OF FIGURES

LIST OF EQUATIONS

LIST OF ABBREVIATIONS

AR	Aspect ratio
CFL	Cell-free layer
CAD	Coronary artery disease
CSR	Critical shear rate
EC	Endothelial cell
EPR	Enhanced permeability and retention
ESD	Equivalent spherical diameter
Hct	Hematocrit
HUVEC	Human umbilical vein endothelial cell
PPFC	Parallel plate flow chamber
PS	Polystyrene
RBC	Red blood cell
RES	Reticuloendothelial system
Si	Silica
Ti	Titania
VTC	Vascular-targeted carrier
WSR	Wall shear rate

ABSTRACT

THE DESIGN OF VASCULAR-TARGETED CARRIERS FOR ENHANCED INTERACTIONS WITH DISEASED ENDOTHELIUM FROM BLOOD FLOW

by

Alex J. Thompson

Chair: Omolola Eniola-Adefeso

Particulate carriers proposed for use in vascular-targeting are typically spherical and on the nanometer to sub-micron scale. However, spherical nanoparticles do not efficiently marginate, or localize to the cell-free layer (CFL), in blood flow making them sub-optimal as vascular-targeted carriers. Microspheres with diameter ≥ 2 μm are able to efficiently marginate in the presence of blood, however may present issues in navigating the vasculature or in adhering in the presence of high shear forces. Here, we investigate how physical design parameters in addition to particle size, namely particle shape and density, affect the efficacy of vascular-targeted carriers (VTC) both *in vitro* and *in vivo*.

We find that particle shape and density both affect the ability of microparticles to adhere to inflamed endothelium from blood flow. Rod and disk-shaped particles display improved adhesion *in vitro* to endothelium compared to equivalent spheres, provided the aspect ratio is

sufficiently high and the equivalent spherical diameter (ESD) is ≥ 1 μm. These effects were confirmed *in vivo*, as targeted 2 μm ESD rods bound to the aorta of atherosclerotic mice at levels ~3 times higher than equivalent spheres, while 500 nm rods and spheres displayed minimal adhesion. We also find that particle density affects the ability of nanoparticles (500 nm diameter) to target inflamed endothelium. Silica spheres (2.0 g/cm^3) adhered to inflamed endothelium *in vitro* at consistently higher levels than either polystyrene (1.05 g/cm^3) or titania (3.9 g/cm^3) spheres, while titania spheres only display improved adhesion when external forces (such as gravity, centrifugal force) also favor adhesion. Particle density also affected the adhesion profile along the aorta of mice with systemic inflammation, with silica spheres displaying the most adhesion. Overall this work shows that particle shape and density are design parameters which should be considered to optimize the performance of vascular-targeted carriers.

CHAPTER 1: INTRODUCTION

1.1 Background

Systemic administration of therapeutics via the vasculature is an excellent route for drug delivery as it provides relatively non-invasive access to essentially anywhere in the body; however, traditional free-drug administration is quite inefficient and inherently flawed for a number of reasons. First and foremost, drugs administered in this manner are distributed throughout the vasculature, even to healthy tissues, which can cause severe side effects particularly for highly potent therapeutics (e.g. chemotherapy), limiting the dosage that can safely be administered. Also, the drug is vulnerable to the body's innate immune response, subjecting the drug to clearance/degradation, limiting the maximum potential effect from the dose. Bolus injections of drugs also present issues in terms of keeping the drug within the therapeutic window for an extended period of time, therefore requiring multiple subsequent dosages whereas the controlled release of a single drug administration would be more favorable.

1.1.1 Vascular Targeting

Vascular targeting is an emerging drug delivery strategy that holds vast possibilities for improving the diagnosis and treatment of many human diseases.[1,2] Vascular targeting seeks to mitigate the issues associated with free-drug administration and maximize the therapeutic or diagnostic effect by providing highly localized, highly site-specific delivery. Localized delivery is desirable in that it can reduce the delivery of potent therapeutics or imaging agents to

unwanted areas of the body and maximize delivery to the intended site, minimizing harsh side effects and improving imaging/therapeutic effects, while still utilizing the vasculature as the route for delivery. Often, vascular targeting is coupled with particulate drug delivery systems,[3] in which drugs are encapsulated or conjugated to drug delivery "vehicles" on the nanometer or micron scale, which can protect the active drug/imaging cargo from premature degradation and offers opportunity to engineer the controlled release of therapeutics for sustained or site-specific drug delivery.[4] The potential for minimizing side effects while also improving the effectiveness and longevity of injected therapeutics makes the development of vascular-targeted carriers (VTC) an exciting area of research for new disease treatment options.

1.1.1.1 Active versus Passive Targeting

The effectiveness of vascular targeting hinges on the ability of the carrier to navigate the vasculature and be able to specifically accumulate in the targeted area of the body. This can be achieved in a variety of ways, however the strategies can typically be defined as either *passive* or *active* targeting. Passive targeting relies on the physical characteristics of the carrier and physiology of the target environment to achieve localized delivery. A good example of this is in targeting to tumors via the "enhanced permeability and retention" (EPR) effect, in which the rapid formation of new vasculature in tumors results in abnormally large fenestrations between endothelial cells in these areas (among other abnormalities such as improper lymphatic drainage).[5,6] Injected carriers in the size range of tens to hundreds of nanometers can diffuse through these fenestrations to preferentially accumulate in these tumors, while healthy endothelium prevents such carriers from accumulating in healthy tissues, resulting in a preferential accumulation of the carrier (and thus the drug/diagnostic) in the tumor tissue. Another example of passive targeting would be to use relatively large particles (on the order of

tens of microns in diameter) to specifically accumulate in smaller vessels (such as lung capillaries) through which particles cannot physically navigate, or to inject particles which readily accumulate in a specific organs.[7,8] Active targeting on the other hand, relies on the specific interaction between ligands and receptors to produce the desired localized delivery.[9] Often, disease pathologies are accompanied by an overexpression of surface-bound receptors either not present or present in low levels on healthy cells. By coating the surface of the vascular-targeted carrier with ligands which specifically interact with these overexpressed receptors, a carrier can circulate the vasculature until it "recognizes" the target receptor, allowing molecular interaction between ligand and targeted receptor to occur resulting in site-specific accumulation of the cargo. A good example of an active targeting strategy can also be employed to target solid tumors. Tumor vasculature is known to be characterized by rapid new vessel formation, or angiogenesis. Vascular endothelial growth factor, or VEGF, is an endothelial expressed receptor which triggers angiogenesis is overexpressed in cancer vasculature for this reason. Vascular-targeted carriers coated with a ligand to VEGF can recognize and adhere to overexpressed VEGF, resulting in specific accumulation to tumor vasculature. Whether utilizing passive or active targeting, the optimization of vascular-targeted carrier strategies holds potential to vastly improve the treatment and diagnosis of many diseases accessible via the vasculature.

1.1.2 Opportunities in Vascular-Targeting

Active targeting can be applied to treat a plethora of diseases, given that appropriate target receptors associated with the disease pathology are identified. Active targeting has been widely investigated for improving the treatment and imaging in cancer.[10–12] A variety of molecular targets have been identified which are associated with overactive processes present in cancer pathology (such as angiogenesis and cell proliferation), as well as targets expressed by

specific types of cancers.[9,13] Likewise, a wide variety of targeting moieties, including specific antibodies, peptides, proteins, and small molecules have been identified for potential use in drug targeting. Multiple antibody-based target cancer therapies have been approved by the FDA[14], and the further development of drug carrier systems using these targeting molecules hold promise in improving therapeutic effects while decreasing side effects.[15]

Active targeting strategies are also of particular interest for improving the treatment and early detection of cardiovascular diseases[4,16], which remains the leading cause of death in the western world.[17] Cardiovascular disease is typically caused by atherosclerosis, a narrowing of the arteries via a buildup of plaque in the vessel intima. Atherosclerosis is a chronic inflammatory disease, in which chronic inflammation continually elicits an immune response locally in specific areas of the vasculature which actually aids in the progression of the disease. This chronic inflammation is characterized by the overexpression of inflammatory receptors by endothelial cells in the afflicted area. These inflammatory receptors which include selectins (P and E), VCAM-1, ICAM-1, recruit circulating leukocytes from blood flow which transmigrate across the endothelium and differentiate into macrophages and eventually foam cells, aiding in plaque growth. However, the inflammatory receptors also provide a convenient platform for active targeting. By coating particles with ligands to these inflammatory markers, localized delivery of therapeutics or imaging agents for early detection can be achieved.

Regardless of the ligand/receptor pair identified for targeting, a wide variety of carrier types can be employed to deliver the intended cargo. This provides the opportunity for the design and engineering of carriers to optimize their ability to successfully target diseased cells or tissues.

1.2 Challenges in Vascular-Targeted Carrier Design

There are many important obstacles/challenges that must be considered when designing VTCs. Carriers administered intravenously face barriers associated with the body's immune system, such as plasma protein absorption, phagocytosis, and clearance from the bloodstream which an effective carrier system must be able to overcome to reach the target site.[15,18] One interesting challenge in carrier design lies in the fact that carriers must be able to efficiently "marginate" or localize to the endothelium in order to interact with the target receptors. The benefit of a highly specific ligand/receptor targeting system is diminished if the particle never interacts with the target because deposition to the target endothelium from blood flow is sub-optimal. This issue is of particular concern for targeting diseases such as atherosclerosis which affect medium/large blood vessels, where the vessel diameter may be orders of magnitude greater than the size of the individual carrier. Further, the interaction between ligands on the particle and surface receptors must be strong enough to overcome the shear force and momentum on the particle imparted by blood flow in order to result in firm adhesion. These phenomena should be considered when designing vascular-targeted carrier systems.

1.2.1 Particle Margination

It is well known that leukocytes and platelets are able to rapidly and efficiently traffic to inflamed endothelium in part because they are able to marginate very effectively, aided by their interactions with red blood cells in flow.[19–22] Red blood cells tend to move toward the center of the vessel in blood flow, forcing white blood cells and platelets to congregate in what is known as the "cell-free layer" adjacent to the endothelium. This combined effect is due in part to the difference RBC membrane and leukocyte flexibility, of WBCs, RBC hematocrit, shear, and the size of the WBCs and platelets.[21,23–26]

This "forced margination" has also been shown to occur for rigid particles, which is of interest in vascular-targeted carrier design. For spherical particles, RBC induced margination has been shown to be a function of particle size. In the presence of RBCs, particles having diameters $\geq$ 2 μm tend to concentrated to the periphery of flow, whereas particles in the nanometer or sub-micron diameter range tend to reside in the RBC rich core away from the vessel periphery.[27–30] This presents a design problem for VTCs, which traditionally have been design as spherical particles with diameters in the nanometer to sub-micron range. This size range is advantageous in that these particles can easily navigate microvasculature and experience lower shear forces upon adhesion, however the inability to marginate effectively in the presence of RBCs limits the potential of targeted nanospheres as drug carriers.

1.2.2 Particle Adhesion

Once a targeted carrier has localized to the endothelium, the interactions between ligand/receptors must be strong enough to overcome the shear removal forces imparted by blood flow. The magnitude of this shear removal force increases with particle diameter, thus also must be considered in the design of VTCs. Previous work has shown that there exists a "critical shear rate" (CSR) for particles in blood flow, above which the momentum/shear removal force is sufficient to prevent particles from binding to the endothelium.[27] This CSR is particularly limiting once particles have diameters on the micron scale, providing an upper size limit restriction on VTC design.

1.2.3 VTC Design Parameters

To date, particle size has been shown to be an important consideration in designing VTCs. Particles which are too large are limited by their ability to safely navigate microvasculature, as well as their inability to adhere to endothelium in the presence of high shear forces. Particles

which are too small are limited by their inability to effectively marginate to the endothelium, thus making them sub-optimal for vascular targeting. Recently, researchers have found that other carrier design parameters in addition to size, such as particle shape, density and deformability/rigidity may affect carrier performance.[31–33]

1.2.3.1 Particle Shape

Particle shape has been of particular focus in VTC design, as the advent of new fabrication techniques has allowed for the precise design of non-spherical particles.[34,35] The use of non-spherical particles has been of interest for a number of reasons. Elongated particles in shear flow close to a wall have been predicted *in silico* to experience a lateral drift velocity toward the wall, allowing particles to cross streamlines and contact the wall more often than spherical particles.[36,37] It is hypothesized that this effect could result in increased localization/adhesion of non-spherical VTCs compared to traditional spherical particles. Also, non-spherical particles with an elongated shape inherently have advantage over spherical particles in that they can present more targeting ligands over a larger contact surface area than equivalent spheres, potentially providing a stronger adhesion to withstand shear forces.[38] Particles with a streamlined shape can also be employed, reducing the shear removal force felt by a particle in blood flow. Early experimental evidence suggests that indeed shape can be used to improve adhesion in the presence of shear forces, though these experiments do not take into account interactions with RBCs, which are known to have major effects on the margination and adhesion of particles and cells in flow.[32,39] In addition, shape has been shown to affect the ability of phagocytes to successfully engulf particles, which may have an effect on the circulation time of an injected VTC.[40,41] Thus, one focus of this work is to elucidate the effect that particle shape

(coupled with size) has on the targeting affinity of vascular-targeted carriers in blood flow, both *in vitro* and *in vivo*.

1.2.3.2 Particle Density

Another physical parameter to be explored is particle density, which can be altered depending on the material makeup of the carrier system being employed. To date, materials with a range of densities have been proposed for use in drug delivery or diagnostics, including microbubbles[42,43], polymers[44–47], liposomes[48,49], inorganic particles (titania, gold, iron oxide)[50,51], blood cells[52,53], or combinations of multiple material types[54–56]. Yet, there is limited understanding of the role that density plays in prescribing carrier performance relating to their margination and vascular wall adhesion. Particle density forces seemingly could be regarded as negligible in describing particle motion relevant to physiological blood flow, since the hydrodynamic forces due to flow (for microparticles) and Brownian forces (for nanoparticles) are often orders of magnitude higher than density-dependent body forces such as gravitational and centrifugal forces.[57,58] However, the distance that a particle must travel in the normal direction to the endothelium to initiate contact may also be orders of magnitude shorter than the distance the particle travels in the transverse direction. This is particularly true for particles already localized to the cell-free layer (CFL) which forms adjacent to the endothelium and has a height of only a few micrometers.[19] A recent study suggests that particle density negatively affects the margination of nanoparticles in microchannel buffer flow, however, the effects of particle interactions with RBCs is not taken into account.[32] Thus, the second major focus of this work is to investigate drug carriers of various particle densities, to elucidate the effect that particle density has on the localization and adhesion of targeted particles to inflamed endothelium from blood flow, *in vitro* and *in vivo*.

1.3 Dissertation Focus and Outline

The focus of this work is in the design of vascular-targeted carriers, including identifying how the physical characteristics of the carrier (such as size, shape, density, and material) can be engineered to optimize carrier targeting performance.

Chapter 1 gives the introduction to vascular targeting, the challenges and opportunities for improved design of vascular-targeted carriers, and the general focus and outline of this dissertation.

Chapter 2 provides the detailed materials and methods used to gather the experimental data described in this dissertation.

Chapter 3 provides experimental analysis exploring the effect that particle shape has on the ability of vascular-targeted carriers to bind to inflamed endothelium using an *in vitro* model of human vasculature. The margination and adhesion of spherical and ellipsoidal particles with particle sizes ranging from 500 nm equivalent spherical diameter (ESD) and aspect ratios ranging from 1 to 11 are explored in a variety of simple and complex blood flow profiles.

Chapter 4 provides experimental analysis exploring the effect of particle shape on vascular targeting using an *in vivo* mouse model of atherosclerosis. This chapter is a collaborative project with Katawut Namdee, and the work presented is published in a co-authored paper in *Atherosclerosis* journal.[59] Dual-targeted spherical and prolate ellipsoidal particles with equivalent spherical diameters ranging from 500 nm to 2 μm having aspect ratios ranging from 1 (sphere) to 9 are injected into atherosclerotic mice, and the ability to target the aorta as well as the biodistribution to major organs is quantified.

Chapter 5 employs an *in vitro* model of human vasculature to test the effect that particle density has on the margination and adhesion to inflamed endothelium in the presence of red blood cells. The targeting ability of polystyrene, silica, and titania spheres with 500 nm diameter but with varied densities are investigated.

Chapter 6 employs an *in vivo* mouse model of systemic inflammation to test how particles of different material (polystyrene, silica, and titania) and density adhere to inflamed aorta and accumulate within major organs.

Chapter 7 provides future directions and outlook in the field of vascular-targeted carrier design based on the conclusions drawn from the work described in this dissertation as well as the current literature.

References

1. Hajitou, A., Pasqualini, R. & Arap, W. Vascular targeting: Recent advances and therapeutic perspectives. *Trends Cardiovasc. Med.* **16,** 80–88 (2006).

2. Gupta, A. Sen. Nanomedicine approaches in vascular disease: A review. *Nanomedicine Nanotechnology, Biol. Med.* **7,** 763–779 (2011).

3. Kohane, D. S. Microparticles and nanoparticles for drug delivery. *Biotechnol. Bioeng.* **96,** 203–209 (2007).

4. Ding, B.-S., Dziubla, T., Shuvaev, V. V, Muro, S. & Muzykantov, V. R. Advanced drug delivery systems that target the vascular endothelium. *Mol. Interv.* **6,** 98–112 (2006).

5. Greish, K. Enhanced permeability and retention (EPR) effect for anticancer nanomedicine drug targeting. *Methods Mol. Biol.* **624,** 25–37 (2010).

6. Iyer, A. K., Khaled, G., Fang, J. & Maeda, H. Exploiting the enhanced permeability and retention effect for tumor targeting. *Drug Discov. Today* **11,** 812–818 (2006).

7. Cao, F. *et al.* Lung-targeted delivery system of curcumin loaded gelatin microspheres. *Drug Deliv.* 1–10 (2011). doi:10.3109/10717544.2011.595842

8. Devarajan, P. V *et al.* Particle shape: a new design parameter for passive targeting in splenotropic drug delivery. *J Pharm Sci* **99,** 2576–2581 (2010).

9. Byrne, J. D., Betancourt, T. & Brannon-Peppas, L. Active targeting schemes for nanoparticle systems in cancer therapeutics. *Adv. Drug Deliv. Rev.* **60,** 1615–1626 (2008).

10. Béduneau, A., Saulnier, P. & Benoit, J. P. Active targeting of brain tumors using nanocarriers. *Biomaterials* **28,** 4947–4967 (2007).

11. Marcucci, F. & Lefoulon, F. Active targeting with particulate drug carriers in tumor therapy: Fundamentals and recent progress. *Drug Discov. Today* **9,** 219–228 (2004).

12. Choi, C. H. J., Alabi, C. A., Webster, P. & Davis, M. E. Mechanism of active targeting in solid tumors with transferrin-containing gold nanoparticles. *Proc. Natl. Acad. Sci. U. S. A.* **107,** 1235–1240 (2010).

13. Steichen, S. D., Caldorera-Moore, M. & Peppas, N. A. A review of current nanoparticle and targeting moieties for the delivery of cancer therapeutics. *Eur. J. Pharm. Sci.* **48,** 416–427 (2013).

14. Abou-Jawde, R., Choueiri, T., Alemany, C. & Mekhail, T. An overview of targeted treatments in cancer. *Clin. Ther.* **25,** 2121–2137 (2003).

15. Brannon-Peppas, L. & Blanchette, J. O. Nanoparticle and targeted systems for cancer therapy. *Adv. Drug Deliv. Rev.* **64,** 206–212 (2012).

16. Spragg, D. D. *et al.* Immunotargeting of liposomes to activated vascular endothelial cells: a strategy for site-selective delivery in the cardiovascular system. *Proc. Natl. Acad. Sci. U. S. A.* **94,** 8795–8800 (1997).

17. Psarros, C., Lee, R., Margaritis, M. & Antoniades, C. Nanomedicine for the prevention, treatment and imaging of atherosclerosis. *Maturitas* **73,** 52–60 (2012).

18. Sobczynski, D. J. *et al.* Plasma protein corona modulates the vascular wall interaction of drug carriers in a material and donor specific manner. *PLoS One* **9,** e107408 (2014).

19. Migliorini, C. *et al.* Red blood cells augment leukocyte rolling in a virtual blood vessel. *Biophys. J.* **83,** 1834–1841 (2002).

20. Munn, L. L. & Dupin, M. M. Blood cell interactions and segregation in flow. *Ann. Biomed. Eng.* **36,** 534–544 (2008).

21. Kumar, A. & Graham, M. D. Segregation by membrane rigidity in flowing binary suspensions of elastic capsules. *Phys. Rev. E - Stat. Nonlinear, Soft Matter Phys.* **84,** (2011).

22. Kumar, A. & Graham, M. D. Mechanism of margination in confined flows of blood and other multicomponent suspensions. *Phys. Rev. Lett.* **109,** (2012).

23. Zhao, H., Shaqfeh, E. S. G. & Narsimhan, V. Shear-induced particle migration and margination in a cellular suspension. *Phys. Fluids* **24,** (2012).

24. Tateishi, N. Flow dynamics of erythrocytes in microvessels of isolated rabbit mesentery: Cell-free layer and flow resistance. *J. Biomech.* **27,** 1119–1125 (1994).

25. Freund, J. B. Leukocyte margination in a model microvessel. *Phys. Fluids* **19,** (2007).

26. Kumar, A. & Graham, M. D. Margination and segregation in confined flows of blood and other multicomponent suspensions. *Soft Matter* **8,** 10536 (2012).

27. Charoenphol, P., Huang, R. B. & Eniola-Adefeso, O. Potential role of size and hemodynamics in the efficacy of vascular-targeted spherical drug carriers. *Biomaterials* **31,** 1392–1402 (2010).

28. Charoenphol, P. *et al.* Targeting therapeutics to the vascular wall in atherosclerosis-Carrier size matters. *Atherosclerosis* **217,** 364–370 (2011).

29. Eckstein, E. C., Tilles, A. W. & Millero 3rd, F. J. Conditions for the occurrence of large near-wall excesses of small particles during blood flow. *Microvasc Res* **36,** 31–39 (1988).

30. Tilles, A. W. & Eckstein, E. C. The near-wall excess of platelet-sized particles in blood flow: its dependence on hematocrit and wall shear rate. *Microvasc. Res.* **33,** 211–223 (1987).

31. Champion, J. A., Katare, Y. K. & Mitragotri, S. Particle shape: a new design parameter for micro- and nanoscale drug delivery carriers. *J. Control. Release* **121,** 3–9 (2007).

32. Toy, R., Hayden, E., Shoup, C., Baskaran, H. & Karathanasis, E. The effects of particle size, density and shape on margination of nanoparticles in microcirculation. *Nanotechnology* **22,** 115101 (2011).

33. Moghimi, S. M., Hunter, a C. & Andresen, T. L. Factors controlling nanoparticle pharmacokinetics: an integrated analysis and perspective. *Annu. Rev. Pharmacol. Toxicol.* **52,** 481–503 (2012).

34. Champion, J. A., Katare, Y. K. & Mitragotri, S. Making polymeric micro- and nanoparticles of complex shapes. *Proc Natl Acad Sci U S A* **104,** 11901–11904 (2007).

35. Perry, J. L., Herlihy, K. P., Napier, M. E. & Desimone, J. M. PRINT: A novel platform toward shape and size specific nanoparticle theranostics. *Acc. Chem. Res.* **44,** 990–998 (2011).

36. Gavze, E. & Shapiro, M. Motion of inertial spheroidal particles in a shear flow near a solid wall with special application to aerosol transport in microgravity. *J. Fluid Mech.* **371,** 59–79 (1998).

37. Lee, S. Y., Ferrari, M. & Decuzzi, P. Shaping nano-/micro-particles for enhanced vascular interaction in laminar flows. *Nanotechnology* **20,** (2009).

38. Decuzzi, P. & Ferrari, M. The adhesive strength of non-spherical particles mediated by specific interactions. *Biomaterials* **27,** 5307–5314 (2006).

39. Doshi, N. *et al.* Flow and adhesion of drug carriers in blood vessels depend on their shape: A study using model synthetic microvascular networks. *J. Control. Release* **146,** 196–200 (2010).

40. Champion, J. A. & Mitragotri, S. Role of target geometry in phagocytosis. *Proc Natl Acad Sci U S A* **103,** 4930–4934 (2006).

41. Champion, J. A. & Mitragotri, S. Shape induced inhibition of phagocytosis of polymer particles. *Pharm Res* **26,** 244–249 (2009).

42. Unger, E., Porter, T., Lindner, J. & Grayburn, P. Cardiovascular drug delivery with ultrasound and microbubbles. *Adv. Drug Deliv. Rev.* **72,** 110–126 (2014).

43. Ting, C. Y. *et al.* Concurrent blood-brain barrier opening and local drug delivery using drug-carrying microbubbles and focused ultrasound for brain glioma treatment. *Biomaterials* **33,** 704–712 (2012).

44. Nance, E. *et al.* Brain-Penetrating Nanoparticles Improve Paclitaxel Efficacy in Malignant Glioma Following Local Administration. *ACS Nano* (2014). doi:10.1021/nn504210g

45. Shuvaev, V. V. *et al.* Endothelial targeting of antibody-decorated polymeric filomicelles. *ACS Nano* **5,** 6991–6999 (2011).

46. Kamaly, N., Xiao, Z., Valencia, P. M., Radovic-Moreno, A. F. & Farokhzad, O. C. Targeted polymeric therapeutic nanoparticles: design, development and clinical translation. *Chem. Soc. Rev.* **41,** 2971 (2012).

47. Muro, S. *et al.* Endothelial targeting of high-affinity multivalent polymer nanocarriers directed to intercellular adhesion molecule 1. *J. Pharmacol. Exp. Ther.* **317,** 1161–1169 (2006).

48. Allen, T. M. Long-circulating (sterically stabilized) liposomes for targeted drug delivery. *Trends Pharmacol. Sci.* **15,** 215–220 (1994).

49. Allen, T. M. & Cullis, P. R. Liposomal drug delivery systems: From concept to clinical applications. *Adv. Drug Deliv. Rev.* **65,** 36–48 (2013).

50. Liong, M. *et al.* Multifunctional inorganic nanoparticles for imaging, targeting, and drug delivery. *ACS Nano* **2,** 889–896 (2008).

51. Huang, H.-C., Barua, S., Sharma, G., Dey, S. K. & Rege, K. Inorganic nanoparticles for cancer imaging and therapy. *J. Control. Release* **155,** 344–57 (2011).

52. Samokhin, G., Smirnov, M., Muzykantov, V., Domogatsky, S. & Smirnov, V. Effect of flow rate and blood cellular elements on the efficiency of red blood cell targeting to collagen-coated surfaces. *J. Appl. Biochem.* **6,** 70–75 (1984).

53. Muzykantov, V. R. Drug delivery by red blood cells: vascular carriers designed by Mother Nature. *Expert Opin. Drug Deliv.* **7,** 403–427 (2011).

54. Park, J. Il *et al.* Microbubbles loaded with nanoparticles: A route to multiple imaging modalities. *ACS Nano* **4,** 6579–6586 (2010).

55. Anselmo, A. C. & Mitragotri, S. Cell-mediated delivery of nanoparticles: Taking advantage of circulatory cells to target nanoparticles. *J. Control. Release* (2014). doi:10.1016/j.jconrel.2014.03.050

56. Geers, B. *et al.* Self-assembled liposome-loaded microbubbles: The missing link for safe and efficient ultrasound triggered drug-delivery. *J. Control. Release* **152,** 249–256 (2011).

57. Lee, S. Y., Ferrari, M. & Decuzzi, P. Shaping nano-/micro-particles for enhanced vascular interaction in laminar flows. *Nanotechnology* **20,** 495101 (2009).

58. Jurney, P. *et al.* The Effect of Nanoparticle Size on Margination and Adhesion Propensity in Artificial Micro-Capillaries. *Proc. Asme Micro/Nanoscale Heat Mass Transf. Int. Conf. 2012* 109–115 (2012). at <<Go to ISI>://WOS:000324346800015>

59. Namdee, K. *et al.* In vivo evaluation of vascular-targeted spheroidal microparticles for imaging and drug delivery application in atherosclerosis. *Atherosclerosis* **237,** 279–286 (2014).

CHAPTER 2: MATERIALS AND METHODS

2.1 Introduction and Common Materials

This section contains the materials and methods used to complete the experimental research described in the following four chapters of this dissertation. Sources of the materials and clear procedures are given to allow for reproduction of all results described. Model vascular-targeted carriers are prepared and the propensity to adhere to inflamed endothelium in a variety of hemodynamic conditions are investigated, both *in vitro* using a parallel plate flow chamber (PPFC) assay and *in vivo* using murine models of atherosclerosis or systemic inflammation. The materials (and source) will be listed within the specific subsection for which that material was utilized.

2.1.1 Particles used for Vascular-Targeting

Fluoresbrite® YG Carboxylate polystyrene spheres (500 nm, 1 μm, and 2 μm diameter) were purchased from Polysciences, Inc. (Warrington, PA). Fluorescent (green) carboxylated silica spheres (500 nm diameter) were purchased from Corpuscular, Inc (Cold Springs, NY). Amine-terminated titania spheres were purchased from EPRUI Nanoparticles & Microparticles Co Ltd (Nanjing, China).

2.1.2 Phosphate Buffers

Dulbecco's phosphate buffered saline (with Ca^{2+} and Mg^{2+} ions), Dulbecco's phosphate buffered saline (without Ca^{2+} and Mg^{2+} ions), sodium dihydrogen phosphate, sodium phosphate

dibasic, dextran and bovine serum albumin (BSA) were purchased from Sigma Aldrich (Saint Louis, MO).

Multiple types of phosphate buffers are used and will be referred to as follows. 50 mM PBS is made as 50 mM sodium dihydrogen phosphate, 50 mM sodium phosphate dibasic, and 0.9% NaOH, and adjusted to pH 7.4. PBS – 1% BSA refers to 50 mM PBS with 1% w/v BSA added. PBS++1%BSA refers to 1X Dulbecco's phosphate buffered saline with 1% w/v BSA added. Viscous buffer (VB) refers to PBS++1%BSA with 1.4% w/v dextran added to match the viscosity of human plasma. PBS-\- refers to 1X Dulbecco's phosphate buffered saline (without Ca^{2+} and Mg^{2+} ions).

2.2 Fabrication of Ellipsoidal Particles: Heat Stretching

Fluoresbrite® YG Carboxylate polystyrene spheres (500 nm, 1 µm, and 2 µm diameter) were purchased from Polysciences, Inc. (Warrington, PA). Poly(vinyl alcohol) (PVA) and isopropanol were purchased from Sigma Aldrich (Saint Louis, MO). Nunc™ OmniTrays™ were purchased from Thermo Scientific (Waltham, MA). A previously developed polymer film stretching method was used to form prolate (rod-like) and oblate (disk-like) ellipsoidal particles.[1–3] Polystyrene spheres were suspended in a solution of 10% w/v aqueous PVA and cast into a film by pouring into Nunc™ OmniTrays™. Films were dried on a leveling table overnight before being removed from trays for heat stretching. Ellipsoidal particles were formed by stretching films uniaxially using one pair of parallel movable clamps or biaxially using two pairs of movable parallel clamps. Clamp mechanisms were housed in customized ovens to allow for manipulation of films at high temperature. Films were heated to approximately 150 °C and stretched uniaxially to produce prolate ellipsoids (rods) or biaxially to produce oblate ellipsoids (disks). Stretched films were cooled back to room temperature before removing from clamps

and dissolving in 30% isopropanol overnight and subsequently washed/centrifuged multiple times to ensure minimal residual PVA. Samples of recovered particle stocks were dried and imaged using a Philips XL30 FEG SEM (courtesy of University of Michigan EMAL). Particle dimensions were obtained from SEM images via Metamorph® Software (Molecular Devices, LLC). Rods and disks having equivalent spherical diameters (ESD) of 500 nm, 1 μm, and 2 μm and aspect ratios ranging from 2-11, as well as equivalent volume spherical particles were used in experiments. Particle dimensions of ellipsoidal particles will be given in the experimental section in which the particles were used.

2.3 Vascular Targeting: Conjugation with Targeting Ligands

Particle surfaces are conjugated with targeting ligands for both PPFC assays and *in vivo* experiments. In general, functionalized particles (either surface carboxylated or surface aminated) are covalently coupled with avidin protein. Then, particles are conjugated with biotinylated ligands on the day of the experiment. After avidin conjugation, the ligand conjugation procedure is slightly different between *in vitro* and *in vivo* experiments, and as such, will be described separately.

2.3.1 Avidin Conjugation

Neutravidin® Biotin Binding Protein (Avidin), NHS-Biotin, and 1-ethyl-3-(-3-dimethylaminopropyl) carbodiimide hydrochloride (EDAC) were purchased from Thermo Scientific (Waltham, MA). MES hydrate, dimethyl sulfoxide (DMSO), and glycine were purchased from Sigma Aldrich (Saint Louis, MO).

Carboxylated particles were suspended in 5 mg/mL avidin in 50 mM aqueous MES and rotated for 15 min at room temperature. Then, an equal volume of EDAC solution (75 mg/mL in

50 mM aqueous MES) was added to the avidin-particle solution and the solution was adjusted to pH of 8. Particles were rotated for ~20 hours before adding glycine to a final concentration of 100 mM. After a 30 min incubation, particles were washed twice and stored with 50 mM PBS at 4°C until further conjugation. Aminated particles were suspended in 10 mM NHS-Biotin in DMSO and rotated (covered) for 1 hour. Particles were washed twice with 50 mM PBS, then reconstituted in 1 mL of 5 mg/mL avidin in 50 mM PBS and rotated for ~20 hours. Particles were then washed once and reconstituted with 50 mM PBS. Particles were stored at 4°C until further conjugation.

2.3.2 Ligand Conjugation for *In Vitro* Flow Assays

Biotinylated sialyl Lewis A (sLe^a) was purchased from Glycotech (Gaithersburg, MD). Biotin-FITC conjugate was purchased from Thermo Scientific (Waltham, MA). Biotinylated sialyl Lewis A solution was prepared by dissolving in PBS-1%BSA at a concentration ranging between 0.1-10 µg/mL. The sLe^a concentration used is pre-determined using flow cytometry (described below) to provide the desired sLe^a site density on the particle surface (#/µm^2). The number of particles used per conjugation was 1.8 x 10^7 particles (for 1 and 2 µm ESD particles) or 5 x 10^7 particles (500 nm ESD). Particles were added to 100 µL of sLe^a solution and rotated for 20 mins. For experiments exploring particle shape (Chapter 3), particles were washed twice and stored in 1 mL PBS++-1%BSA at 4°C until used in the experiment. For experiments exploring particle density (Chapter 5), particles were rotated an additional hour with 100 µL Biotin-FITC at 5 µg/mL (to aid in post-experiment imaging) before being washed twice and stored in PBS++-1%BSA at 4°C.

2.3.3 Ligand Conjugation for *In Vivo* Experiments

Biotinylated rat anti-mouse CD106 (aVCAM-1) was purchased from BD Pharmingen (San Jose, CA). A solution of aVCAM-1 was made by dissolving in PBS-1%BSA (5 µg/mL, unless otherwise stated). Avidin-coated particles were added to a solution of sLe^a and aVCAM (equal parts sLe^a solution and aVCAM solution, 200 µL total) and rotated for 45 min. For experiments exploring particle shape (Chapter 3), particles were washed twice and stored in 1 mL PBS++-1%BSA at 4°C until used in the experiment. For experiments exploring particle density (Chapter 5), particles were rotated an additional hour with 100 µL Biotin-FITC at 5 µg/mL to aid in post-experiment imaging before being washed twice and stored in PBS++-1%BSA at 4°C.

2.3.4 Quantification of Ligand Site Density

Biotin-phycoerythrin conjugate was purchased from Life Technologies (Waltham, MA). Biotin-FITC conjugate was purchased from Thermo Scientific (Waltham, MA). Anti-CLA-PE, human was purchased from Miltenyi Biotec (San Diego, CA). Particles coated with sLe^a were incubated with 10 µg/mL anti-CLA-PE in 100 µL total volume for 20 mins. Isotype controls were performed to ensure specificity of staining antibodies. Particles were washed twice and reconstituted in filtered water or PBS-1%BSA before fluorescent intensity (PE) was measured with either a BD FACSCalibur® or Attune® Acoustic Focusing Cytometer. Site densities were back calculated by comparing fluorescent intensity with standard calibration beads purchased from Bangs Labs (Fishers, IN). Approximate site densities for particle types used in specific experiments are listed in the relevant sections of the text.

2.4 Blood Collection and Treatment

Blood from human donors was drawn into syringes containing the anticoagulant acetate citrate dextrose according to IRB approved protocols and in line with the WMA Declaration of Helsinki. Red blood cells (RBC) were separated by dextran sedimentation for 2 hours and were washed once with PBS-/- before storing at 37 °C until use. All flow assays utilized reconstituted blood (RBCs reconstituted in PBS++1%BSA or VB, as specified) at either 30% or 40% hematocrit.

2.5 HUVEC Isolation and Culture

Primary human umbilical vein endothelial cells (HUVEC) were obtained from human umbilical cords (University of Michigan C.S. Mott Children's Hospital) according to a previously described protocol.[4] Briefly, the umbilical veins were filled with a collagenase solution for 30 mins, degrading the extracellular matrix to release the HUVEC. Isolated cells were pooled from multiple donors and were grown in culture flasks until confluent. Subsequent passages of HUVEC were either grown in culture flasks or on glass coverslips which were coated with porcine gelatin and crosslinked with glutaraldehyde for use in PPFC assays per a previously described protocol.[5]

2.6 Parallel Plate Flow Chamber

2.6.1 Experimental Setup

A PPFC was purchased from Glycotech (Gaithersburg, MD). The height and width of the flow channel is set by a silicone gasket. The height and width of the chamber used is 254 μm and 1 cm, respectively, unless otherwise specified. The bottom of the flow chamber is formed by a glass coverslip covered with a confluent monolayer of HUVECs. Laminar flow through the

chamber is generated by a programmable syringe pump downstream of the channel, and the shear rate at the channel wall is determined using **Equation 2.1**, where *Q* is the volumetric flow rate, *h* is the channel height, and *w* is the channel width. A range of physiological shear rates are investigated, and are specified in the appropriate experimental sections.

Equation 2.1 Relationship between flow rate, wall shear, and PPFC dimensions

$$\gamma_w = \frac{6Q}{h^2 w}$$

Two physiologically relevant pulsatile flow profiles were also investigated via a programmable syringe pump; forward flow at alternating low and high shear rates (120-1200 s^{-1}), and oscillating forward/reverse flow at high shear (1000 s^{-1}) with a net forward flow as previously described.[5,6]

Also, a step channel was used to simulate regions of recirculation flow, typical of regions where atherosclerotic plaques are known to accumulate.[6] The step channel has a pre-step channel height of 125 μm and a post-step channel height of 500 μm. A region of recirculating flow is created immediately downstream of the step when laminar flow through the channel passes over the step. The recirculating flow region extends to a stagnation, or reattachment, point where there is no fluid velocity in the direction parallel to the bottom of the chamber at the wall. Downstream of the reattachment point, flow develops into a 1-dimensional flow profile with fluid velocity in the direction parallel to the bottom of the chamber.

In the *in vitro* adhesion assays performed, the flow rate (thus the wall shear rate), flow type (laminar, pulsatile, recirculation), hematocrit, and channel orientation all can be varied, and are specified in the appropriate experimental sections.

2.6.2 Adhesion Assays

IL-1β cytokine was purchased from Fitzgerald (Acton, MA). Confluent HUVEC grown on glass coverslips were activated (inflamed) via addition of fresh culture media containing 1 ng/mL of IL-1β to cells in static for 4 hours. This treatment induces the upregulation of E-selectin, to which the targeting ligand on the particle (sLe^a) binds. After activation, the coverslip is attached to the bottom of the PPFC flow deck. Targeted particles in reconstituted blood at a fixed concentration (5×10^5 #/mL, unless otherwise specified) were then perfused through the flow channel at the specified flow conditions for a fixed period of time. The chamber was flushed with PBS++1%BSA at the end of experimental time and the HUVEC monolayer was observed using a Nikon TE 2000-S Inverted Microscope. Adhesion data was captured using a Photometric CoolSNAP EZ digital camera with a Sony CCD sensor, and adherent particles were quantified using Metamorph® software.

2.6.3 Localization Assays

For localization assays examining the effect of particle size and shape (Chapter 3), the same PPFC setup (without HUVEC monolayer) was used to image particles localized to a near-wall focal plane. A Leica Inverted SP5X Confocal Microscope (MIL, University of Michigan) was used to visualize the localization of fluorescent particles to the CFL from reconstituted blood being perfused through a PPFC. Particle visualization was performed at a focal plane of 2 μm height from the bottom of the chamber, unless otherwise specified. Particles were added to reconstituted blood at various concentrations and WSR as specified in the appropriate experimental sections. The localization to the near-wall focal plane for each particle shape/size was imaged using Leica Microsystems LAS AF Lite Imaging Software. The localization of differently shaped particles was compared by counting the fluorescent particles seen in each

image at the same particle concentration used for adhesion assays. The localization of micro and nanospheres was quantified by mean fluorescence of each image at either 1X (5×10^5 #/mL) or 5X concentration.

For localization assays examining the effect of particle density (Chapter 5), rectangular microchannels with the same approximate height used in PPFC assays were utilized. Sticky-Slide I 0.2 Luer, sterile rectangular microchannels were purchased from Ibidi LLC (Verone, WI). Fluorescent particles were mixed with reconstituted blood and flowed through the microchannel at a WSR of 500 s^{-1}. The microchannel was live-imaged using an Olympus FB 1200 Confocal Microscope (compliments of Dr. Greg Thurber, University of Michigan) under 20x magnification. Images were captured of a focal plane within 2 μm into the flow from the top surface of the microchannel. After thresholding the background noise, the "Analyze particles" function in ImageJ was used to automatically count the instantaneous number of particles localized to the near-wall focal plane.

2.7 *In Vivo* Experiments

All procedures used for animal experimentation were approved by the University of Michigan Committee on Use and Care of Animals (UCUCA) and are in compliance with the guidelines for the "Care and Use of Laboratory Animals" set by the University, State, and Federal regulations. A murine model of atherosclerosis (ApoE -/-) was employed to examine the plaque targeting of spherical and rod-shaped targeted particles (Chapter 4). A wild-type mouse model of systemic inflammation was employed to examine the inflammation targeting ability of particles with different density (Chapter 6). The materials and methods are described separately as follows.

2.7.1 Apo E -/- Murine Model

Twenty-five homozygous ApoE-/- mice and twenty-five wild-type mice at 8-10 weeks of age were purchased from Jackson Laboratories (Bar Harbor, ME). Mice were fed a normal diet for 20 weeks. Mice with an average weight of 28 g were randomly assigned into five groups of five animals, and dual-targeted particles were administered via a 200 µL bolus injection into the tail vein at a dosage of 20 x 10^6 particles in phosphate buffered saline per mouse. The post injection protocol is described further in section 2.7.3.

2.7.2 Systemic Inflammation Model

Mouse TNF-α cytokine was purchased from BD Pharmingen (San Jose, CA). Twenty-four wild-type male mice at 20 weeks of age were purchased from Jackson Laboratories (Bar Harbor, ME). Mice were assigned to three groups of five animals (dual-targeted) and three groups of three animals (IgG controls), and each mice was injected via tail-vein with Mouse TNF-α cytokine at a concentration of 10 ng/mL in 300 µL PBS to induce inflammation of the murine vasculature. Twenty-four hours after injection of TNF- α, particles were injected via tail-vein at a dosage of $40x10^6$ particles per mouse in 200 µL of PBS. The post injection protocol is described further in section 2.7.3.

2.7.3 *In Vivo* Experimental Protocol

30 min after injection, mice were anaesthetized with 100 µL of a mixture of 35% ketamine and 5% xylazine in PBS, and additional anesthesia was administered as necessary. Blood was drawn via cardiac puncture from the left ventricle using a heparin-coated syringe. Then, the right atrium was nicked and the vasculature was perfused with ice-cold PBS by injection into the puncture site at the apex of the left ventricle. The lung, liver, spleen, and kidney were harvested and snap-frozen in liquid nitrogen. Consequently, the heart and aorta

were perfused again with ice-cold 4% paraformaldehyde (PFA) in PBS at pH 7.5. Whole mice were preserved in 4% PFA until aorta isolation. The aorta were excised from the aortic arch to the iliac branches, including the renal branches and celiac branch, and kept in 4% PFA in PBS.

Aortae were excised into segments along the full length including the aortic arch, abdominal branches, and iliac branches. Aortic segments were bisected and mounted open *en face* on glass slides with 4% PFA, and coverslips were sealed using nail polish agent. Aorta were imaged using a Nikon TE 2000-S Inverted Microscope and an attached Photometric CoolSNAP EZ digital camera with a Sony CCD sensor (Chapter 4) or an Olympus FB 1200 Confocal Microscope (Chapter 6) under 20x, 40x, or 60x magnification. *En face* images were quantified by counting the number of adherent particles to the aorta. For each group of mice, the number of adherent particles along the entire aorta was averaged. Particle adhesion was also normalized to the area of each section, to give an adhesion density per section of aorta.

Particle biodistribution in major organs was also quantified. Multiple samples from each organ were weighed and homogenized in 1 mL of PBS++. The concentration of particles in each homogenized solution was quantified using a hemocytometer. For the lungs and liver, a portion of the organ was harvested and analyzed for particle accumulation. For lungs, a portion of the left lobe was used, and for the liver, a portion of the left lateral lobe was used. Whole organs were used to quantify particle accumulation in the kidney and spleen. Particle accumulation is reported as % injected dose/gram organ (%ID/g).

2.8 Data Analysis

Data for *in vitro* adhesion experiments is quantified as the number of adherent particles per mm^2 of endothelium. Ten fields of view (20x magnification) were imaged, and the average

number of adherent particles per field of view is divided by the field of view area. Adhesion density following recirculation flow experiments is quantified at 100 μm intervals downstream from the step, so the adhesion is divided by the appropriate area of a 100 μm wide lateral region at 20x magnification. Standard error bars are plotted and significant differences are analyzed via a one-way ANOVA with Tukey's post-test or student t test, with a p value < 0.05 considered statistically significant, unless otherwise stated.

Data for localization experiments was quantified in one of two ways. For localization experiments comparing 500 nm and 2 μm ESD spheres (Chapter 3), the mean fluorescence per image is calculated and normalized to the mean fluorescence at 1x concentration. For localization experiments comparing spheres and ellipsoids (Chapter 3) or particles of different density (Chapter 6), an instantaneous particle localization is quantified as the average number of particles visible in the field of view divided by the field of view area. Standard error bars are plotted and significant differences are analyzed via a one-way ANOVA with Tukey's post-test or student t test, with a p value < 0.05 considered statistically significant, unless otherwise stated.

Aorta adhesion data for *in vivo* experiments is reported as average number of particles adherent to the whole aorta, as well as the average particle adhesion to each aortic section. Also, adhesion is normalized to the area of each aortic section to give the particle adhesion density. For experiments comparing particles of different shape (Chapter 4), adhesion is normalized to the adhesion of 500 nm spheres. Standard error bars are plotted and significant differences are analyzed via a one-way ANOVA with Tukey's post-test or student t test, with a p value < 0.05 considered statistically significant, unless otherwise stated.

Biodistribution data for *in vivo* experiments is reported as % injected dose/gram organ (%ID/g). Standard error bars are plotted and significant differences are analyzed via a one-way ANOVA with Tukey's post-test or student t test, with a p value < 0.05 considered statistically significant, unless otherwise stated.

References

1. Ho, C. C., Keller, A., Odell, J. A. & Ottewill, R. H. Preparation of monodisperse ellipsoidal polystyrene particles. *Colloid Polym. Sci.* **271,** 469–479 (1993).

2. Ho, C. C., Ottewill, R. H., Keller, A. & Odell, J. A. Monodisperse ellipsoidal polystyrene latex particles: Preparation and characterisation. *Polym. Int.* **30,** 207–211 (1993).

3. Champion, J. A., Katare, Y. K. & Mitragotri, S. Making polymeric micro- and nanoparticles of complex shapes. *Proc Natl Acad Sci U S A* **104,** 11901–11904 (2007).

4. Huang, R. B. & Eniola-Adefeso, O. Shear stress modulation of IL-1beta-induced E-selectin expression in human endothelial cells. *PLoS One* **7,** e31874 (2012).

5. Charoenphol, P., Huang, R. B. & Eniola-Adefeso, O. Potential role of size and hemodynamics in the efficacy of vascular-targeted spherical drug carriers. *Biomaterials* **31,** 1392–1402 (2010).

6. Charoenphol, P. *et al.* Targeting therapeutics to the vascular wall in atherosclerosis-Carrier size matters. *Atherosclerosis* **217,** 364–370 (2011).

CHAPTER 3: THE MARGINATION PROPENSITY OF ELLIPSOIDAL MICRO/NANOPARTICLES TO THE ENDOTHELIUM IN HUMAN BLOOD FLOW

The majority of the work in this chapter is published as AJ Thompson, EM Mastria, and O Eniola-Adefeso. The margination propensity of ellipsoidal micro/nanoparticles to the endothelium in human blood flow. *Biomaterials* 34 (23), 5863-5871 (2013).

ABSTRACT

Particle shape is becoming increasingly recognized as an important parameter for the development of vascular-targeted carriers (VTC) for disease treatment and diagnosis. However, limited research exists that investigates how particle shape coupled with hemodynamics affects VTC margination (localization and adhesion). In this study, we investigate the effects of particle shape parameters (volume, aspect ratio, axis length) on the margination efficacy of targeted spheres, prolate ellipsoids, and oblate ellipsoids in an inflamed endothelial wall from human blood flow in an in vitro model of human vasculature. Overall, particles with 2 μm equivalent spherical diameters (ESD) display higher margination than particles with either 1 μm or 500 nm ESDs. Interestingly, rod-shaped microparticles (1 μm or 2 μm ESD) with high aspect ratios display significantly improved margination compared to spheres of equal volume, particularly under high shear rates and disturbed flow profiles. Nanorods (500 nm ESD), even with high aspect ratio, do not display enhanced margination compared to that of equivalent spheres, which suggests that nanorods, like nanospheres, display minimal margination due to their inability to effectively localize to the vessel wall in the presence of red blood cells (RBC).

3.1 Introduction

Vascular-targeted carriers (VTC) offer unique opportunities to improve disease diagnosis and treatment by providing highly localized delivery of therapeutics/imaging agents. Regardless of the carrier type (e.g. polymeric, liposomes, dendrimers, micelles, etc) the typical geometry for a VTC is spherical with diameters on the nanometer scale. However, recent publications have shown that nanospheres may be suboptimal for targeting diseases affecting larger vessels with bulk blood flow, such as atherosclerosis.[1,2] In bulk blood flow, red blood cells (RBC) tend to move to the center of flow, resulting in a RBC core that forces leukocytes and platelets to concentrate into the red blood "cell free layer" (CFL) adjacent to the vascular wall. This enhanced concentration at the wall, i.e. "near-wall excess", then allows for these cells to optimally interact with the endothelium despite large vessel diameters. Microspheres (2-10 μm diameters) can also take advantage of the near-wall excess mechanism[1–4], allowing for their efficient margination (localization and adhesion) to the endothelium from bulk blood flow. Nanospheres, however, are not similarly displaced to the CFL, and thus exhibit minimal margination from bulk blood flow.[1–5]

Therefore, one major challenge in targeting atherosclerosis is in designing carriers that have the capacity to localize to and have a high affinity for binding to the vascular wall from bulk blood flow. Recent published works have suggested that deviating from the typical spherical shape of VTCs could potentially improve VTC performance. Specifically, macrophages are reported to be less efficient at engulfing elongated particles of sufficient volume than spheres, which could translate to reduced clearance and lower accumulation in non-targeted organs.[6,7] Indeed, non-spherical microparticles of similar volume have been shown to have different *in vivo* biodistribution profiles in tumor-bearing mice.[8] Drug-loaded filamentous

micelles have also been shown to persist in circulation for much longer than spherical micelles in mice[9], and ICAM-1 targeted elliptical disks were shown to have a longer circulation half-life and a better targeting specificity than their spherical counterparts.[10] Theoretical works have also predicted that ellipsoidal particles display a preferential lateral drift in shear flow near a wall (analogous to the CFL).[11,12] Also, disk-shaped particles are predicted to better adhere to endothelial cells in the presence of flow-induced shear stress, due to both a higher contact surface with the endothelium and a streamlined shape.[13] Recent experimental works have also demonstrated that particle elongation can increase particle adhesion to protein-coated surfaces in microchannels; however these works were done with particles in low shear buffer flows and thus do not provide indication as to whether these particles can better localize to the CFL from the RBC core than spheres.[14,15] Thus, it largely remains unclear how particle shape affects margination in human blood flow, and in conditions relevant to targeting the endothelium in blood vessels with bulk blood flows.

This study seeks to evaluate the efficiency of rod-shaped and disk-shaped, relative to spherical, model VTCs in marginating to the vascular wall in the presence of RBCs via parallel plate flow chamber (PPFC) adhesion assays, with the central goal of identifying particle shape parameters (volume, aspect ratio, major/minor axis length), if any, that are paramount in determining the capacity for VTCs to readily marginate in physiological human blood flow conditions. Pulsatile and recirculation blood flow patterns were used in adhesion assays for relevance in large arteries and areas of sudden expansion within these arteries, respectively, that are typically afflicted with atherosclerosis. Steady laminar blood flow was explored for their relevance in small arteries (i.e. arterioles) that are important in cancer and some cardiovascular diseases, including arteriolosclerosis and specific types of vasculitis.

3.2 Results

Prolate ellipsoids (rods) having ESD of 2 μm, 1 μm, and 500 nm were used with aspect ratios ranging from 2 to 11. The dimensions of the particles used in this study are given in Table 3.1, where rods are denoted by their aspect ratios (AR) – the ratio of the major axis length to the minor axis length.

Table 3.1 Dimensions for spherical and rod-shaped particles used in adhesion experiments (ESD=equivalent spherical diameter)

Particle Shape	ESD [μm]	Aspect Ratio	Major Axis [μm]
Sphere	**2.07**	1.00	2.07
AR-2		2.11	3.39
AR-4		4.03	5.21
AR-9		9.09	8.97
Sphere	**1.01**	1.00	1.01
AR-2		1.98	1.61
AR-4		4.17	2.76
AR-11		11.23	5.90
Sphere	**0.52**	1.00	0.52
AR-2		2.14	0.85
AR-4		4.50	1.40
AR-10		10.15	2.41

3.2.1 Particle adhesion in laminar blood flow

Figure 3.1 shows the adhesion of spheres and rods with an equivalent spherical diameter (ESD) of 2 μm to an activated HUVEC monolayer from laminar blood flow of reconstituted human blood at 30% hematocrit (Hct - % RBC by volume) in a PPFC. At a wall shear rate (WSR) of 200 s^{-1}, there was no difference in the adhesion of particles between the different shapes. At 500 s^{-1}, all spheres and rods with aspect ratio (AR – the ratio of the major axis length

to the minor axis length) ≤ 4 displayed the same level of adhesion, while the adhesion density of rods with AR of 9 was 31% higher than that of equivalent spheres. At the highest WSR of 1000 s^{-1}, the adhesion density of AR ≤ 4 was either the same or slightly higher than spheres; however, the adhesion density of AR-9 rods was 121% higher compared to spheres. Overall, as the WSR increased, the adhesion density for each particle type also increased – likely due to the increased number of particles fed through the chamber at higher shear rates for a fixed experiment time.

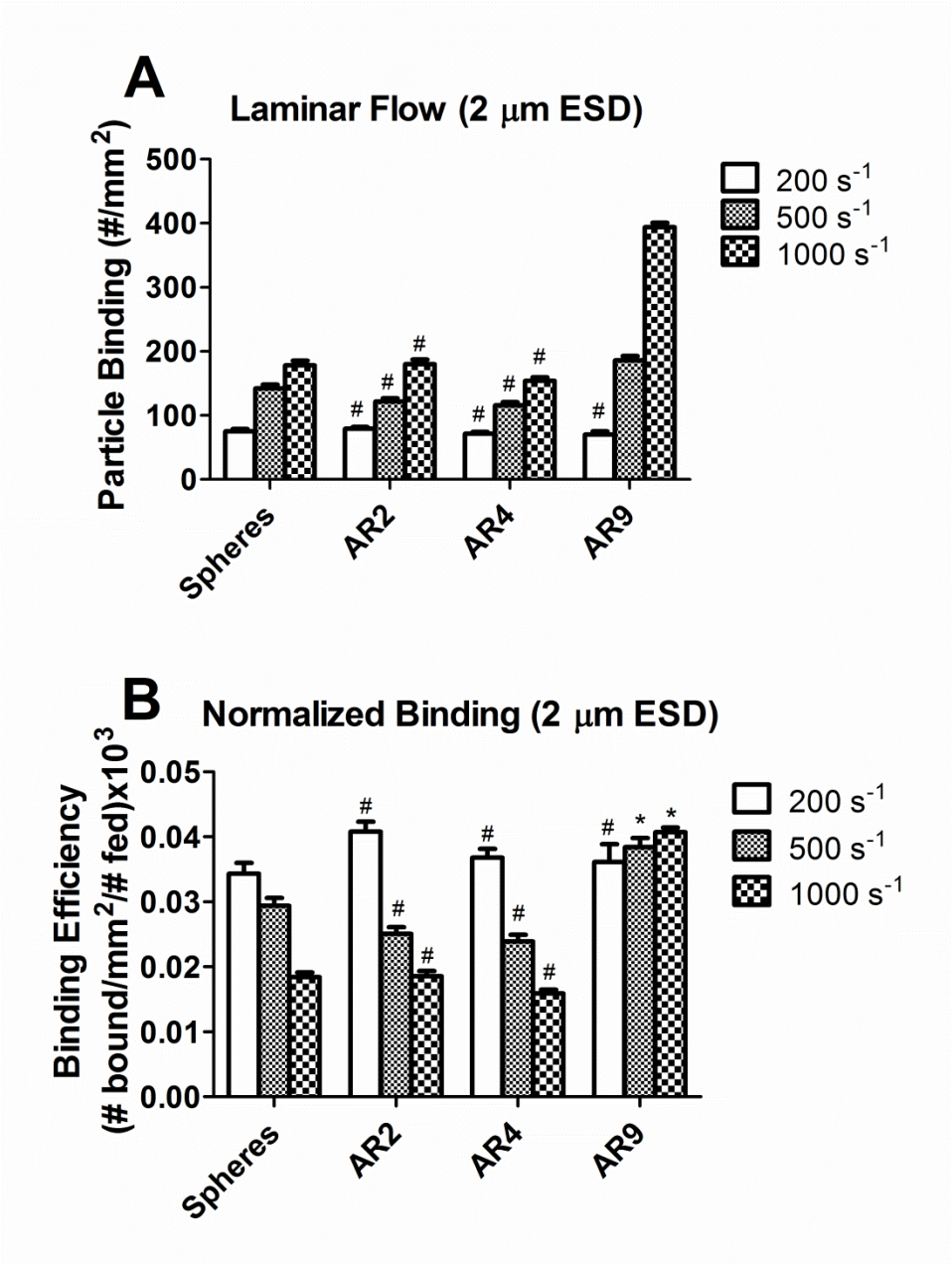

Figure 3.1 Adhesion density (A) and flux-normalized adhesion (B) of sLe^a-coated spheres and rods (2 μm ESD) to activated ECs from 30% RBCs in buffer after 3 min of steady flow through a PPFC. A fixed sLe^a density of 970 ± 40 sites·μm^{-2} is used for all particles. Flux-normalized adhesion is achieved by dividing the particle adhesion density by the absolute number of particles fed through the PPFC after 3 min of flow. Particle concentration = 5 x 10^5 #/mL blood. * = not significant ($p > 0.01$) compared to adhesion of the same particle at the immediately lower WSR and # = not significant ($p > 0.01$) compared to adhesion of spheres at the same WSR via one-way ANOVA with Tukey post-test, $n \geq 3$.

To better understand how efficiently particles adhere under different shear conditions, the adhesion data was normalized for the increased particle flux with increasing shear rates by dividing the adhesion density by the total number of particles that passed through the flow chamber. From the normalized data (Figure 3.1B), it is apparent that the binding efficiency of spheres and rods with AR $\leq$ 4 decreased with increasing WSR. However, the AR-9 rods displayed the same binding efficiency over all shear rates despite the higher shear forces present at higher WSRs. Similar results were obtained for AR-9 rods when adhesion efficiency was evaluated with assays having the total amount of particles fed into the flow chamber fixed between low and high WSR (Figure 3.2A), e.g. the concentration of particles fed at 1000 s^{-1} was 5 times lower than the concentration fed at 200 s^{-1} for a fixed experiment time of 3 min.

Particle binding assays were also performed with particles having a fixed total number of sLe^a copies to see if the maintained binding efficiency shown for AR-9 rods compared to spheres is simply a result of a higher number of ligand copies on rods for experiments done with a fixed ligand density as in Figure 3.1B (spheres and rods have a fixed sLe^a density of ~1000 sites/μm^2, thus rods have a higher number of total targeting ligand copies available for binding). As shown in Figure 3.2B, with all particles having about 14,000 ± 1000 (SE) sLe^a copies on their surface, the adhesion for the AR-9 rods (now at ~600 sLe^a sites/μm^2) was still higher than that of spheres (~1000 sLe^a sites/μm^2) at both 500 and 1000 s^{-1} WSR. Also, the adhesion of AR-9 rods increased as the WSR is increased from 500 to 1000 s^{-1} – however the level of adhesion does not quite double (as was the case for the fixed sLe^a density assays shown in Figure 3.1).

To determine if rods exhibit enhanced localization to the CFL from the RBC core, the localization of spheres, AR-4 rods, and AR-9 rods to the CFL was visualized using confocal microscopy at the same 1000 s^{-1} condition used in the laminar adhesion assay. Images were

taken to show the number of particles localized to a near-wall region 2 μm away from the step at any instant. No significant difference in the average number of particles localized to the CFL was observed between spheres and rods with 2 μm ESD (Figure 3.3).

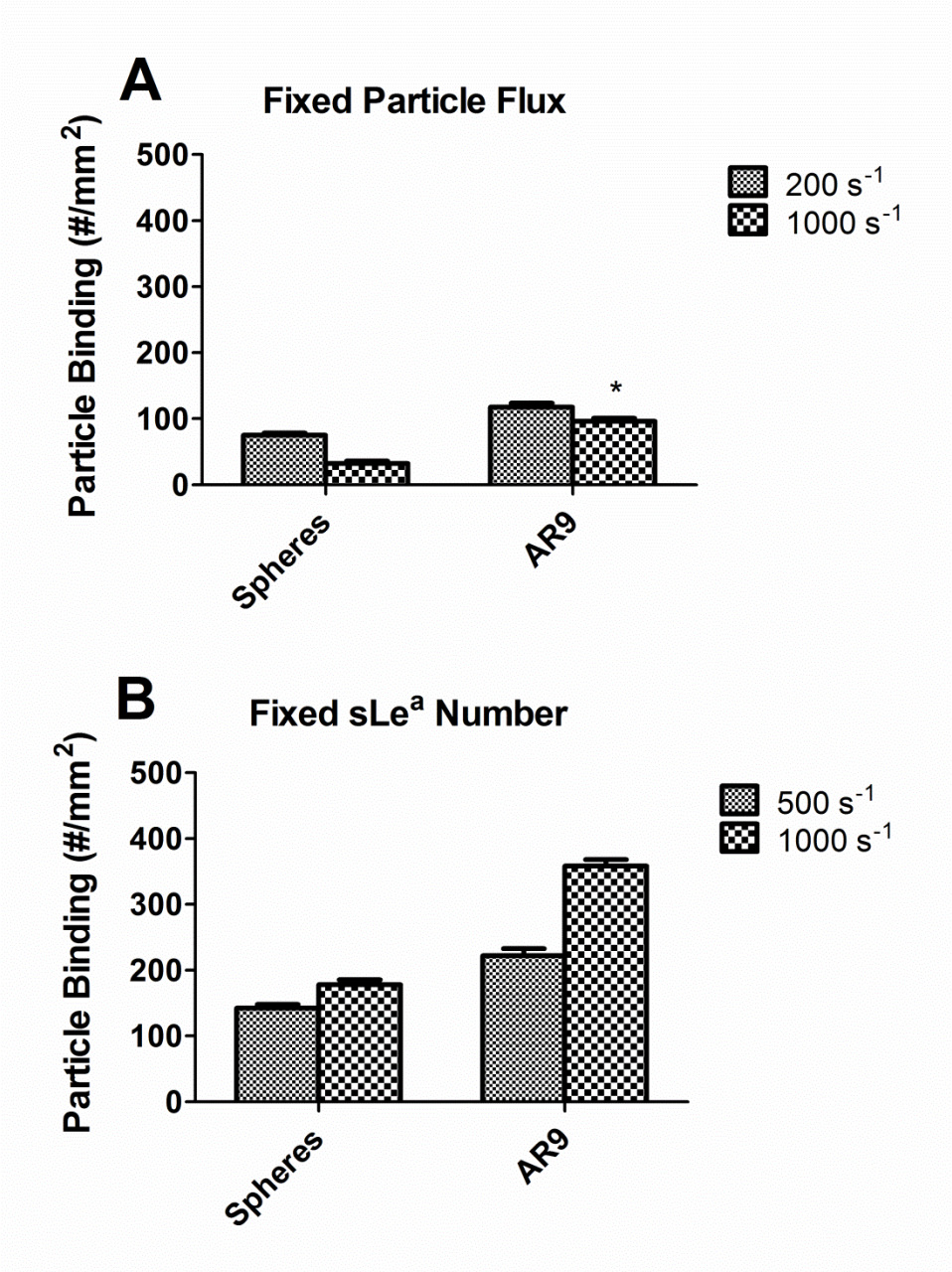

Figure 3.2 Adhesion density of spheres and AR-9 rods with ESD of 2 μm from 30% RBC in buffer to activated HUVEC following 3 min of steady flow through a PPFC with either (A) a fixed particle flux or (B) a fixed number of sLe^a sites on all particles at a fixed particle concentration. The fixed particle flux condition was achieved by feeding particles into the PPFC at a 5x lower concentration at 1000 s^{-1} than at 200 s^{-1}. Particles used in the fixed sLe^a number experiment were coated with a total of 14,000 ± 1000 sLe^a/particle. * = not significant ($p > 0.01$) compared to adhesion of the same particle at the immediately lower WSR and # = not significant ($p > 0.01$) compared to adhesion of spheres at the same WSR via one-way ANOVA with Tukey post-test, $n \geq 3$.

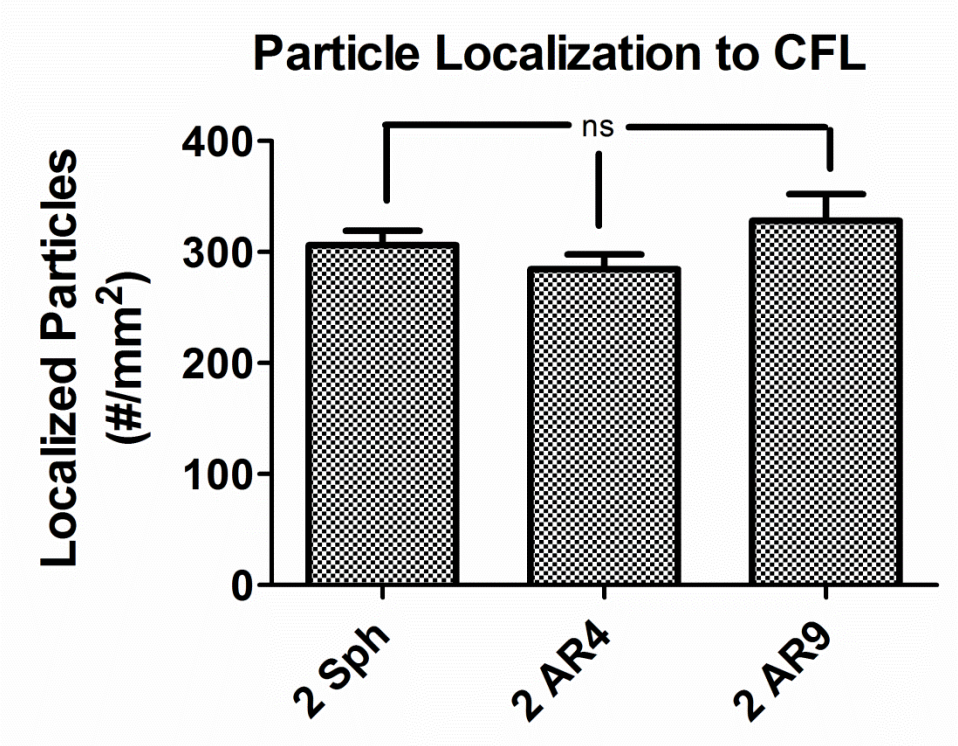

Figure 3.3 Number of particles localized to the CFL from 30% Hct RBC in buffer flow in a PPFC at a WSR of $1000s^{-1}$ normalized to the square area of each confocal image analyzed. ns = $p > 0.01$

Next, the adhesion density of spheres and rods with 1 μm ESD to activated HUVEC was evaluated in laminar RBC flows at 30% Hct (Figure 3.4). The adhesion density for AR-11 rods was significantly higher than that of equivalent spheres at all WSRs and was more pronounced with increasing WSRs. Also, the adhesion density for AR-4 rods was higher relative to spheres only at the 1000 s^{-1} WSR while AR-2 rods displayed similar adhesion levels as their equivalent spheres at all WSRs evaluated. Similar to particles with 2 μm ESD, when adhesion was normalized to particle flux, there was a significant decrease in the binding efficiency of 1 μm ESD spheres, AR-2 rods, and AR-4. The adhesion efficiency of AR-11 rods only slightly decreased (by ~25%) for the WSR increase from 500 s^{-1} to 1000 s^{-1} (data not shown).

In light of the adhesion trend shown in Figure 3.4A, we sought to determine if an increase in blood Hct would affect the adhesion trend for 1 μm ESD rods and spheres by conducting flow assays with a 40% Hct (Figure 3.4B) – reducing the height of the CFL and providing a better protective force normal to the HUVEC monolayer for particles near the vessel wall.[16] At 40% Hct, the adhesion level of AR-11 rods was significantly higher than equivalent spheres only at 500 and 1000 s^{-1}, whereas adhesion was higher than spheres at all WSR in 30% RBC flow. There was also no significant difference in the binding between spheres and AR-2 rods at any WSR examined in 40% RBC flow while AR-4 rods displayed higher binding than spheres only at the WSR of 1000 s^{-1}.

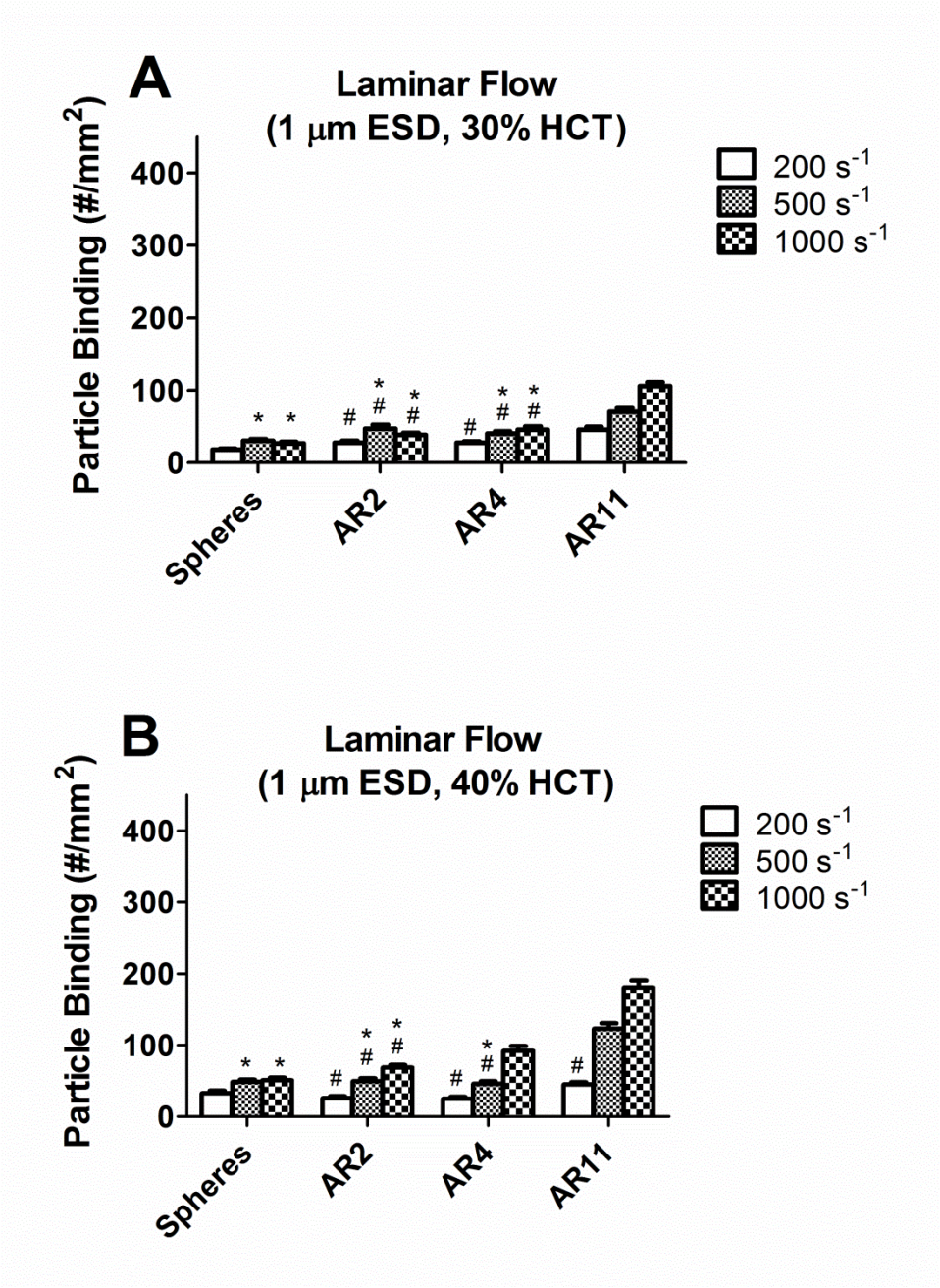

Figure 3.4 Adhesion density of spheres and rods (1 μm ESD) coated with a fixed sLe^a site density (970 ± 40 sites/μm^2) to activated ECs from 30% (A) and 40% (B) RBC in buffer following 3 min of steady flow at various shear rates through a PPFC. Particle concentration = 5 x 10^5 #/mL blood. * = not significant ($p > 0.01$) compared to adhesion of the same particle at the immediately lower WSR and # = not significant ($p > 0.01$) compared to adhesion of spheres at the same WSR via one-way ANOVA, $n \geq 3$.

Again, the increases in the binding of AR-11 rods relative to spheres was not solely a result of rods having more total copies of sLe^a, since assays performed at 40% Hct with a fixed total ligand number show that the adhesion of AR-11 rods remains significantly higher than that of spheres at both 500 s^{-1} and 1000 s^{-1} (Figure 3.5A). Also, localization of spheres and AR-11 rods to the CFL was visualized via confocal microscopy at the same 1000 s^{-1} WSR condition (30% Hct) used in the laminar adhesion assay shown in Figure 3.4A. Interestingly, the localization data indicated that the AR-11 rods with 1 μm ESD localized to the CFL at levels ~25% lower than equivalent spheres (Figure 3.5B), despite displaying adhesion levels greater than equivalent spheres. Also, as expected, the 1 μm ESD spheres localized to the CFL at levels ~42% less than 2 μm spheres.

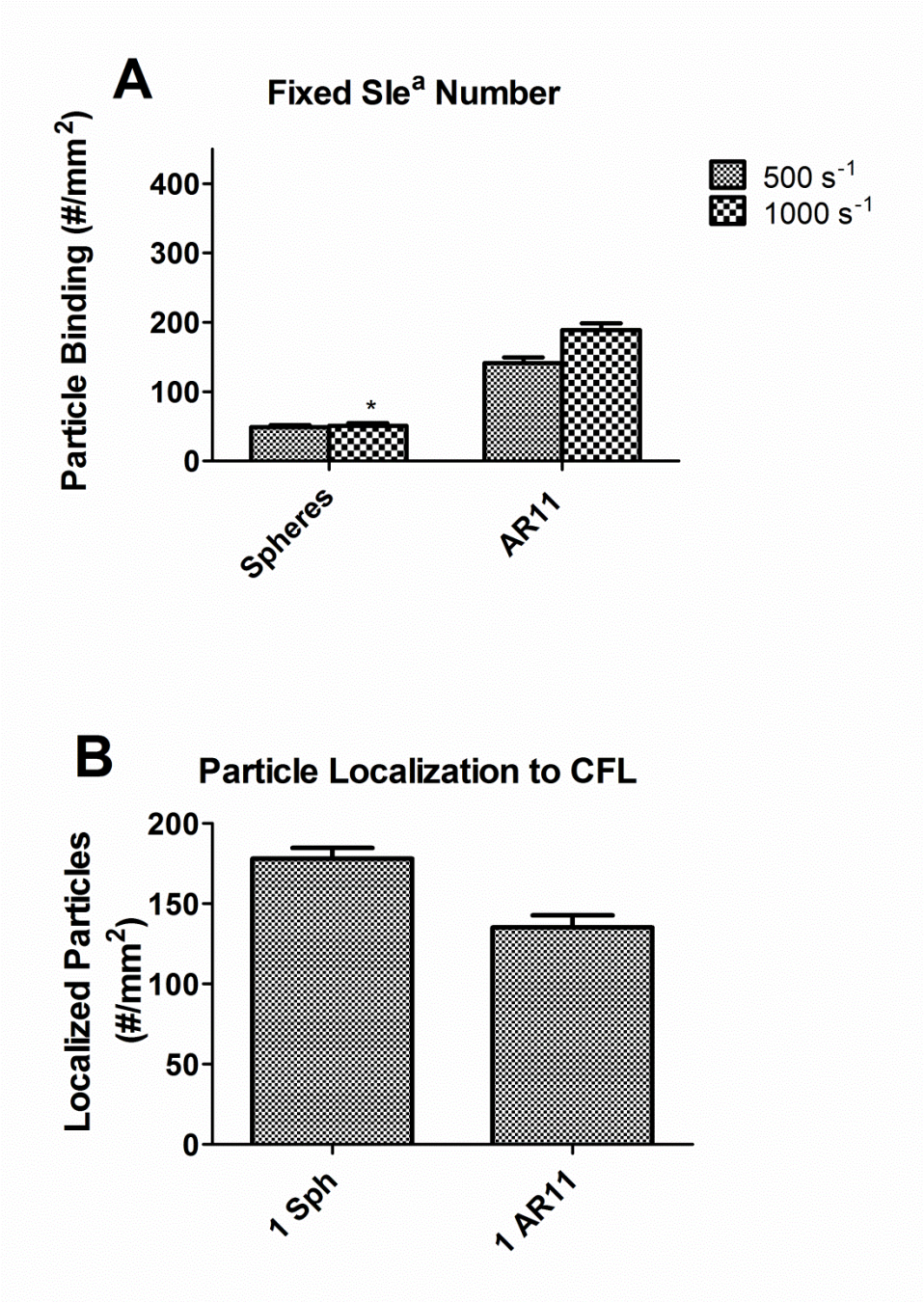

Figure 3.5 (A) Particle adhesion of spheres and aspect ratio (AR) 11 rods with 1 μm ESD from 30% RBC in buffer flow to activated ECs following a 3 min of steady flow through a PPFC with a fixed sLe^a number on all particles at a fixed particle concentration. Particles used in the fixed sLe^a number condition were coated with ~3100 sLea sites/particle. (B) Number of particles localized to the CFL from 30% Hct RBC in buffer flow in a PPFC at a WSR of $1000s^{-1}$ normalized to the square area of each confocal image analyzed. * = not significant ($p > 0.01$) compared to adhesion of same particle at the immediately lower WSR and # = not significant ($p > 0.01$) compared to adhesion of spheres at the same WSR via one-way ANOVA, $n \geq 3$.

Figure 3.6 shows the adhesion of spheres and rods with 500 nm ESD from 40% RBC in buffer after 3 min of laminar flow in a PPFC. Consistent with previous experimental work[1,2,5], the adhesion levels of nanoparticles were much lower than that of microparticles. Increasing the WSR did not result in a significant difference in the adhesion for any of the particle shapes. More importantly, the adhesion density of rods with 500 nm ESD was equal or lower than that of their equivalent spheres, regardless of aspect ratio. Indeed, the normalized data shows that the rods bound significantly less efficiently than spheres as the channel WSR increased (Figure 3.6B).

We see that although particle shape can improve particle adhesion, particle size is still an important factor in determining overall targeting, due to the ability or inability of particles to preferentially localize to the CFL in the presence of red blood cells. We investigated this RBC-enhanced localization effect with fluorescent 2 μm and 500 nm diameter spheres by imaging a near-wall focal plane in a PPFC using a confocal microscope and measuring the average fluorescent intensity of each image. Figure 3.7 shows the response in near-wall fluorescence caused by a 5X increase in particle concentration fed. In line with previous research, we see that in the presence of RBCs at a physiological Hct, increasing the particle concentration of 2 μm diameter spheres by 5X resulted in ~7.5X increase in fluorescence intensity. The same experiment but with 500 nm ESD only results in a ~3X increase in near-wall fluorescence. Also, increasing the 2 μm sphere concentration by 5X in blood results in a greater increase in near-wall fluorescence compared to in buffer flow, but increasing the 500 nm sphere concentration by 5X results in a greater increase in fluorescence in buffer flow rather than blood flow. This reinforces the importance of particle size in determining margination in the presence of RBCs, and is likely the reason non-spherical nanoparticles also show minimal binding in blood.

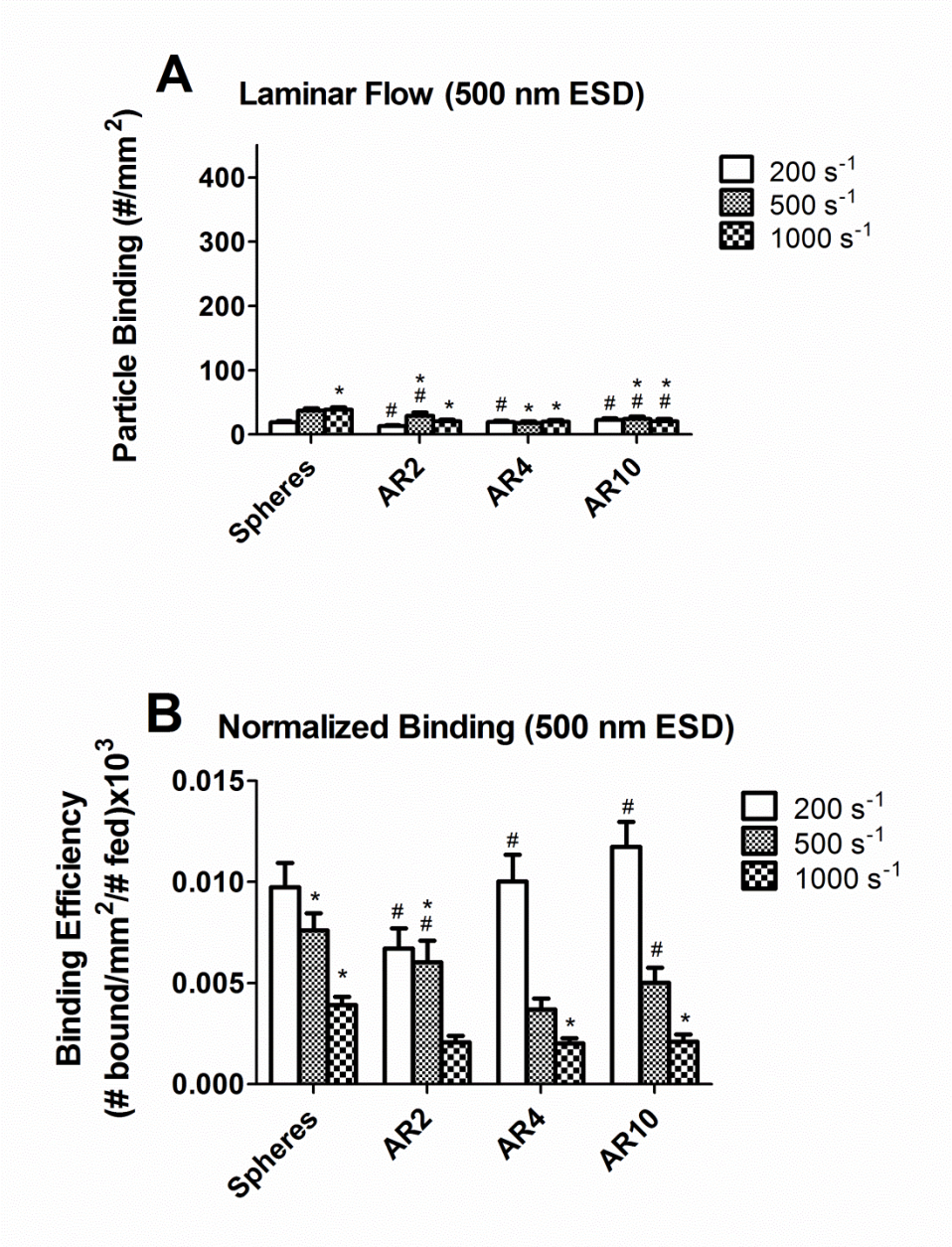

Figure 3.6 Adhesion density (A) and flux-normalized adhesion (B) of spheres and rods (500 nm ESD) coated with a fixed sLe^a density (970 ± 40 sites/μm^2) to activated ECs from 40% RBC in buffer following 3 min of steady flow at various shear rates through a PPFC. Particle concentration = 5 x 10^5 #/mL blood. * = not significant ($p > 0.01$) compared to adhesion of same particle at the immediately lower WSR and # = not significant ($p > 0.01$) compared to adhesion of spheres at the same WSR via one-way ANOVA, $n \geq 3$.

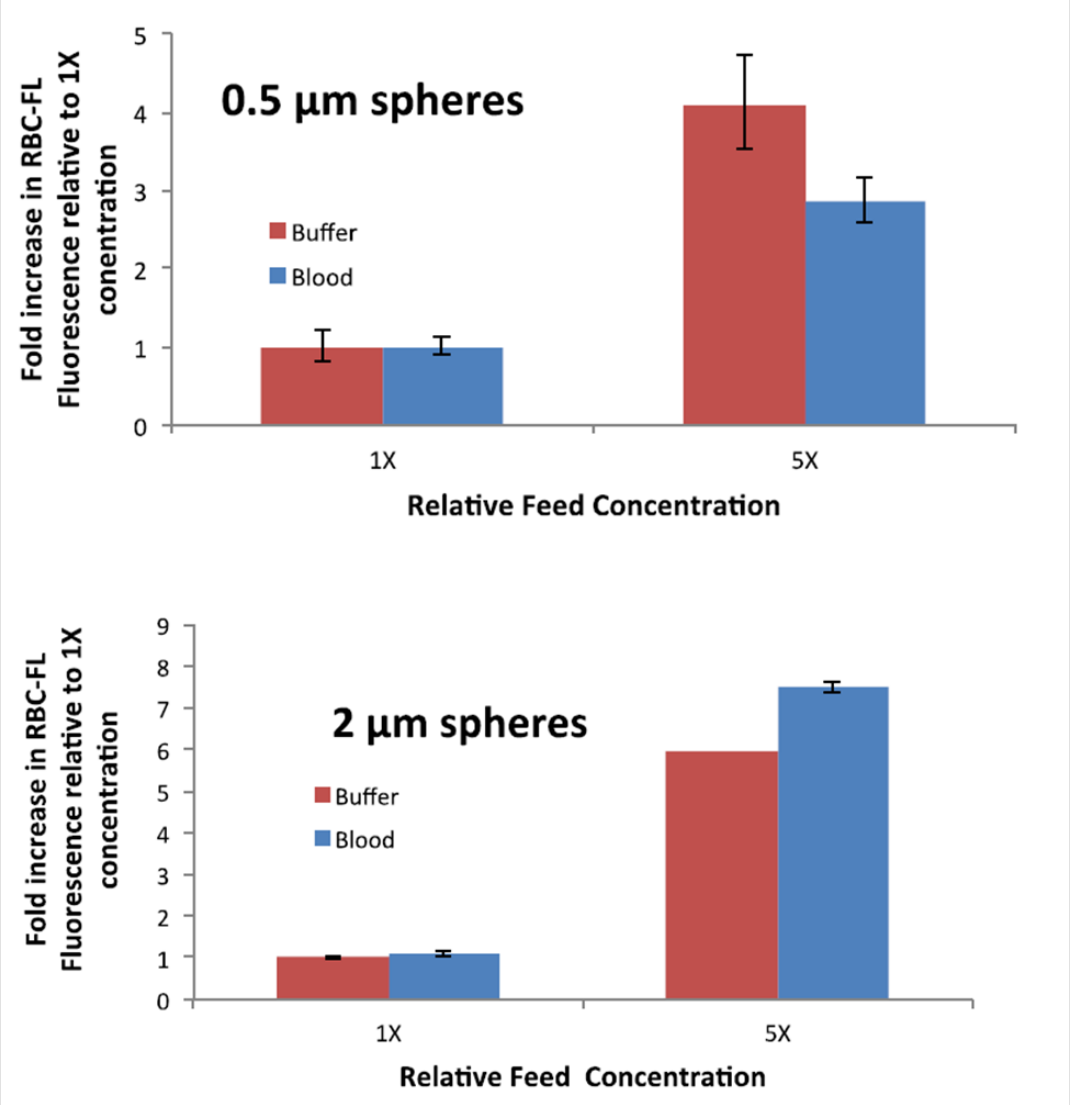

Figure 3.7 The ratio of fluorescence intensity of nanospheres (top) and microspheres (bottom) in the near-wall focal plane for the $5x10^5$ (1X) relative to the $2.5x10^6$ (5X) particles/mL feed concentrations in RBC in buffer flow at 30% Hct and in PBS++1%BSA flow at a WSR of 200 s^{-1} in a PPFC.[5]

Also of interest is whether disk shaped particles on the sub-micron or nano range would show improved adhesion compared to spheres. The disks were also prepared via heat-stretching, except they were stretched biaxially rather than uniaxially. The dimensions of the disks used in these experiments are listed in Table 3.2 (AR is calculated as the average of the widths divided by the thickness). Figure 3.8 shows the adhesion of disk shaped targeted particles with 1 μm and 500 nm ESD compared to spheres and rods of equivalent volume, while Figure 3.9 shows the adhesion of disks with 2 μm ESD compared to equivalent spheres. 1 μm ESD disks show increased adhesion compared to equivalent spheres, though no different from the 1 μm ESD rods discussed previously (AR-11). Also, 500 nm ESD disks did not adhere significantly higher than equivalent spheres. Disks with 2 μm ESD display a similar improvement in adhesion compared to equivalent spheres as was shown for high AR rod-shaped particles.

Table 3.2 Dimensions for disk-shaped particles used in adhesion experiments

Particle Shape	ESD [μm]	Width 1 [μm]	Width 2 [μm]	Thickness [μm]	Aspect Ratio
Disk	0.53	0.90	0.87	0.10	9.2
Disk	1.01	1.71	1.36	0.23	7.1
Disk	1.83	2.80	2.47	0.45	6.1

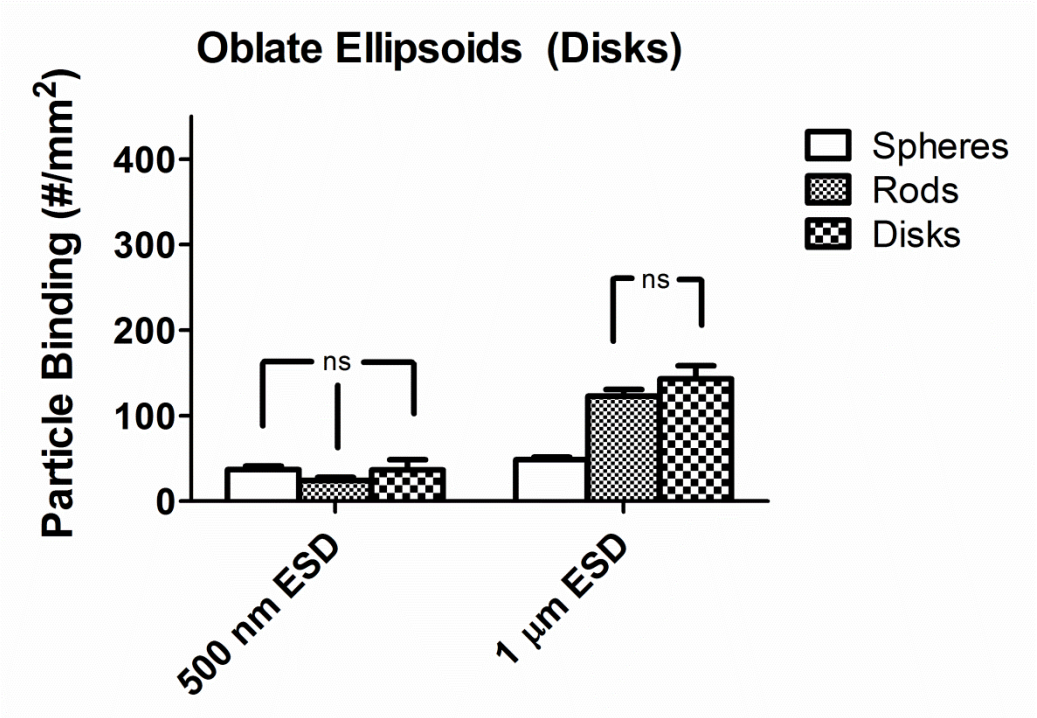

Figure 3.8 Adhesion density of targeted spheres, rods, and disks (1 μm and 500 nm ESD) to activated ECs from 40% RBC in buffer following 3 min of steady flow at a WSR of 500 s^{-1}. Particle concentration = 5 x 10^5 #/mL blood. ns = not significant ($p > 0.01$)

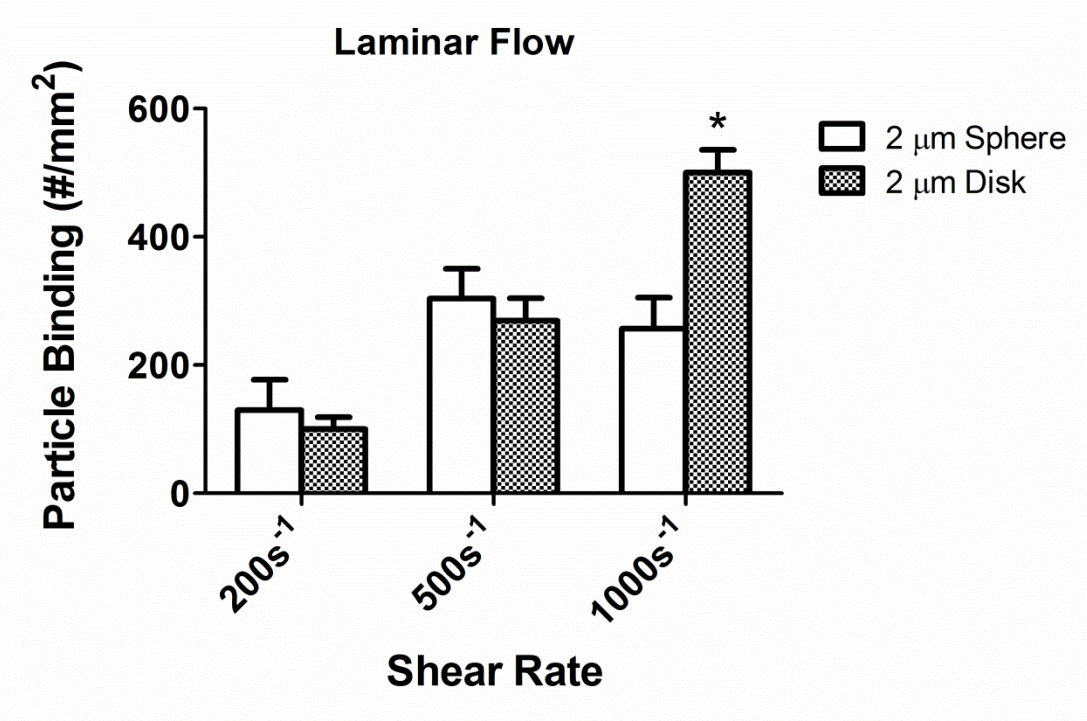

Figure 3.9 Adhesion density of targeted spheres and disks (2 μm ESD) to activated ECs from 40% RBC in plasma following 3 min of steady flow at varied WSR. Particle concentration = 5 x 10^5 #/mL blood. * indicates $p < 0.01$ comparing adhesion of spheres and disks at the same shear rate.

3.2.2 Particle adhesion in pulsatile blood flow

Particle adhesion was examined from two different pulsatile blood flow profiles at 40% Hct – (1) a forward flow at alternating low and high shear rates (120 s^{-1} – 1200 s^{-1}) and (2) alternating forward/reverse flow at high shear (1000 s^{-1}) with a net forward flow.[2] As shown in Figure 3.10, AR-9 rods with 2 μm ESD displayed over 130% higher adhesion compared to their equivalent spheres in both pulsatile profiles. There was no difference between the adhesion of 2 μm spheres and AR-2 rods, and a slightly higher adhesion level for AR-4 rods compared to spheres was observed only in the alternating low/high shear flow (Figure 3.10A). The adhesion trend seen for 1 μm ESD particles in pulsatile flow was similar to the trend seen for laminar flow, in which there was no difference in adhesion between spheres and rods of AR-2 or AR-4, but AR-11 rods adhere to HUVEC at ~140% higher levels than equivalent spheres in both pulsatile profiles. As with laminar flow assays, rods with 500 nm ESD in pulsatile flow showed either the same or slightly lower adhesion levels than 500 nm diameter spheres. Overall, adhesion of particles with 2 μm ESD was significantly higher than particles with 500 nm and 1 μm ESDs of similar shape in both pulsatile flow profiles explored – up to ~2500% for the longest AR rods.

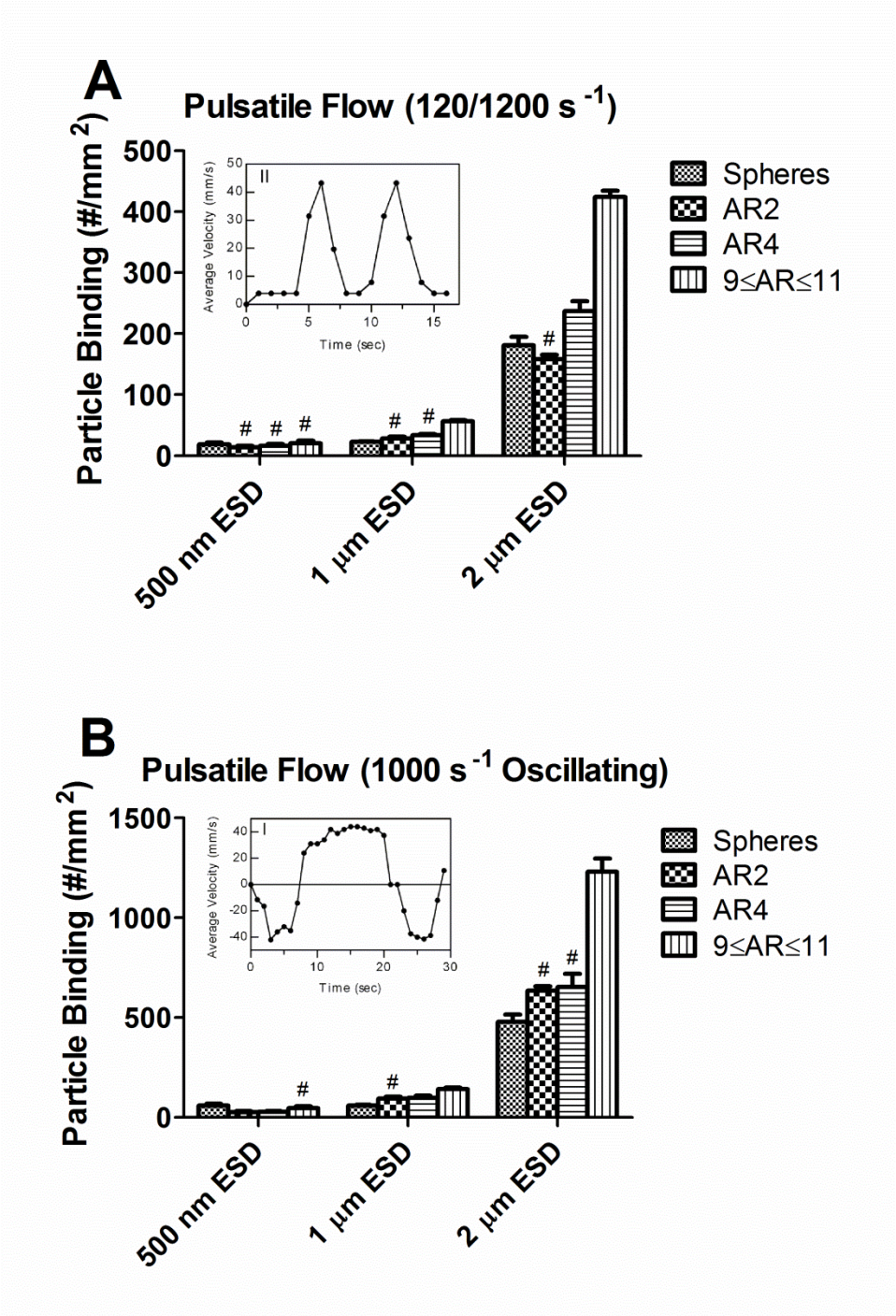

Figure 3.10 Adhesion of spheres and rods to activated ECs from (A) alternating low/high shear forward flow and (B) oscillating high shear flow profiles from 40% RBC in buffer at a particle concentration of 5 x 10^5 #/mL. Experiment times corresponded to 3 min of net forward flow (Total experiment times were 3 min for low/high flow and 9 min for oscillating flow). # = not significant ($p > 0.01$) compared to adhesion of spheres at the same size (ESD) via one-way ANOVA, $n \geq 3$.

3.2.3 Particle adhesion in recirculation blood flow

A step channel was used to examine particle adhesion from a recirculating flow profile. Figure 3.11 shows particle adhesion densities in the flow recirculation region, stagnation point, and far downstream of the stagnation point for particles having ESD of 2 μm. At 200 s^{-1} of shear (set to channel height downstream of flow expansion), adhesion at areas within the recirculation zone (see methods section) for 2 μm ESD particles showed no dependence on particle shape. In the disturbed flow region downstream of the stagnation point, only the adhesion density of AR-9 rods was higher than that of equivalent spheres (86% higher). Far downstream from the stagnation point where laminar flow is reestablished, the adhesion of AR-9 rods is also higher than equivalent spheres, though only 46% higher. With a downstream WSR of 500 s^{-1}, the adhesion density of AR-9 rods both upstream and downstream of the stagnation point and in the far downstream region was ~85% higher than that of equivalent spheres. Shorter (AR-2 and AR-4) rods displayed either slightly lower or no difference in their adhesion compared to spheres at both shear rates. Also, increasing the particle flux by a factor of 5/2 via higher WSR (comparing 500 s^{-1} versus 200 s^{-1} in Figure 3.11) only increased the far downstream adhesion of spheres by 85%, while the same increase in flux of AR-9 rods resulted in 140% higher adhesion – indicating either a better transport to the vessel wall or an improved capacity for adhesion.

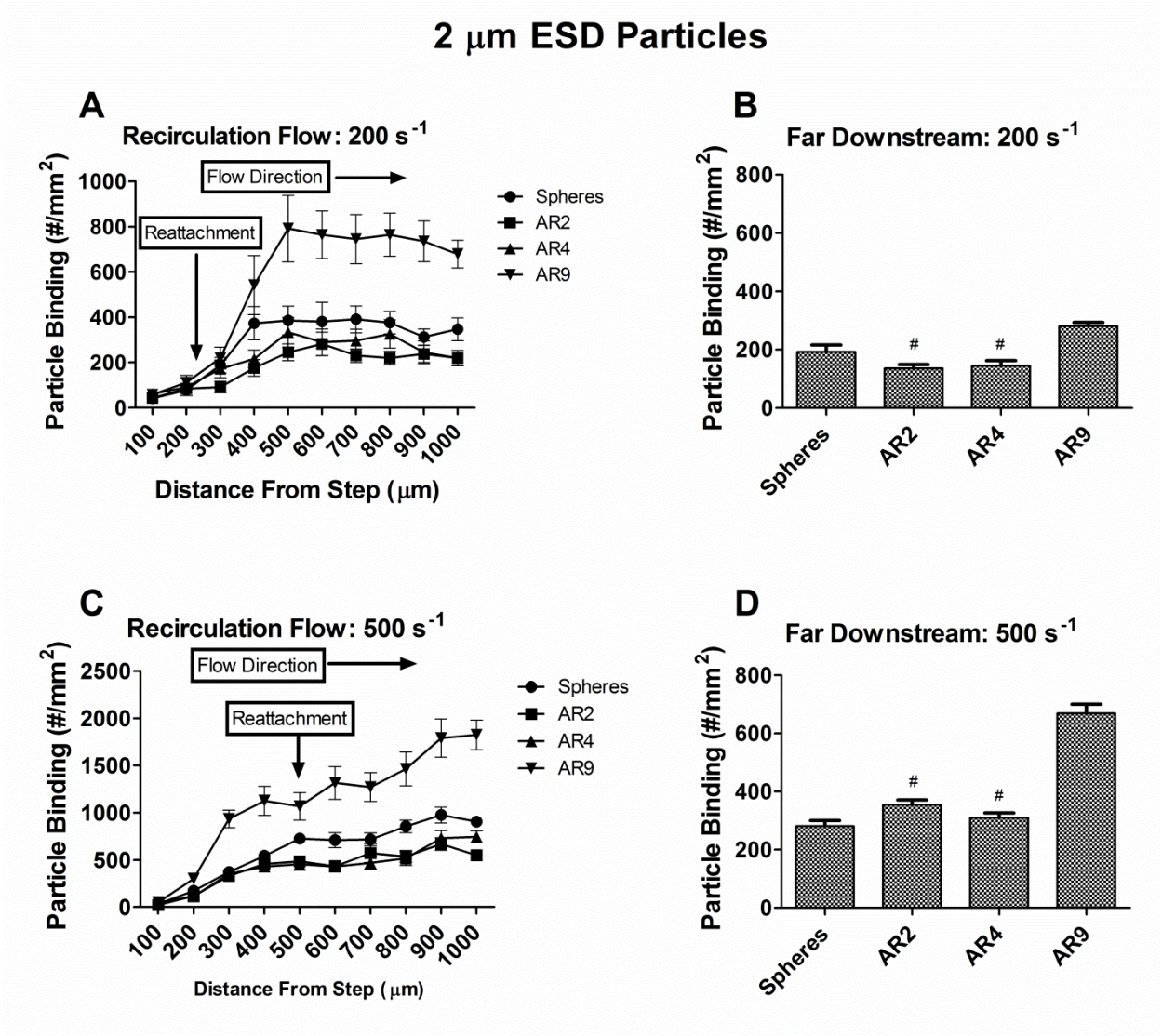

Figure 3.11 Adhesion of spheres and rods with 2 μm ESD to activated ECs from 40% RBC in buffer at a fixed particle concentration of 5 x 10^5 #/mL. Experiment was performed in a flow channel with a sudden expansion which causes recirculation flow to occur. Data is plotted as a function of the distance downstream of the sudden expansion. # = not significant ($p > 0.01$) compared to adhesion of spheres at the same WSR via one-way ANOVA, $n \geq 3$.

For 1 μm ESD particles, only AR-11 rods showed significantly higher adhesion than equivalent spheres in the region beyond the stagnation point for both downstream WSRs of 200 and 500 s^{-1} (Figure 3.12). However, note that even with recirculation flow, which could potentially cause redistribution of particles toward the vessel wall – the adhesion density of 1 μm ESD for all shapes was relatively low compared to particles with 2 μm ESDs.

For 500 nm ESD particles, similar to observation in laminar and pulsatile flows, adhesion in recirculating flow was minimal with no apparent improvement in adhesion due to particle shape or WSR (Figure 3.13).

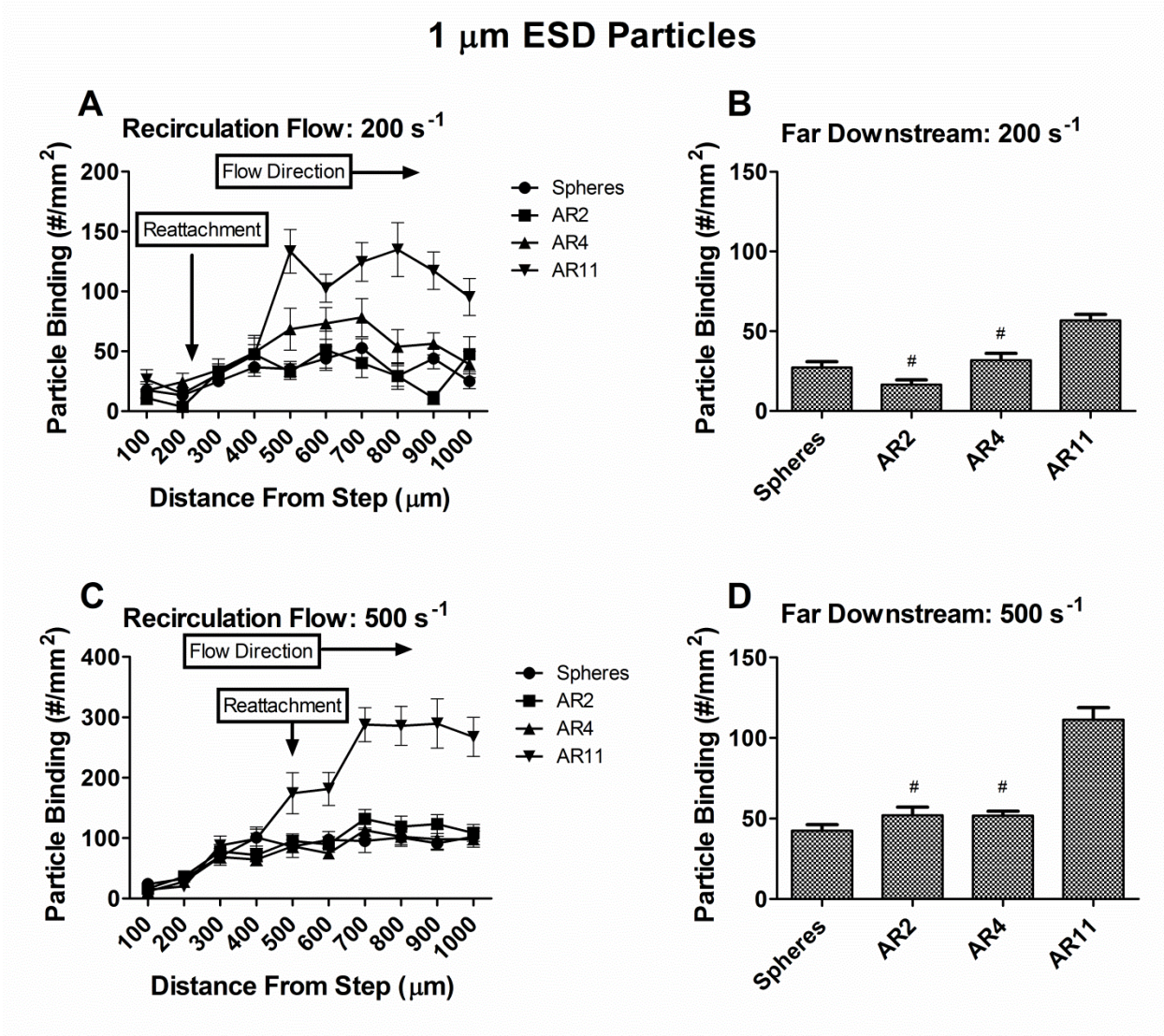

Figure 3.12 Adhesion of spheres and rods with 1 μm ESD to activated ECs from 40% RBC in buffer at a fixed particle concentration of 5 x 10^5 #/mL. Experiment was performed in a flow channel with a sudden expansion which causes recirculation flow to occur. Data is plotted as a function of the distance downstream of the sudden expansion. # = not significant ($p > 0.01$) compared to adhesion of spheres at the same WSR via one-way ANOVA, $n \geq 3$.

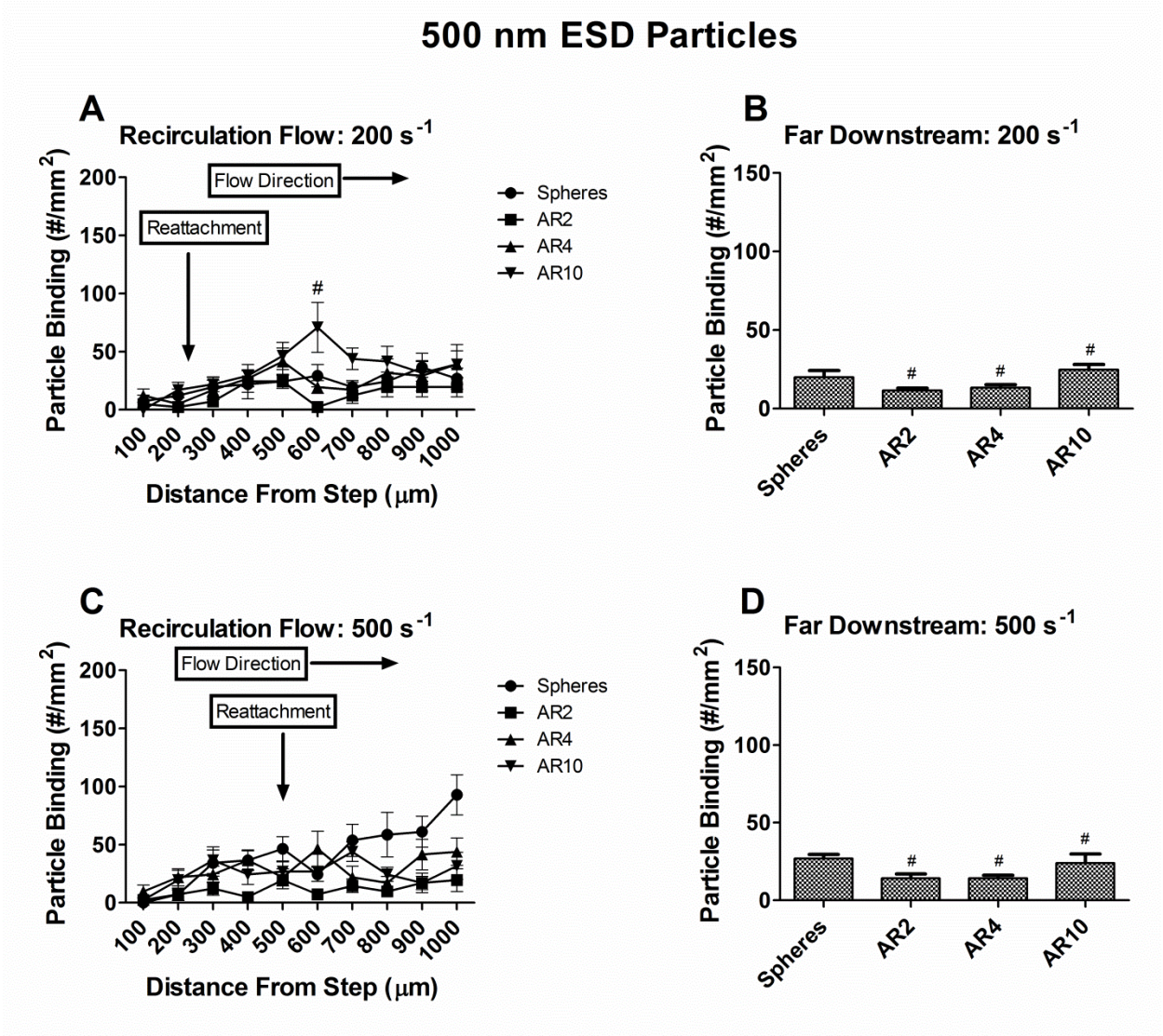

Figure 3.13 Adhesion of spheres and rods with 500 nm ESD to activated ECs from 40% RBC in buffer at a fixed particle concentration of 5 x 10^5 #/mL. Experiment was performed in a flow channel with a sudden expansion which causes recirculation flow to occur. Data is plotted as a function of the distance downstream of the sudden expansion. # = not significant ($p > 0.01$) compared to adhesion of spheres at the same WSR via one-way ANOVA, $n \geq 3$.

3.3 Discussion

Many parameters must be considered when designing vascular-targeted drug delivery systems. Previous works have investigated many different types of drug carriers, such as polymer matrices, liposomes, dendrimers, lipomers, microbubbles, etc.[17–25] Other studies have investigated bond strength and specificity of candidate ligand-receptor pairs.[26,27] Size has also been shown to have an effect on the margination of spheres to the CFL from blood flow.[1–4] Particle shape is a parameter that is similarly proposed to have an effect on the blood flow margination of drug carriers to the endothelium. However, limited experimental evidence exists in the literature to this end. In this study, we sought to examine the effect that particle shape parameters (volume, axis length, aspect ratio) have on the adhesion of vascular wall targeted rods and spheres from various physiological blood flow profiles via parallel plate flow chamber (PPFC) assays with an inflamed HUVEC monolayer lining the flow chamber wall. Overall, our data shows that rod-shaped particles having volume equal to or greater than a 1 μm spherical volume (ESD ≥ 1 μm) and with AR ≥ 9 displayed enhanced adhesion compared to their spherical counterparts at high shear rates in laminar, pulsatile, and recirculation flow profiles. At the largest particle volume explored (ESD = 2 μm), targeted rods with AR-9 showed over 2.2 fold more adhesion to the EC wall than equivalent spheres in laminar flow at a shear rate of 1000 s^{-1}. We find similar results for 2 μm ESD disks, which display significantly greater adhesion at 1000 s^{-1}, but no difference at lower shear rates. Spheres with 2 μm diameters, much like platelets, have been shown to be able to localize to the CFL efficiently in the presence of RBCs. Thus, the increase in adhesion seen for rods and disks with 2 μm ESD can in part be attributed to better adhesive properties, such as a larger contact area with the vascular wall compared to the other particles and a streamlined shape. This assertion is supported by the particle flux normalized

adhesion data (Figure 3.1B) – where the adhesion efficiency of 2 μm spheres in flow decreased as the WSR increased, while the adhesion efficiency of the AR-9 rods remained the same even at higher shear rates. Particle elongation increases the particle surface area in contact with the endothelium and thereby presents a greater number of targeting ligand (in this case sLe^a molecules) to the endothelium when particles had a fixed ligand site density. However, adhesion assays performed with a fixed total sLe^a number on 2 μm ESD particles indicate that the higher total number of sLe^a on rods is not the sole cause for the increased adhesion displayed by AR-9 rods in the fixed ligand density assays. Likely also important is the fact that the higher contact area with the endothelium exhibited by rods and disks distributes their adhesive force over a larger surface area, which would increase the shear force necessary to remove an adherent particle from the endothelium. Furthermore, the streamlined shape of ellipsoids reduces the removal force due to blood flow felt by these particles at the endothelium compared to an equivalent sphere. These combined effects have been predicted *in silico*[13] and shown in buffer flow adhesion assays[14,15] to improve particle adhesion dynamics.

Previous works have shown that spherical particles with diameters less than 2 μm do not effectively marginate to the vessel wall from bulk blood flow.[1–4] Our laminar flow data agrees with this in that under the same blood flow conditions, particles of all shapes with ESD ≤ 1 μm displayed significantly lower localization to the CFL, as visualized via confocal microscopy. Further, 2 μm diameter spheres in the presence of RBCs produced a greater than 1 to 1 response in near-wall fluorescence following an increase in particle concentration, while 500 nm diameter spheres produced a less than 1 to 1 response (Figure 3.7), indicating the importance of particle size in determining localization to the CFL. This translated to lower adhesion to the endothelium

than particles of the same shape with ESD of 2 μm for all WSR explored, despite being fed into the PPFC at the same concentration.

More importantly, most rods with ESD ≤ 1 μm evaluated in laminar RBC flow displayed the same or slightly worse adhesion density than equivalent spheres. However, the highest aspect ratio rods having 1 μm ESD (AR-11) displayed significantly higher adhesion than equivalent spheres; in this case over the entire range of shear rates investigated at 30% Hct and over 3 times higher than spheres at 1000 s^{-1}. At 40% Hct, adhesion between AR-11 rods and equivalent spheres was not significantly different at 200 s^{-1} WSR because the decreased CFL size caused the spheres adhesion level to improve to that shown for AR-11 rods. It seems likely that for 1 μm ESD particles, the rod shape – in addition to the favorable adhesion characteristics mentioned in the previous paragraph – improves particle transport to the vessel wall compared to spheres. This assertion is supported by the 2 – 2.5 times higher adhesion for AR-11 rods at the lowest WSR explored with 30% Hct, a condition in which adhesion is not expected to be reaction-limited.[1] In this case, the higher surface contact area exhibited by AR-11 rods and their streamlined shape that enhance reaction kinetics are expected to be inconsequential as was the case for 2 μm ESD particles at this condition (Figure 3.1, 200 s^{-1} WSR). Two possibilities seem likely for this improved adhesion density for the AR-11 rods: (1) more of these rods may be excluded from the RBC core and into the CFL, i.e. they exhibit enhanced near-wall excess and/or (2) particles already within or near the CFL could better initiate contact with the vessel wall compared to particles with shorter axis lengths due to their major axis (~6 μm major axis for AR-11, 1 μm ESD rods) being on the order of CFL size[28], thus resulting in greater adhesion probability. When localization was imaged using confocal microscopy, less AR-11 rods were seen in the CFL than equivalent spheres under the same conditions that enhanced adhesion of

AR-11 was observed – indicating that the second possibility is most likely the reason for the improved adhesion of AR-11 rods with 1 μm ESD compared to equivalent spheres at low shear rate. The higher probability of contact for rods already within the CFL also agrees with the notion that rods in shear flow exhibit a lateral drift, which reduces margination time resulting in enhanced adhesion.[11,12]

Blood flow in areas of the vasculature where atherosclerotic plaques preferentially accumulate is often characterized by disturbed flow profiles including high pulsatility, low net shear due to reverse flow, and recirculation eddies near areas of bifurcations or high curvature. For this reason, adhesion experiments were performed in these relevant disturbed flow profiles. The disturbed flow assays revealed similar trends as was seen in laminar, steady flow. Compared to spheres with a 2 μm diameter, the AR-9 rods with 2 μm ESD exhibited the highest positive differential in adhesion from recirculating flow as well as in both pulsatile flow profiles (characterized by either alternating low/high shear forward flow or alternating forward/reverse high shear flow). Similarly, only AR-11 rods with 1 μm ESD displayed a robust improvement in adhesion relative to spheres in recirculating and both pulsatile flow profiles evaluated. Again, shape did not improve adhesion compared to spheres for particles with 500 nm ESD in disturbed flow patterns despite conditions which allow particles more residence time within the flow chamber (Figure 3.10B) and particle redistribution to the wall (recirculation flow).[2]

Overall, it is possible that a minimum major axis length for rods, rather than a minimum aspect ratio, is requisite for enhanced transportation to the wall, much like it has been shown that a minimum particle diameter is required for effective margination of spheres (~2 μm diameter). Of the 500 nm ESD particles used in this study, the highest aspect ratio rod evaluated (AR-10) had a major axis of 2.4 μm. Even at this high aspect ratio, the adhesion was minimal as it was

for all 500 nm particles investigated. Meanwhile, the major axis length for the 1 μm ESD rods (AR-11) that displayed enhanced adhesion compared to spheres was ~6 μm. Also, 1 μm ESD rods with a major axis of 2.76 μm (AR-4) did not consistently show significant positive differential in binding relative to spheres under the flow conditions explored. In line with our observations, Decuzzi *et al* presented a model which predicts that the lateral drift velocity of discoidal particles increases, i.e. faster collision with the wall, with increased particle elongation[11]; however, this work did not explicitly include high aspect ratio nanoparticles with a micrometer scale major axis dimension as was evaluated here. Our current rod fabrication technique limits our capacity to fabricate rods of 500 nm ESD with major axis greater than 2.5 μm and thus limits our capacity to test this hypothesis in this work.

Finally, it remains possible that particles of other non-spherical shapes having volume in the nanometer ESD range may exhibit enhanced margination in blood relative to equivalent spheres. For instance, Decuzzi and co-workers recently showed that nanodisks in low shear buffer flow exhibit ~2 fold increased adhesion over rods of equal volume due to slightly higher hydrodynamic forces exerted on the rods compared to disks and the larger surface for adhesion exposed by disks relative to rods.[15] However, our results show no indication that disks provide improvement over spheres or rods at the 500 nm or 1 μm ESD size when in the presence of RBCs. Overall, the presented work shows that indeed particle shape can affect particle margination, thus should be considered in the design of VTCs.

References

1. Charoenphol, P., Huang, R. B. & Eniola-Adefeso, O. Potential role of size and hemodynamics in the efficacy of vascular-targeted spherical drug carriers. *Biomaterials* **31,** 1392–1402 (2010).

2. Charoenphol, P. *et al.* Targeting therapeutics to the vascular wall in atherosclerosis-Carrier size matters. *Atherosclerosis* **217,** 364–370 (2011).

3. Tilles, A. W. & Eckstein, E. C. The near-wall excess of platelet-sized particles in blood flow: its dependence on hematocrit and wall shear rate. *Microvasc. Res.* **33,** 211–223 (1987).

4. Eckstein, E. C., Tilles, A. W. & Millero 3rd, F. J. Conditions for the occurrence of large near-wall excesses of small particles during blood flow. *Microvasc Res* **36,** 31–39 (1988).

5. Namdee, K., Thompson, A. J., Charoenphol, P. & Eniola-Adefeso, O. Margination propensity of vascular-targeted spheres from blood flow in a microfluidic model of human microvessels. *Langmuir* **29,** 2530–2535 (2013).

6. Champion, J. A. & Mitragotri, S. Shape induced inhibition of phagocytosis of polymer particles. *Pharm. Res.* **26,** 244–249 (2009).

7. Champion, J. A. & Mitragotri, S. Role of target geometry in phagocytosis. *Proc Natl Acad Sci U S A* **103,** 4930–4934 (2006).

8. Decuzzi, P. *et al.* Size and shape effects in the biodistribution of intravascularly injected particles. *J Control Release* **141,** 320–327 (2010).

9. Geng, Y. *et al.* Shape effects of filaments versus spherical particles in flow and drug delivery. *Nat Nanotechnol* **2,** 249–255 (2007).

10. Muro, S. *et al.* Control of endothelial targeting and intracellular delivery of therapeutic enzymes by modulating the size and shape of ICAM-1-targeted carriers. *Mol Ther* **16,** 1450–1458 (2008).

11. Lee, S. Y., Ferrari, M. & Decuzzi, P. Shaping nano-/micro-particles for enhanced vascular interaction in laminar flows. *Nanotechnology* **20,** (2009).

12. Gavze, E. & Shapiro, M. Motion of inertial spheroidal particles in a shear flow near a solid wall with special application to aerosol transport in microgravity. *J. Fluid Mech.* **371,** 59–79 (1998).

13. Decuzzi, P. & Ferrari, M. The adhesive strength of non-spherical particles mediated by specific interactions. *Biomaterials* **27,** 5307–5314 (2006).

14. Doshi, N. *et al.* Flow and adhesion of drug carriers in blood vessels depend on their shape: A study using model synthetic microvascular networks. *J. Control. Release* **146,** 196–200 (2010).

15. Adriani, G. *et al.* The preferential targeting of the diseased microvasculature by disk-like particles. *Biomaterials* **33,** 5504–5513 (2012).

16. Charoenphol, P., Onyskiw, P. J., Carrasco-Teja, M. & Eniola-Adefeso, O. Particle-cell dynamics in human blood flow: implications for vascular-targeted drug delivery. *J Biomech* **45,** 2822–2828 (2012).

17. Backer, M. V *et al.* Vascular endothelial growth factor selectively targets boronated dendrimers to tumor vasculature. *Mol. Cancer Ther.* **4,** 1423–1429 (2005).

18. Unger, E., Porter, T., Lindner, J. & Grayburn, P. Cardiovascular drug delivery with ultrasound and microbubbles. *Adv. Drug Deliv. Rev.* **72,** 110–126 (2014).

19. Ting, C. Y. *et al.* Concurrent blood-brain barrier opening and local drug delivery using drug-carrying microbubbles and focused ultrasound for brain glioma treatment. *Biomaterials* **33,** 704–712 (2012).

20. Nance, E. *et al.* Brain-Penetrating Nanoparticles Improve Paclitaxel Efficacy in Malignant Glioma Following Local Administration. *ACS Nano* (2014). doi:10.1021/nn504210g

21. Shuvaev, V. V. *et al.* Endothelial targeting of antibody-decorated polymeric filomicelles. *ACS Nano* **5,** 6991–6999 (2011).

22. Kamaly, N., Xiao, Z., Valencia, P. M., Radovic-Moreno, A. F. & Farokhzad, O. C. Targeted polymeric therapeutic nanoparticles: design, development and clinical translation. *Chem. Soc. Rev.* **41,** 2971 (2012).

23. Muro, S. *et al.* Endothelial targeting of high-affinity multivalent polymer nanocarriers directed to intercellular adhesion molecule 1. *J. Pharmacol. Exp. Ther.* **317,** 1161–1169 (2006).

24. Allen, T. M. Long-circulating (sterically stabilized) liposomes for targeted drug delivery. *Trends Pharmacol. Sci.* **15,** 215–220 (1994).

25. Allen, T. M. & Cullis, P. R. Liposomal drug delivery systems: From concept to clinical applications. *Adv. Drug Deliv. Rev.* **65,** 36–48 (2013).

26. Byrne, J. D., Betancourt, T. & Brannon-Peppas, L. Active targeting schemes for nanoparticle systems in cancer therapeutics. *Adv. Drug Deliv. Rev.* **60,** 1615–1626 (2008).

27. Eniola, A. O., Krasik, E. F., Smith, L. A., Song, G. & Hammer, D. A. I-domain of lymphocyte function-associated antigen-1 mediates rolling of polystyrene particles on ICAM-1 under flow. *Biophys. J.* **89,** 3577–3588 (2005).

28. Sharan, M. & Popel, A. S. A two-phase model for flow of blood in narrow tubes with increased effective viscosity near the wall. *Biorheology* **38,** 415–428 (2001).

CHAPTER 4: SHAPE EFFECTS ON THE IN VIVO TARGETING AND BIODISTRIBUTION OF ELLIPSOIDAL PARTICLES IN ATHEROSCLEROTIC MICE

This work is a collaboration with Katawut Namdee, and is published as K Namdee[*], AJ Thompson[*], A Golinski, S Mocherla, D Bouis, and O Eniola-Adefeso. *In vivo* evaluation of vascular-targeted spheroidal microparticles for imaging and drug delivery application in atherosclerosis. *Atherosclerosis* 237 (1), 279-286 (2014).[1] *Authors had equal contribution to this work.

ABSTRACT

Vascular-targeting is a promising strategy for improving the diagnosis and treatment of coronary artery disease (CAD) by providing localized delivery of imaging and therapeutic agents to sites of atherosclerosis. Targeting particles to atherosclerosis is especially challenging in that particles must be able to marginate to the endothelium in relatively large vessels and in the presence of high shear rates due to blood flow. In this work we evaluate how particle size and shape affects the capacity of a vascular-targeted carrier system to bind to inflamed endothelium over plaque using ApoE-/- mice with developed atherosclerosis. Spherical and prolate ellipsoidal particles with either 500 nm or 2 μm equivalent spherical diameters (ESD) targeted to the inflammatory receptors E-selectin and VCAM-1 were injected via tail-vein and allowed to circulate for 30 min. The entire aorta and major organs (lung, liver, spleen, and kidney) were excised and analyzed for particle targeting and accumulation. We found that targeted ellipsoidal

microparticles adhered to mouse aortae at higher levels than microspheres of similar volume, particularly at segments that contained atherosclerotic plaques. Moreover, both ellipsoidal and spherical nanoparticles displayed the same minimal adhesion levels compared to both types of microparticles evaluated, likely due to poor localization of nanoparticles to the vessel wall in blood flow. We found that microparticles targeted to plaque-associated inflammation were retained at higher levels in the lungs than untargeted particles, largely due to molecular interaction with the pulmonary endothelium. The level of mechanical entrapment of ellipsoidal microparticles in the lungs was also not significantly different from that of microspheres of the same volume despite a 3 fold higher major axis length for the ellipsoids. This study confirms that particle shape and size should be considered in designing carrier systems to target atherosclerosis, as these parameters can be tuned to improve carrier performance.

4.1 Introduction

Vascular-targeted carriers is a promising potential strategy for improving treatment of atherosclerosis because specific vascular wall endothelial cell receptors associated with acute and chronic inflammation (selectins, ICAM-1, VCAM-1) play a major role in the pathology of this disease. Naturally, these receptors then also provide a convenient and accessible platform for vascular targeting. Current vascular-targeting strategies in coronary artery disease (CAD) typically involve coating injectable carriers with targeting moieties for specific interaction with the relevant endothelial expressed receptors, providing these carriers the ability to navigate the vasculature, adhere, and persist locally in the diseased tissue. Overall, the ability to provide highly localized delivery to atherosclerotic pre-lesions or fully formed plaques in CAD can offer new therapeutic avenues for early diagnosis and treatment of this disease.[2]

Many variants of VTCs have been investigated for use as a diagnostic or therapeutic, such as polymer particles, liposomes, dendrimers, and polymersomes; which are typically spherical with nanoscale diameters.[3] However, particle shape and size have recently been presented as tunable parameters for enhancing the vascular wall interaction of VTCs at a targeted site in the presence of blood flow.[4–6] Numerous mathematical and some simple flow experimental models show that ellipsoidal particles can display greater deposition/adhesion compared to spherical particles of the same volume.[7–10] Our recent *in vitro* study (Chapter 3) also shows that under physiological levels of shear, prolate ellipsoidal (rod-like) particles targeted to inflammation display higher levels of adhesion compared to spheres in the presence of human RBCs in parallel plate flow chamber assays, provided that the equivalent spherical diameter (ESD) of the rods is ≥ 1 μm.[11] To our knowledge, the *in vivo* study presented here is the first to compare adhesion of spherical and ellipsoidal polymer VTCs within the context of targeting atherosclerotic plaques in

CAD. The areas of the vasculature vulnerable to atherosclerosis tend to be large vessels (on the order of centimeters in diameter in humans), which make the successful localization of VTCs to the vascular wall increasingly important in determining their overall performance. Further, these atheroprone areas tend to exhibit pulsatile and disturbed blood flow profiles which are very different in terms of hemodynamics compared to the microvasculature, where much of the previous vascular targeting research has been focused.[12] Here, we evaluate the role that the size and shape of particles has on their capacity to effectively reach and bind to inflamed aorta using a mouse model of atherosclerosis. Specifically, we investigated the adhesion levels of prolate ellipsoidal and spherical particles along sections of the aorta from the aortic root to the iliac branches, and the effect of the targeting ligands on the biodistribution of spherical and ellipsoidal particles in major organs. Particles were dual-targeted to the inflammatory receptors E-selectin and VCAM-1, which are proteins known to be overexpressed by the endothelium in atherosclerosis.[13–15] A dual-targeting approach is employed based on previous publications that suggest *in vivo* selectivity to ECs over plaque in ApoE -/- mice is greatest when both VCAM-1 and selectin were targeted.[16,17] We found that targeted rod-shaped microparticles adhered to mouse aortae at overall higher levels than spherical microparticles, particularly at segments of the aorta that contained developed or developing plaques. There was no difference in the adhesion of rod-shaped and spherical nanoparticles, which was minimal to the adhesion of microparticles.

4.2 Results

Prolate ellipsoidal particles were fabricated using a previously described[11,18,19] polymer film stretching method before coating the surface with sLe^a and aVCAM-1 to target E-selectin and VCAM-1, respectively (see Chapter 2). Particles were administered to 20 week old mice at

a dosage of 20 x 10^6 particles per mouse via the tail-vein and allowed to circulate for 30 min before analyzing particles adherent to the aorta and particle biodistribution.

4.2.1 Particle adhesion to aorta

As in Chapter 3, we are interested in exploring which aspect ratio (AR) results in the best targeting, in this case to inflamed aorta. In order to determine the effect that AR has on targeting ability, targeted rods of three different ARs (2, 4, 9) with 2 μm ESD as well as 500 nm and 2 μm spheres were prepared. Figure 4.1 shows the SEM images and Table 4.1 gives the dimensions of the 2 μm rods and equivalent spheres used to test the effect of AR on targeting in mice.

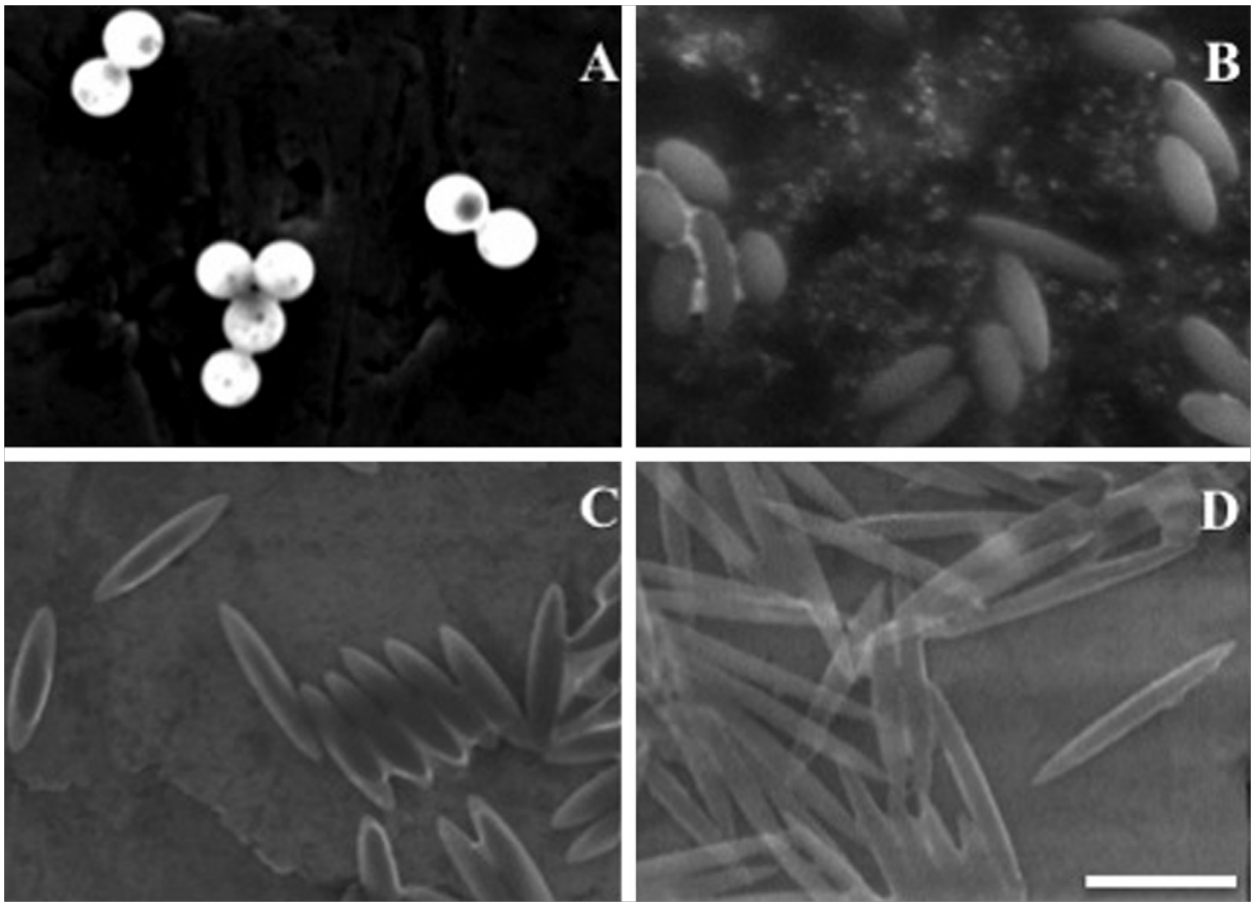

Figure 4.1 SEM Images of 2 μm ESD polystyrene (A) spheres, (B) AR-2 rods, (C) AR-4 rods, and (D) AR-9 rods used to test the effect of aspect ratio on particle adhesion to the aorta in ApoE-/- mice. Scale bar = 5 μm.

Table 4.1 Dimensions of particles used to test the effect of AR on particle adhesion.

Particle Shape	ESD (μm)	Aspect Ratio	Major Axis (μm)	Minor Axis (μm)
Sphere	**2.07**	1.00	2.07	2.07
AR-2		2.25	3.55	1.58
AR-4		4.46	5.61	1.26
AR-9		9.45	9.25	0.98

Following tail-vein injection into ApoE-/- mice, adhesion of each particle type to the aorta was quantified and normalized to the average amount of adherent 500 nm diameter spheres (Figure 4.2). The adhesion of the AR4 rods was the highest (~3 times higher) relative to their equivalent microspheres. Adhesion of AR2 rods was roughly the same as 2 μm spheres, likely because of the relatively small difference in shape and surface area between these two shapes. Adhesion of AR9 rods was statistically the same as the 2 μm spheres and lower than that of AR4 rods, despite displaying the highest adhesion in the *in vitro* human blood assays (Chapter 3). This change in optimum AR is potentially due to increased entrapment of AR9 rods in the capillaries as they have a major axis length of roughly 9 μm. Also, mouse RBCs have different characteristics compared to human RBCs such as diameter, volume, and tendency to form RBC aggregates; which could affect which particle AR is ideal for margination and adhesion.

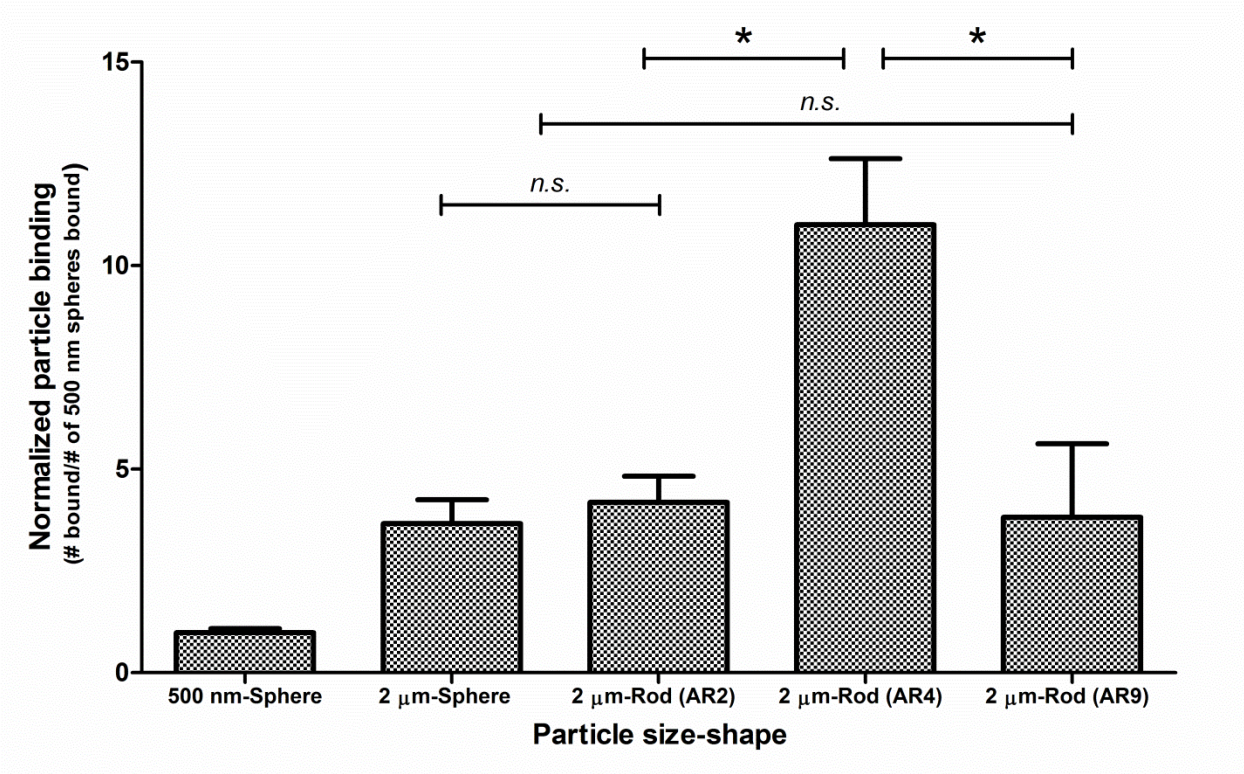

Figure 4.2 Ratio of the binding (normalized to 500 nm diameter sphere) of sLe^a and anti-VCAM coated particles of various AR on ApoE-/- mouse aortae after 30 min circulation via tail-vein injection. (* = $p < 0.05$ and n.s. = not significant via one-way ANOVA, $n \geq 3$).

Given the results in Figure 4.2, the following adhesion experiments were performed with the highest binding 2 μm rods (AR4), as well as 2 μm spheres, 500 nm spheres, and 500 nm rods with AR6. Figure 4.3 shows the average cumulative particle adhesion along the entire length of the aortic tree normalized to the adhesion of 500 nm spheres, from the ascending aorta to the iliac branching points. Particles with 2 μm ESD displayed significantly higher adhesion densities, at least 4 fold, compared to particles with 500 nm ESD. When adhesion data is normalized for particle volume (relevant for drug loading), the cumulative volume delivered by adherent microparticles is ~500-1500 fold higher than the volume of adherent nanoparticles depending on particle shape (Figure 4.4). Nanorods displayed no increased adhesion compared to their equivalent 500 nm diameter spheres. Control experiments with targeted 2 μm spheres injected into wild type mice or 2 μm IgG-coated particles (spheres and AR4 rods) injected into ApoE-/- mice show minimal accumulation in the aorta, suggesting that the high adhesion of targeted microparticles observed in the aorta of ApoE-/- mice are due to the expression of the targeted inflammatory molecules on the endothelium.

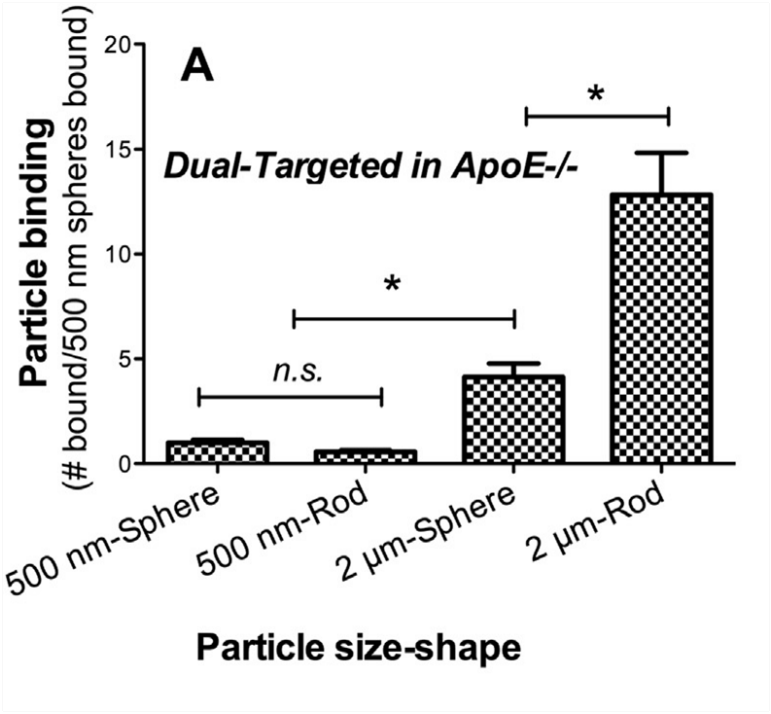

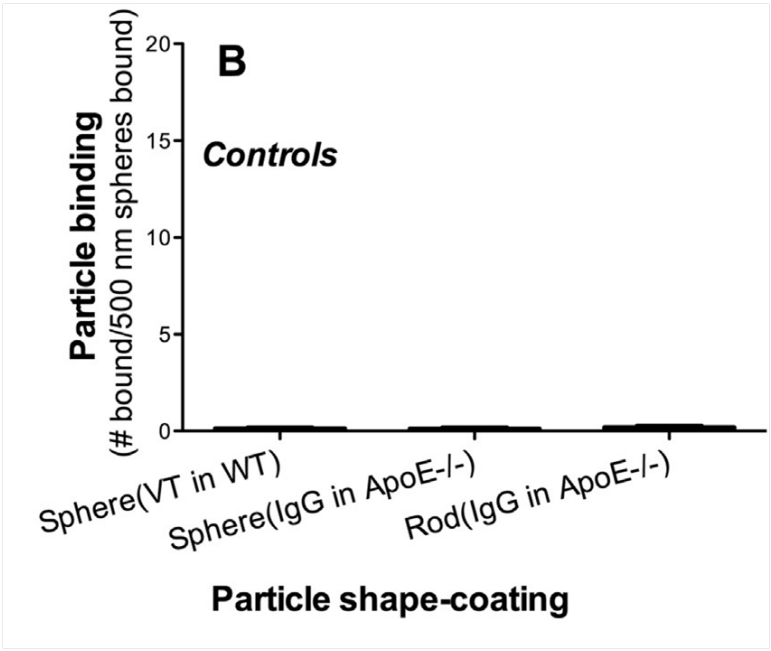

Figure 4.3 (A) Ratio of the adhesion of sLe^a and anti-VCAM targeted particles on ApoE-/- mouse aortae following 30 min circulation via tail-vein injection. AR = 6 and 4 for rods with ESD of 500 nm and 2 µm, respectively (* = $p < 0.05$ with respect to 2 µm microspheres and n.s. = not significant via one-way ANOVA, $n \geq 5$). (B) Ratio of the adhesion of sLe^a and anti-VCAM targeted 2 µm spheres to wild-type mouse aortae or of IgG-coated 2 µm spheres and rods (AR4) to ApoE-/- mouse aortae following 30 min circulation via tail-vein injection.

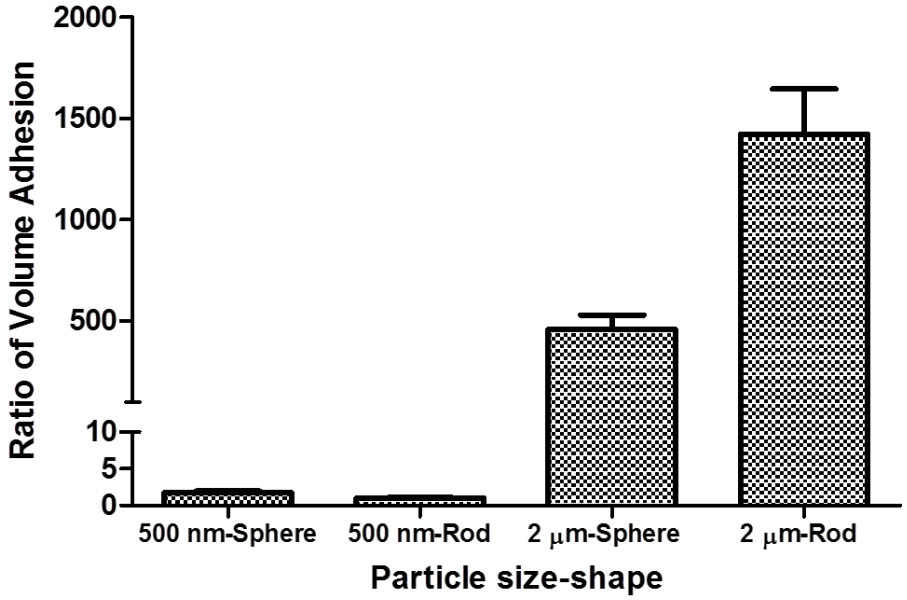

Figure 4.4 Ratio of volume binding (normalized to 500 nm ESD rod) of sLe^a and anti-VCAM coated particle binding on ApoE-/- mouse aorta after 30 min circulation via tail-vein injection, $n \geq 5$.

It is established that atheroprone areas of the aorta are typically near vessel bifurcations or curvature, whereas the blood flow profiles along straight sections of the aorta tend to be atheroprotective.[20–22] Therefore, we also quantified the adhesion density of targeted particles along different sections of the aorta from the ascending aorta to the iliac branches. At each section investigated, the adhesion density of 2 μm rods was greater than or equal to the adhesion of equivalent spheres (Figure 4.5). Interestingly, the adhesion density of targeted microrods relative to microspheres and nanoparticles was greatest around the combined area of the brachiocephalic, right common carotid, and right subclavian branching points near the aortic arch, followed by the thoracic aorta and to a lesser extent the descending aorta. Visual inspection revealed developed/developing plaques near many of the branched and curved regions of the vasculature. Qualitatively, adhesion of targeted particles was higher on or near these regions of plaque formation. As shown in Figure 4.6, a representative Hoecsht (nucleus) and wheat germ agglutinin (plasma membrane) staining of a segment of the aorta with visible plaque, more microparticles were bound around the periphery of the developing plaque than on the top. Overall, adhesion was minimal for nanoparticles throughout the aorta compared to microparticles, even in areas where very high levels of inflammation are expected

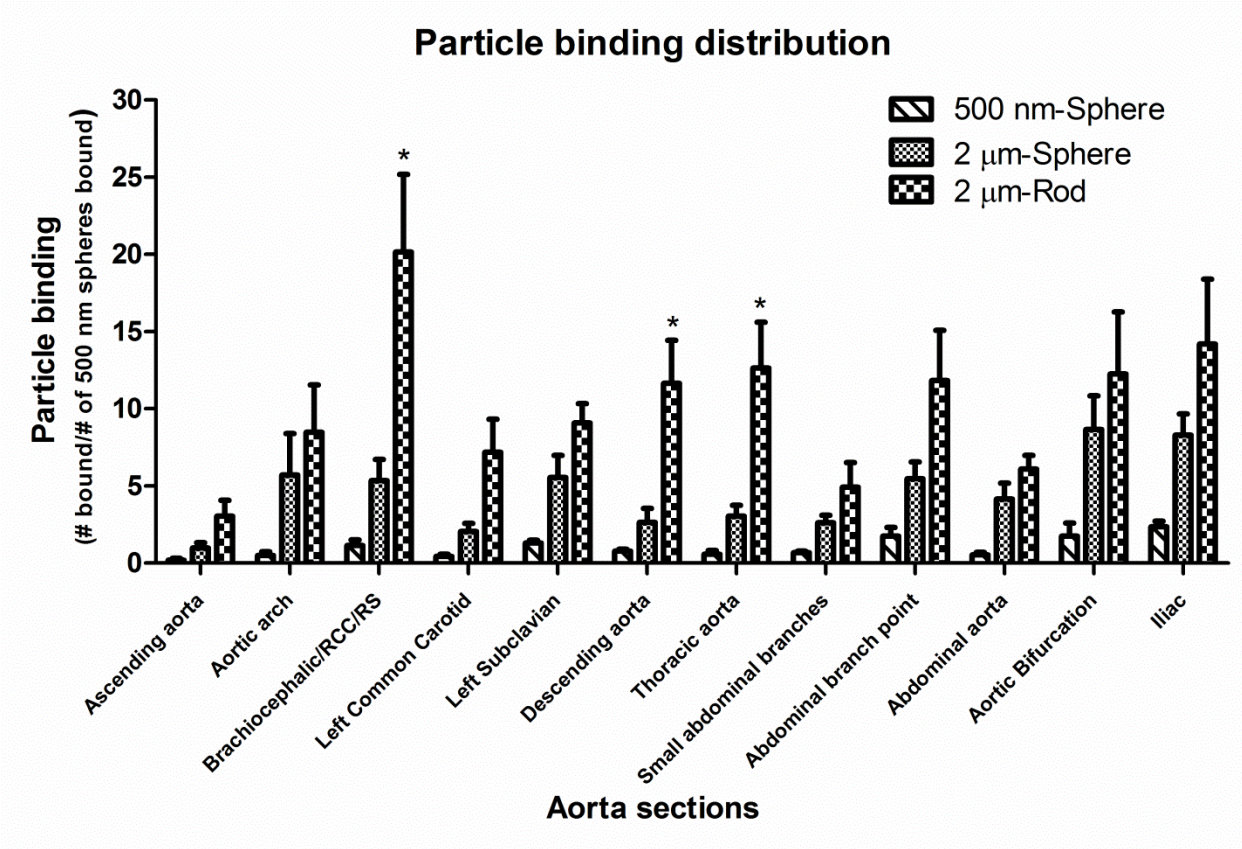

Figure 4.5 Ratio of particle binding of sLe^a and anti-VCAM coated particles to the endothelium in 12 segments along mouse aorta. (* = $p < 0.05$ with respect to 2 μm microspheres, $n \geq 4$). Adhesion data shown is normalized to the averaged to the number of 500 nm diameter spheres bound per segment.

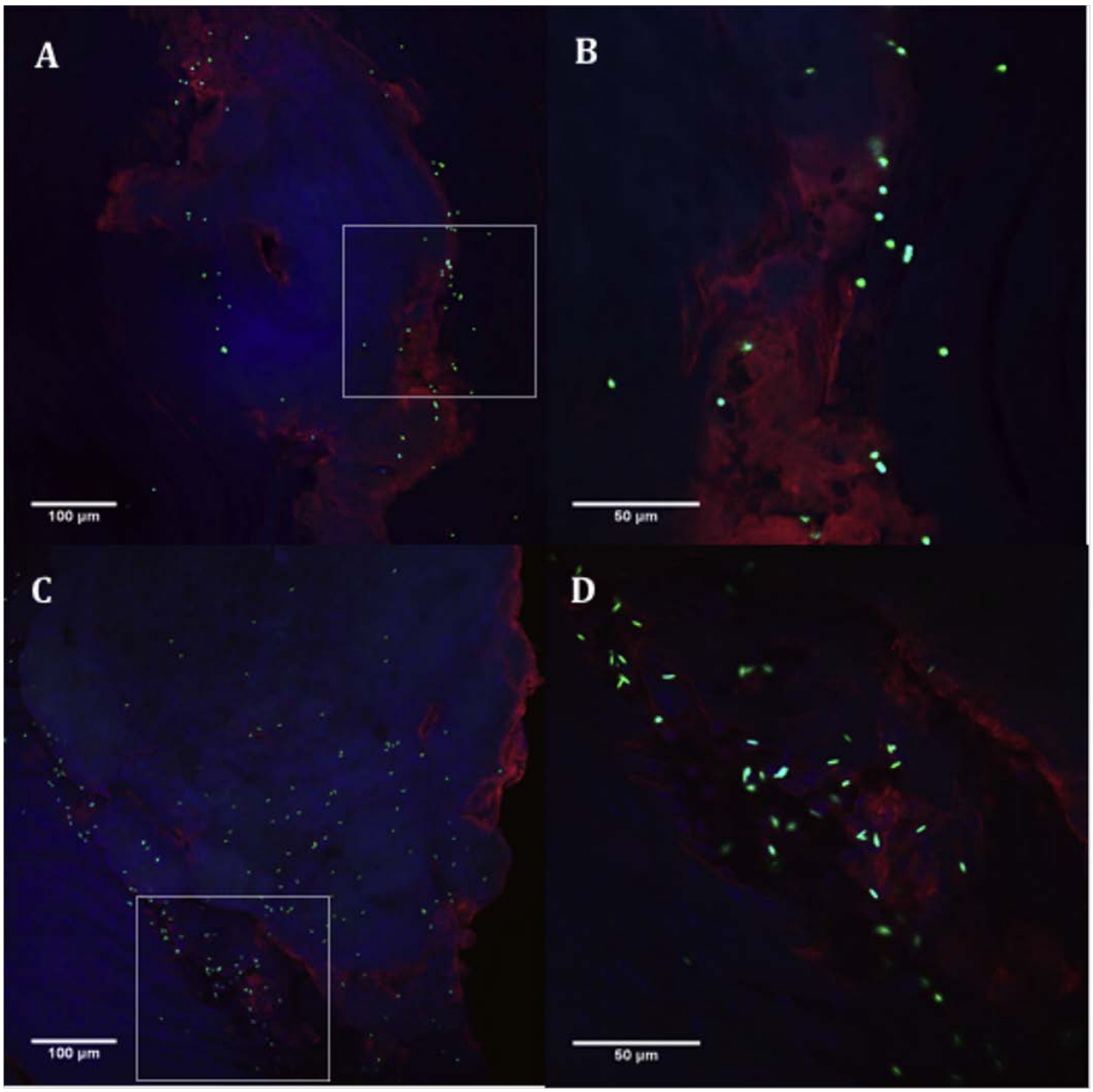

Figure 4.6 Representative images of aortic arch segments (with atherosclerotic plaque present) with adhesion of 2 µm ESD spheres (A and B) and 2 µm ESD rods (C and D) at 20x and 60x magnification, respectively, qualitatively showing the increased adhesion of rods particularly near the periphery of plaques. Blue – nucleus stained by Hoechst, Red – plasma membrane stained by Alexa Fluor conjugate of wheat germ agglutinin and Green – fluorescent particle.

4.2.2 Particle biodistribution to major organs

Major organs were harvested from animals injected with targeted particles to quantify the biodistribution of microrods relative to its equivalent sphere and nanospheres. Figure 4.7 shows the accumulation of targeted particles in the lung, liver, spleen, and kidney. Blood collected following a 30 min circulation time contained negligible amounts of particles. Targeted AR4 microrods were retained at a higher level in the lungs than 2 μm or 500 nm diameter spheres. These same rods were retained at either equal or significantly lower levels than micro/nanospheres in the other organs, potentially because the higher level of first-pass lung accumulation and adhesion to the aorta reduces the amount available to accumulate elsewhere. The 500 nm spheres accumulated at higher levels in the liver than the larger microparticles, and there was no appreciable difference in the splenic accumulation of micro and nanoparticles. Retention of particles in the kidneys was low, as particles larger than about 50-100 nm are not expected to be removed from blood via glomerular filtration.

The higher accumulation of targeted rods in the lungs may be due to physical entrapment of rods (major axis = 5.6 μm) in the small capillaries of the lungs or due to the surface targeting ligands allowing molecular interaction to increase adhesion of particles to the lung endothelium. To investigate this further, uncoated rods and spheres were injected into wild-type mice in the same manner that targeted particles were injected into ApoE-/- mice. As shown in Figure 4.7B, retention of untargeted microspheres and the AR4 microrods in the lungs was about 87% and 93% lower, respectively, than targeted particles of the same size and shape. Retention of untargeted microspheres and microrods was about 605 and 280% higher in the liver and about 81% and 140% higher in the spleen, respectively, than the equivalent targeted particle. When each dataset presented in Figure 4.7 is normalized to the density of each particle type

accumulating in the lungs, the targeted microspheres were found to accumulate in similar amounts in the lung, liver, and spleen while targeted microrods accumulated primarily in the lungs (Figure 4.8). However, untargeted microspheres and microrods both displayed the majority of accumulation in the liver and spleen.

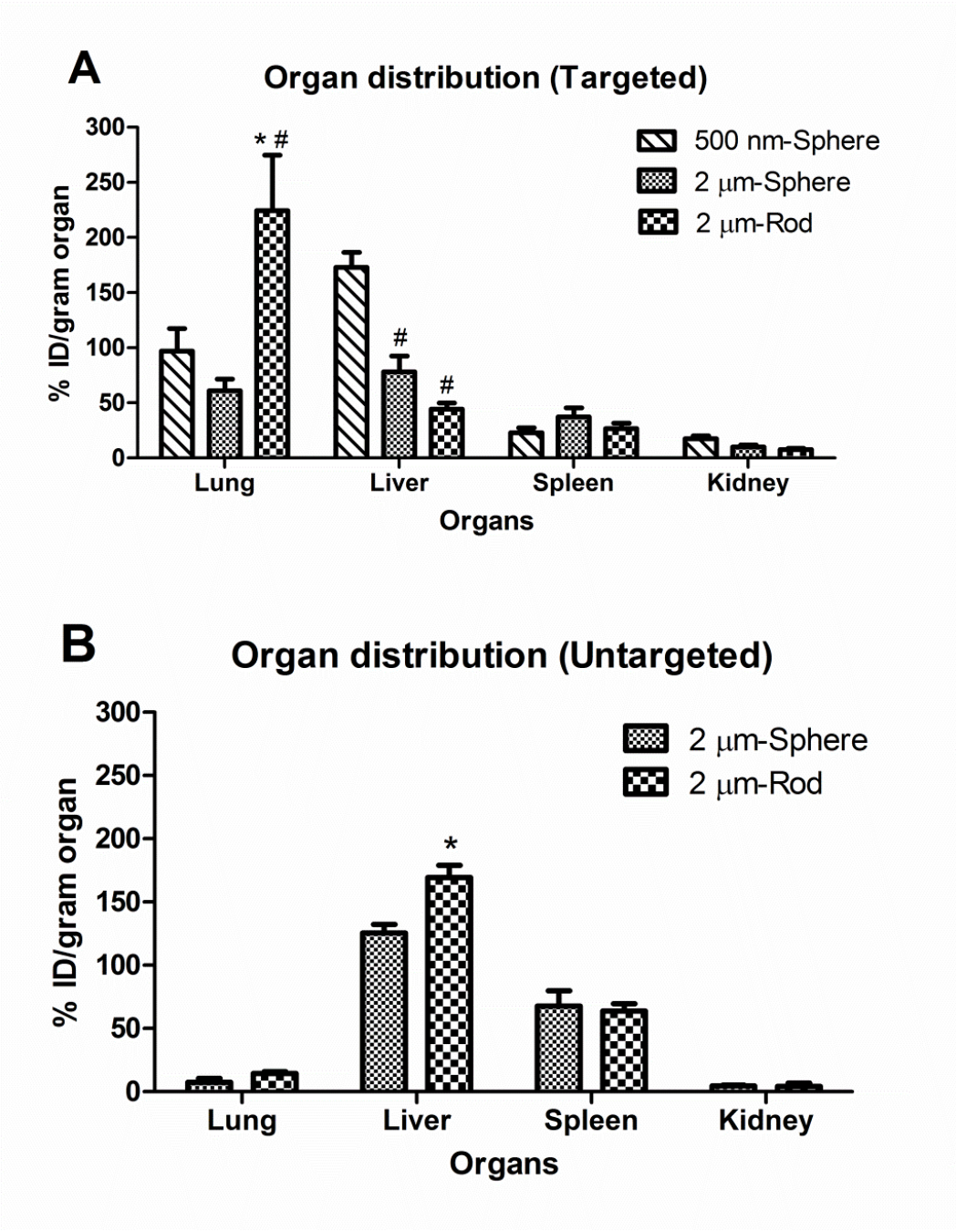

Figure 4.7 (A) Biodistribution of sLe[a] and anti-VCAM coated spheres (500 nm or 2 μm diameters) and rods (2 μm ESD, AR4) in ApoE-/- mice following 30 min circulation via tail-vein injection, $n \geq 5$. (B) Biodistribution of untargeted spheres (2 μm diameter) and (2 μm ESD, AR4) in wild type mice following 30 min circulation via tail-vein injection. (* = $p < 0.05$ relative to 2 μm spheres and # = $p < 0.05$ relative to the 500 nm spheres via one-way ANOVA, $n \geq 4$).

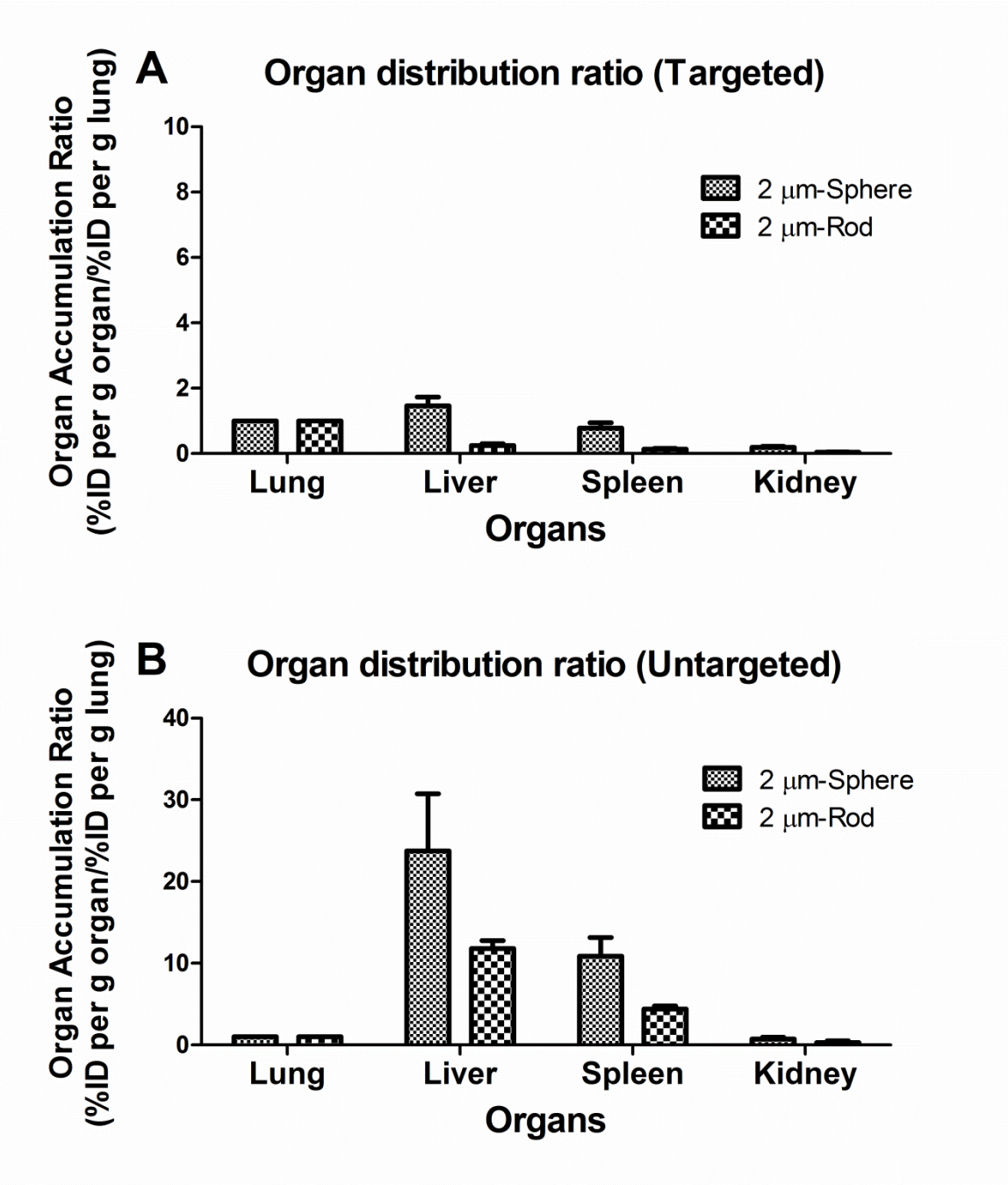

Figure 4.8 Ratio of the accumulation density in major organs (%ID/g organ) to the accumulation density in the lungs (%ID/g lungs) for (A) targeted and (B) untargeted 2 μm spheres and rods (2 μm ESD, AR4) in mice following 30 min circulation via tail-vein injection, $n \geq 4$.

4.3 Discussion

Particle shape is now known to be a parameter that can be tuned to affect the circulation time, biodistribution, adhesion, internalization, and intracellular trafficking of vascular-targeted carrier systems.[23–33] This work demonstrates that the size and shape of vascular-targeted particles plays a role in prescribing their adhesion to sites of atherosclerosis and accumulation in major organs in mice. In order for particles to adhere to inflamed endothelium, they must be able to effectively marginate to the vessel wall – analogous to how circulating immune cells and platelets are able to localize to inflamed/damaged endothelium even in large diameter vessels. Previous works have demonstrated that particle size (spherical diameter) plays a crucial role in the ability or inability of a particle to preferentially marginate in the presence of human blood components (RBC, plasma) using *in vitro* models of flow in blood vessels.[5,6,11,34–36] In general, particles that have diameters (or equivalent spherical diameter) less than about 2 μm do not segregate to the cell-free layer, and hence minimally adhere to inflamed ECs at the wall, in blood flow as efficiently as particles with diameters $\geq$ 2 μm.[6,11,34–36] Instead, evidence suggests these sub-micron to nanoscale particles preferentially remain in the core of flow, encased by RBCs.[6] Concordantly, in this study we find significantly lower adhesion of targeted nanospheres and nanorods of 500 nm ESD along the inflamed mouse aorta compared to microparticles. Also, the enhanced adhesion of microrods to the aorta (roughly 4 fold) compared to equivalent microspheres is in line with our previous observation of particle localization in human blood *in vitro* where microrods ($\geq$ 1 μm ESD) were found to adhere at higher levels than equivalent spheres.[11] This increased adhesion for microrods *in vivo* over their equivalent spheres is likely due to more favorable adhesive characteristics rather than improved localization to the wall, including a higher contact surface area and a streamlined shape to reduce drag in the presence of

blood flow induced shear, since no improvement was found in the localization of rod-shaped particles to the CFL in human blood flow in PPFC assays compared to equivalent spheres.[11] The lack of improved adhesion of nanorods compared to nanospheres is likely due to the inability of nanoparticles to preferentially segregate to the CFL regardless of shape and the diminished impact of higher contact surface area and reduced drag on adhesion for these particles. While particles on the nanometer scale may have benefits in terms of circulation time and ability to transmigrate across the endothelium, this inability of nanoparticles to adhere to the endothelium in the aorta could potentially limit their efficacy as a vascular-targeted carrier system for diseases affecting medium/large blood vessels.

It has been shown that specific areas of the arterial tree are predisposed to atherosclerotic lesion formation, referred to as "atheroprone". These atheroprone areas include the aortic root, the curvature along the aortic arch, and major branching points along the arterial tree; and typically are exposed to disturbed blood flow, characterized by high pulsatility but low net shear.[12,37] We see significantly increased adhesion of microrods compared to spheres in many atheroprone areas, particularly near major branching points in the aorta. Particle adhesion associated with plaques was found preferentially around the periphery of the plaque, which agrees with previously reported findings for the adhesion of VCAM-1 targeted polymeric particles.[38] This patterning is very likely related to the expression patterns of the target molecules,, particularly VCAM-1, which have been shown to persist on ECs adjacent to plaques more so than directly on top of plaques within ApoE-/- mice.[13]

Previous research has also demonstrated that particle shape, size, and the presence of targeting ligands can affect biodistribution in mice.[23,30,33,38,39], and in this study we indeed see the biodistribution profile altered based on these parameters. As expected, we see accumulation of

particles in the lung and liver, with accumulation to a lesser extent in the spleen and kidneys. We find significantly more targeted 2 μm ESD rods in the lungs compared to equivalent spheres, which could be a function of either (1) mechanical entrapment due to the longer axis length of the rod or (2) enhanced molecular interactions of the targeting ligands on rods with pulmonary endothelium. Research has correlated accelerated pulmonary endothelial inflammation with the presence of systemic atherosclerosis,[40] so some level of accumulation based on molecular interaction with targeting ligands could be occurring. Indeed, the significantly lower accumulation of uncoated microparticles in the lung suggests that a significant portion of the lung accumulation is due to molecular interaction of the targeting molecules with the pulmonary endothelium and would be exaggerated for the microrods versus spheres due to the former having a larger surface area for contact (i.e. more favorable adhesion kinetics) and streamlined shape (reduced removal force). Interestingly, the mechanical entrapment of the AR4 microrods (i.e., non-targeted particles) in our study is not significantly different from that of equivalent spheres despite having quite different major axis lengths which would suggest that the rods preferentially enter the capillaries in an orientation that align their major axis in the direction of flow. Overall, our results suggest that the future use of prolate ellipsoids, or other spheroidal-shaped particles, for imaging and drug delivery in atherosclerosis may require the targeting of non-inflammatory molecules specifically overexpressed by the endothelium over plaque but not in the lungs to minimize excessive carrier accumulation and hence prevent signal interference from the lungs in the case of imaging application or unwanted release of cytotoxic/potent agents in the lungs in the case of therapeutic application. Alternatively, rod-shaped microcarriers can be used as a combination therapy where patients are given anti-inflammatory drugs to reduce

inflammation in the lungs prior to injection of rod microcarriers for vascular-targeting in the aorta.

Finally, the overall biodistribution profile of microparticles being shifted towards more accumulation n the liver and spleen when targeting ligands are removed from particle surfaces is likely due to the lower first-pass retention of untargeted particles in the lung (immediately following tail-vein injection) and no retention in the aorta, i.e., more untargeted particles available in circulation for hepatic/splenic clearance compared to targeted particles. The overall observation of particle distribution in this work is in agreement with a previous study by Muro et al., which reported the accumulation of anti-ICAM targeted polystyrene disks in the lungs and liver of C57Bl/6 mice.[23] This study found that targeted disks (0.1 x 1 x 3 μm dimensions) accumulated at high levels in the lungs and relatively low levels in the liver, and that retention of non-targeted (IgG coated) particles was diminished in the lungs, with a corresponding increase in liver accumulation.[23] The liver accumulation of microparticles in our study (%ID/g) is somewhat higher than in other published reports, which may be due to differences in quantification techniques and also heterogeneity in the liver. In this study, the left lobe of the liver from each animal was harvested after the animal is sacrificed and the circulatory system perfused with buffer and fixing agent. It is possible that particles were disproportionately deposited in the left lobe than in the rest of the liver. Indeed, it has been shown that "portal streamlining" can result in incomplete blood mixing causing variation in blood delivered to liver lobes and hence disproportionate deposition of particles between the two lobes.[41] Also, blood from the spleen or stomach tends toward the left side of the liver.[41] Furthermore, others have published *in vivo* studies with fluorescent images that seem to suggest heterogeneous particle deposition in the liver.[42,43]

In conclusion, we confirmed that prolate ellipsoidal microparticles of an intermediate aspect ratio (AR4) with volume equivalent to 2 μm diameter sphere are more efficient than microspheres of equal volume and nanoparticles at targeting inflamed endothelium in the aortae of atherosclerotic mice, particularly in atheroprone areas. Further, these microrods when untargeted displayed a similar level of minimal mechanical entrapment in the lung capillaries compared to their spherical counterparts. Thus, the ellipsoidal geometry at the appropriate magnitude of elongation/aspect ratio may be an advantageous shape to design carriers for targeting the aorta, in order to deliver the highest possible payload of therapeutics or diagnostics intravenously in atherosclerosis. However, targeted microrods, more so than microspheres and nanoparticles, are retained in the lungs at higher levels compared to their untargeted counterparts, likely due to molecular interaction with inflammatory molecules also expressed in the pulmonary vasculature of ApoE-/- mice. Overall in this work we see that particle shape, particle size, and targeting moiety all indeed play a role in prescribing the adhesion and biodistribution profile in a mouse model of atherosclerosis – thus all of these parameters should be considered when designing carrier systems to target this disease.

References

1. Namdee, K. *et al.* In vivo evaluation of vascular-targeted spheroidal microparticles for imaging and drug delivery application in atherosclerosis. *Atherosclerosis* **237,** 279–286 (2014).

2. Lobatto, M. E., Fuster, V., Fayad, Z. A. & Mulder, W. J. M. Perspectives and opportunities for nanomedicine in the management of atherosclerosis. *Nat. Rev. Drug Discov.* **10,** 835–852 (2011).

3. Huang, R. B., Mocherla, S., Heslinga, M. J., Charoenphol, P. & Eniola-Adefeso, O. Dynamic and cellular interactions of nanoparticles in vascular-targeted drug delivery. *Mol Membr Biol* **27,** 312–327 (2010).

4. Decuzzi, P., Pasqualini, R., Arap, W. & Ferrari, M. Intravascular delivery of particulate systems: does geometry really matter? *Pharm Res* **26,** 235–243 (2009).

5. Charoenphol, P. *et al.* Targeting therapeutics to the vascular wall in atherosclerosis--carrier size matters. *Atherosclerosis* **217,** 364–370 (2011).

6. Namdee, K., Thompson, A. J., Charoenphol, P. & Eniola-Adefeso, O. Margination propensity of vascular-targeted spheres from blood flow in a microfluidic model of human microvessels. *Langmuir* **29,** 2530–2535 (2013).

7. Doshi, N. *et al.* Flow and adhesion of drug carriers in blood vessels depend on their shape: A study using model synthetic microvascular networks. *J. Control. Release* **146,** 196–200 (2010).

8. Decuzzi, P. & Ferrari, M. The adhesive strength of non-spherical particles mediated by specific interactions. *Biomaterials* **27,** 5307–5314 (2006).

9. Gavze, E. & Shapiro, M. Motion of inertial spheroidal particles in a shear flow near a solid wall with special application to aerosol transport in microgravity. *J. Fluid Mech.* **371,** 59–79 (1998).

10. Lee, S. Y., Ferrari, M. & Decuzzi, P. Shaping nano-/micro-particles for enhanced vascular interaction in laminar flows. *Nanotechnology* **20,** 495101 (2009).

11. Thompson, A. J., Mastria, E. M. & Eniola-Adefeso, O. The margination propensity of ellipsoidal micro/nanoparticles to the endothelium in human blood flow. *Biomaterials* **34,** 5863–5871 (2013).

12. Ku, D. N., Giddens, D. P., Zarins, C. K. & Glagov, S. Pulsatile flow and atherosclerosis in the human carotid bifurcation. Positive correlation between plaque location and low oscillating shear stress. *Arteriosclerosis* **5,** 293–302 (1985).

13. Iiyama, K. *et al.* Patterns of vascular cell adhesion molecule-1 and intercellular adhesion molecule-1 expression in rabbit and mouse atherosclerotic lesions and at sites predisposed to lesion formation. *Circ Res* **85,** 199–207 (1999).

14. Galkina, E. & Ley, K. Vascular adhesion molecules in atherosclerosis. *Arterioscler. Thromb. Vasc. Biol.* **27,** 2292–2301 (2007).

15. Davies, M. J. *et al.* The expression of the adhesion molecules ICAM-1, VCAM-1, PECAM, and E-selectin in human atherosclerosis. *J. Pathol.* **171,** 223–229 (1993).

16. McAteer, M. A. *et al.* Magnetic resonance imaging of endothelial adhesion molecules in mouse atherosclerosis using dual-targeted microparticles of iron oxide. *Arterioscler. Thromb. Vasc. Biol.* **28,** 77–83 (2008).

17. Ferrante, E. A., Pickard, J. E., Rychak, J., Klibanov, A. & Ley, K. Dual targeting improves microbubble contrast agent adhesion to VCAM-1 and P-selectin under flow. *J. Control. Release* **140,** 100–107 (2009).

18. Ho, C. C., Keller, A., Odell, J. A. & Ottewill, R. H. Preparation of monodisperse ellipsoidal polystyrene particles. *Colloid Polym. Sci.* **271,** 469–479 (1993).

19. Champion, J. A., Katare, Y. K. & Mitragotri, S. Making polymeric micro- and nanoparticles of complex shapes. *Proc Natl Acad Sci U S A* **104,** 11901–11904 (2007).

20. Glagov, S., Zarins, C., Giddens, D. P. & Ku, D. N. Hemodynamics and atherosclerosis. Insights and perspectives gained from studies of human arteries. *Arch. Pathol. Lab. Med.* **112,** 1018–1031 (1988).

21. Kjaernes, M., Svindland, A., Walløe, L. & Wille, S. O. Localization of early atherosclerotic lesions in an arterial bifurcation in humans. *Acta Pathol. Microbiol. Scand. A.* **89,** 35–40 (1981).

22. Grøttum, P., Svindland, A. & Walløe, L. Localization of atherosclerotic lesions in the bifurcation of the main left coronary artery. *Atherosclerosis* **47,** 55–62 (1983).

23. Muro, S. *et al.* Control of endothelial targeting and intracellular delivery of therapeutic enzymes by modulating the size and shape of ICAM-1-targeted carriers. *Mol. Ther.* **16,** 1450–1458 (2008).

24. Geng, Y. *et al.* Shape effects of filaments versus spherical particles in flow and drug delivery. *Nat Nanotechnol* **2,** 249–255 (2007).

25. Christian, D. A. *et al.* Flexible filaments for in vivo imaging and delivery: persistent circulation of filomicelles opens the dosage window for sustained tumor shrinkage. *Mol Pharm* **6,** 1343–1352 (2009).

26. Champion, J. A. & Mitragotri, S. Role of target geometry in phagocytosis. *Proc Natl Acad Sci U S A* **103,** 4930–4934 (2006).

27. Champion, J. A. & Mitragotri, S. Shape induced inhibition of phagocytosis of polymer particles. *Pharm Res* **26,** 244–249 (2009).

28. Gratton, S. E. *et al.* The effect of particle design on cellular internalization pathways. *Proc Natl Acad Sci U S A* **105,** 11613–11618 (2008).

29. Agarwal, R. *et al.* Mammalian cells preferentially internalize hydrogel nanodiscs over nanorods and use shape-specific uptake mechanisms. *Proc Natl Acad Sci U S A* **110,** 17247–17252 (2013).

30. Decuzzi, P. *et al.* Size and shape effects in the biodistribution of intravascularly injected particles. *J Control Release* **141,** 320–327 (2010).

31. Huang, X. *et al.* The shape effect of mesoporous silica nanoparticles on biodistribution, clearance, and biocompatibility in vivo. *ACS Nano* **5,** 5390–5399 (2011).

32. Devarajan, P. V *et al.* Particle shape: a new design parameter for passive targeting in splenotropic drug delivery. *J Pharm Sci* **99,** 2576–2581 (2010).

33. Kolhar, P. *et al.* Using shape effects to target antibody-coated nanoparticles to lung and brain endothelium. *Proc Natl Acad Sci U S A* **110,** 10753–10758 (2013).

34. Charoenphol, P., Huang, R. B. & Eniola-Adefeso, O. Potential role of size and hemodynamics in the efficacy of vascular-targeted spherical drug carriers. *Biomaterials* **31,** 1392–1402 (2010).

35. Tilles, A. W. & Eckstein, E. C. The near-wall excess of platelet-sized particles in blood flow: its dependence on hematocrit and wall shear rate. *Microvasc. Res.* **33,** 211–223 (1987).

36. Eckstein, E. C., Tilles, A. W. & Millero 3rd, F. J. Conditions for the occurrence of large near-wall excesses of small particles during blood flow. *Microvasc Res* **36,** 31–39 (1988).

37. Nakashima, Y., Plump, A. S., Raines, E. W., Breslow, J. L. & Ross, R. ApoE-deficient mice develop lesions of all phases of atherosclerosis throughout the arterial tree. *Arter. Thromb* **14,** 133–140 (1994).

38. Deosarkar, S. P. *et al.* Polymeric particles conjugated with a ligand to VCAM-1 exhibit selective, avid, and focal adhesion to sites of atherosclerosis. *Biotechnol Bioeng* **101,** 400–407 (2008).

39. Gratton, S. E. *et al.* Nanofabricated particles for engineered drug therapies: a preliminary biodistribution study of PRINT nanoparticles. *J Control Release* **121,** 10–18 (2007).

40. Moore, G. W., Smith, R. R. & Hutchins, G. M. Pulmonary artery atherosclerosis: correlation with systemic atherosclerosis and hypertensive pulmonary vascular disease. *Arch Pathol Lab Med* **106,** 378–380 (1982).

41. Malarkey, D. E., Johnson, K., Ryan, L., Boorman, G. & Maronpot, R. R. New insights into functional aspects of liver morphology. *Toxicol. Pathol.* **33,** 27–34 (2005).

42. Ballou, B., Lagerholm, B. C., Ernst, L. A., Bruchez, M. P. & Waggoner, A. S. Noninvasive Imaging of Quantum Dots in Mice. *Bioconjug. Chem.* **15,** 79–86 (2004).

43. Michalet, X. *et al*. Quantum dots for live cells, in vivo imaging, and diagnostics. *Science* **307,** 538–544 (2005).

CHAPTER 5: EFFECT OF PARTICLE DENSITY ON ADHESION OF VASCULAR-TARGETED CARRIERS IN VITRO

ABSTRACT

For vascular-targeted carrier (VTC) systems to be effective, carriers must be able to localize and adhere to the target site from blood flow. It has been shown that neutrally-buoyant nanoparticles are limited by their ability to localize to the endothelium, making them sub-optimal as carriers despite their many benefits including better evasion of the immune system and ease in navigating capillary beds. Here we show that particle density is a parameter which can be exploited to improve the localization and adhesion of nanospheres, potentially making them more effective at accessing diseased tissues locally and specifically via the vasculature. Using a parallel plate flow chamber assay method we see that silica (Si) spheres, which have a density roughly twice that of blood, consistently exhibits improved adhesion to inflamed endothelium compared to neutrally-buoyant polystyrene (PS) spheres with 500 nm diameters. We see directly that Si spheres display improved near-wall localization when in the presence of RBCs compared to in pure buffer, likely resulting in the observed improvement in adhesion. We find titania (Ti) spheres (4 times more dense than blood) adhere at levels higher than PS, but only in conditions where gravity or centrifugal force acts in the direction of adhesion; displaying the importance of other hemodynamic conditions such as channel orientation and shear rate in determining carrier targeting effectiveness. Overall, we find that in the light of the wide array of materials proposed

for use as carrier systems for drug delivery and diagnostics, particle density may be a useful tool for improving the targeting of diseased tissues.

5.1 Introduction

The ability of vascular-targeted carriers to marginate, or localize and adhere to the periphery of the blood vessel, is an important requisite for successful targeting (i.e., binding) to the endothelium. It has been established that particle size and geometry prescribes the ability of a particle to marginate in human blood flow.[1–9] However, it is quite possible that other particle characteristics, in addition to size, may affect the margination propensity of a carrier system. One such parameter is particle density, which can be altered depending on the material makeup of the carrier system being employed. To date, materials with a range of densities have been proposed for use in vascular-targeted drug delivery or diagnostics, including microbubbles[10–12], polymers[13–16], liposomes[17,18], inorganic particles (titania, gold, iron oxide)[19–21], blood cells[22,23], or combinations of multiple material types[24–26]. Yet, there is limited understanding of the role that density plays in prescribing carrier performance relating to their margination and vascular wall adhesion.

Particle density forces seemingly could be regarded as negligible in describing particle motion relevant to physiological blood flow, since the hydrodynamic forces due to flow (for microparticles) and Brownian forces (for nanoparticles) are often orders of magnitude higher than density-dependent forces such as gravitational and centrifugal forces.[27,28] However, the distance that a particle must travel in the normal direction to the endothelium to initiate contact may also be orders of magnitude shorter than the distance the particle travels in the transverse direction. This is particularly true for particles already localized to the cell-free layer (CFL) which forms adjacent to the endothelium and has a height of only a few microns.[29]

It is widely known that red blood cells (RBC) play a crucial role in the margination of leukocytes and platelets.[29,30] By congregating in the center of flow, RBCs force white cells and

platelets to concentrate in the CFL, aiding in their margination and interaction with the vascular wall. This effect is in part due to the size of platelets (2-3 μm diameter) and white cells (8-12 μm diameter).[31] It has been shown via *in vitro* models of human vasculature that neutrally-buoyant microspheres of sufficient size (≥2 μm diameter) can also take advantage of this phenomenon.[1–7] However, it has been shown experimentally and confirmed computationally that neutrally-buoyant particles with diameters in the 100-500 nm size range are not preferentially distributed via this RBC effect, resulting in inefficient margination and sub-optimal targeting to endothelium in microchannels in the presence of physiological levels of RBCs.[3,5,7,8] Still, particles in this size range are attractive and are typically proposed for vascular-targeted drug delivery in that they are able to carry a larger payload than ultra-small nanoparticles while still being able to safely navigate microvasculature.[32–39] To date, it is unclear whether particle density affects the margination of larger nanoparticles or sub-micron sized particles to the CFL via interactions with RBCs in blood flow. While a recent study shows that increasing particle density negatively affects nanoparticle margination in a microchannel[40], this was done in the absence of blood components and with nanoparticles having 60-65 nm diameters whose density effects are much smaller compared to sub-micron sized particles.

Evidence exists in the literature that density may have a role on how efficiently platelets interact with the endothelium in blood flow. Even in the small density range reported for sub-populations of platelets (1.040-1.080 g/mL), it was found that the most dense platelets exhibited roughly 4 times higher initial adhesion than the least dense platelets.[41] Materials proposed for vascular-targeting have a much wider range of particle densities, including bubbles (less dense than blood), neutrally-buoyant and non-neutrally buoyant polymers or lipid based particles, or more dense metal-based particles.[42] Therefore, it is of interest to investigate how the interaction

between nanoparticles with red blood cells (RBC) affects margination when particle density is considered.

In this study, we investigate how the density-dependent forces (gravity, centrifugal), density-independent forces (hydrodynamic, Brownian), momentum, and adhesion dynamics combined with the presence of blood components prescribes the targeting of 500 nm diameter nanospheres to inflamed endothelium from human blood flow. Further, we investigate how the gravity effects change the adhesion profile of targeted spheres when the chamber is oriented such that the direction of margination is either toward or away from gravity. Using a recirculation flow setup we determine whether centrifugal force due to an induced recirculation eddy in the flow allows particles with higher densities to better target the endothelium compared to neutrally-buoyant particles. Finally, we investigate how these *in vitro* results translate to the more complex *in vivo* environment using an inflamed mouse model.

5.2 Results

In this work, we employ an *in vitro* human blood flow assay to study the targeting ability of polystyrene (PS), silica (Si), and titania (Ti) spheres which have 500 nm diameter and densities of 1.05, 2.0, and 3.9 g/cm^3, respectively, to the vascular wall in various blood flow conditions. Briefly, particles are surface-coated with targeting ligands, mixed with buffer or a RBC-in-buffer mixture, and flowed through a parallel plate flow chamber (PPFC), which is lined with an inflamed monolayer of human umbilical vein endothelial cells (HUVEC). Parameters such as shear rate, blood flow profile, chamber orientation and microchannel height are altered to determine how particle density causes differences in targeting affinity. This *in vitro* model of blood flow in a vessel is a useful tool to predict the *in vivo* targeting ability of a carrier system to a multitude of diseased states, depending on the ligand-receptor system employed. In this work,

we target acute inflammation that is relevant to many inflammatory diseases, including atherosclerosis and arthritis.

5.2.1 Effect of RBCs on Particle Adhesion in Laminar Flow

Figure 5.1 compares the adhesion density of 500 nm diameter, vascular-targeted polystyrene (PS), silica (Si), and titania (Ti) spheres following 5 min of either buffer flow or RBC-in-buffer flow over an inflamed HUVEC monolayer at a physiological shear rate of 500 s^{-1}. Representative images of particles bound on HUVEC are shown in Figure 5.2. In buffer flow (Figure 5.1A), particle adhesion to HUVEC at the bottom of the chamber increases with particle density, as Si and Ti spheres adhered 360% and 640% higher, respectively, than PS spheres (though the difference for Si and PS was not statistically significant).

Multiple interesting observations can be made when a physiologically relevant number of RBCs are added to the experimental setup (Figure 5.1B). When the HUVEC monolayer is at the bottom of the chamber, the adhesion of Si and Ti spheres is 257% and 91% higher, respectively, than that of PS spheres. When the chamber is inverted and binding is occurring against the direction of gravity, the adhesion of Si spheres is still 236% higher than that of PS spheres, while the adhesion of PS and Ti spheres was not significantly different. Even with gravity force acting opposite the adhesive surface, Si particles still bind more than neutrally-buoyant PS. This suggests that Si spheres are potentially localizing to the wall, i.e. CFL, better than PS or Ti in the presence of RBC, particularly given that the average adhesion in upright buffer flow assays (Figure 5.1A) increased with increasing particle density.

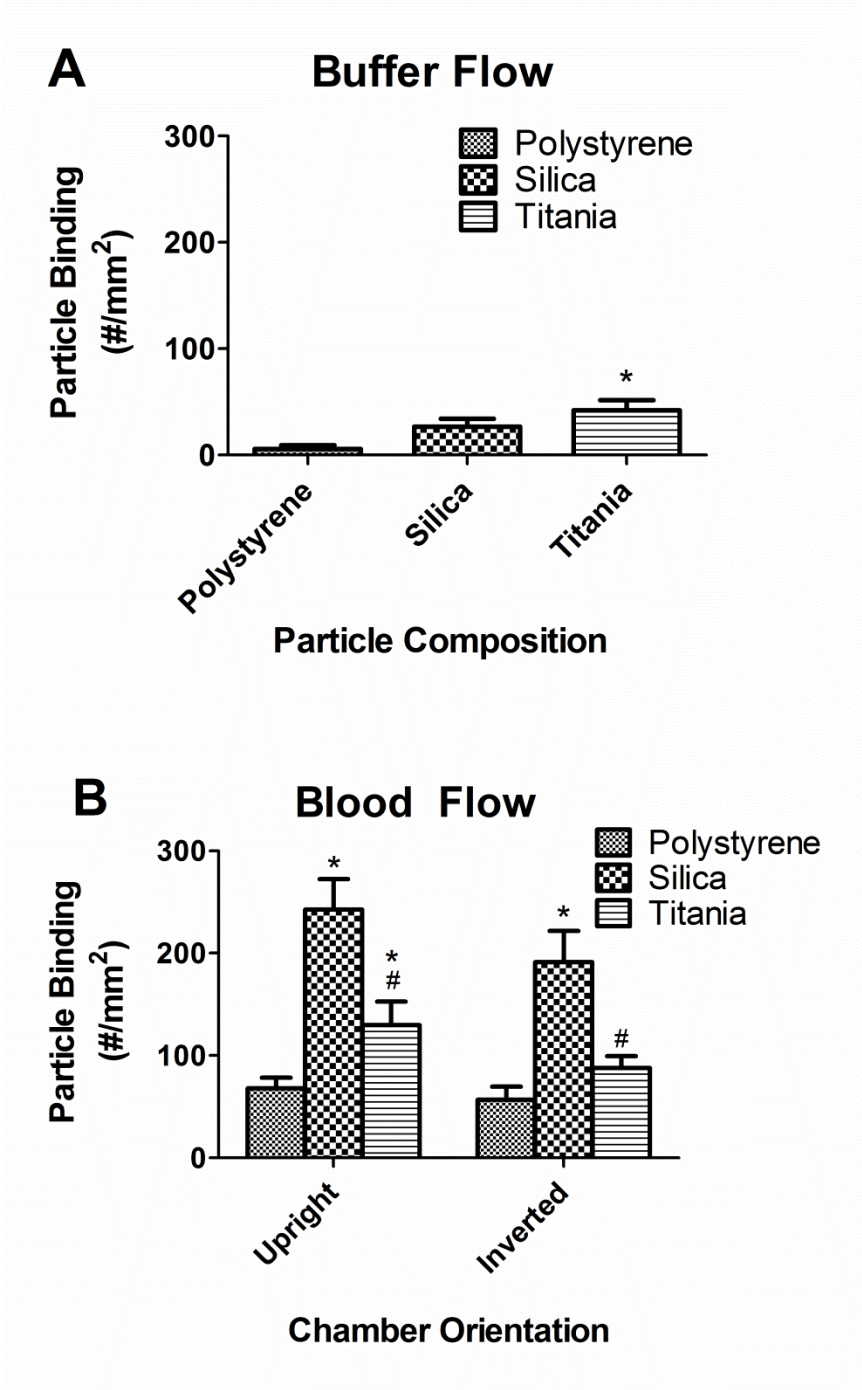

Figure 5.1 Adhesion of sLe^a-coated PS, Si, and Ti spheres (500 nm diameter) to inflamed endothelium after 5 mins of particle-loaded ($5x10^5$ particles/mL total volume) buffer flow (A) or RBC-in-buffer flow (B) at a shear rate of 500 s^{-1}. Experiments were done with the endothelial layer at the bottom (upright) of the chamber in the buffer flow experiments, and chamber orientation was varied in the RBC-in-buffer flow experiments. Student t-test were performed comparing particle adhesion to adhesion of *PS or $^{\#}$Si at the same chamber orientation. A p value < 0.05 was considered statistically significant.

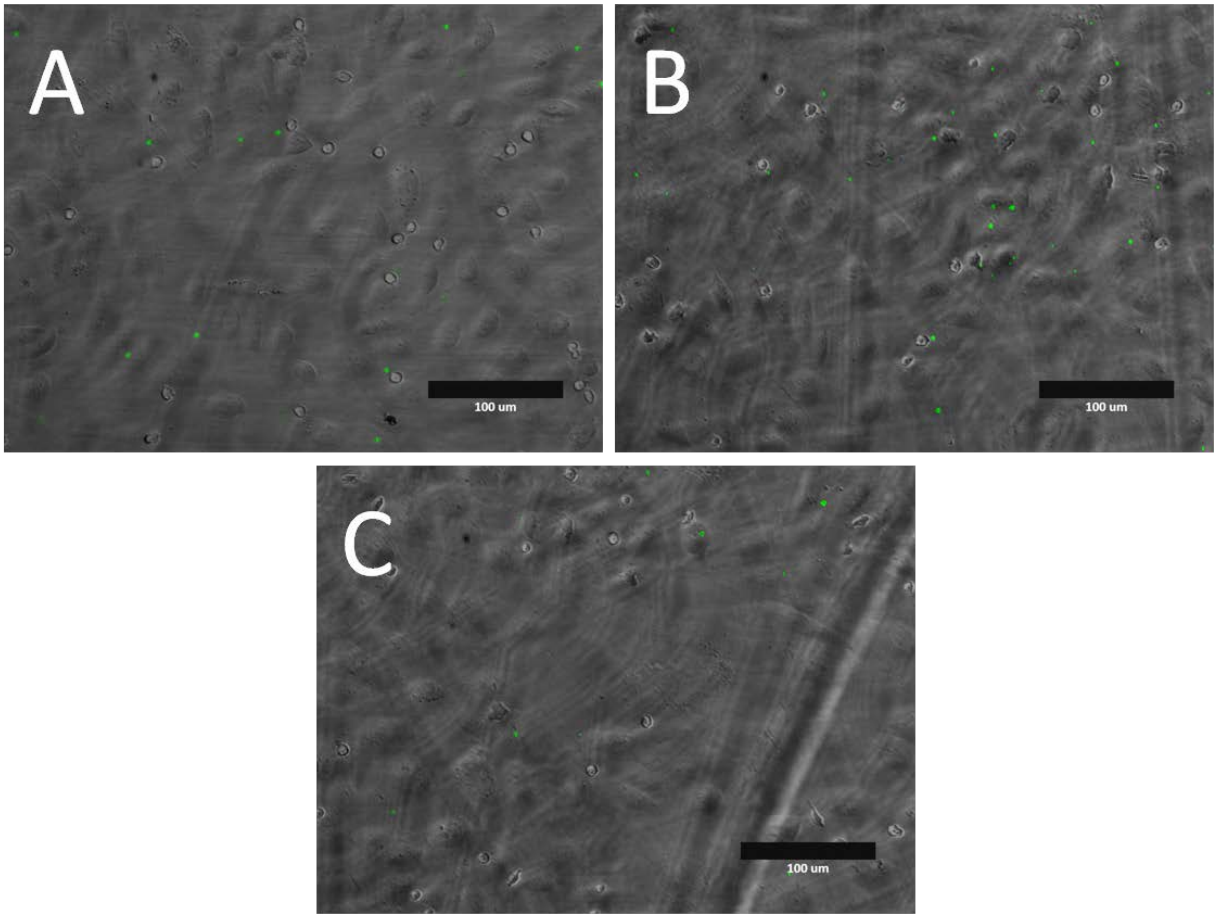

Figure 5.2 Sample images of sLe^a-coated (A) PS, (B) Si, and (C) Ti spheres (500 nm diameter) adhering to inflamed endothelium after 5 minutes of steady laminar particle-loaded ($5x10^5$ particles/mL total volume) RBC-in-buffer flow at a shear rate of 500 s^{-1}. The chamber had a height of 254 μm and the orientation was upright. Scale bar = 100 μm.

5.2.2 Localization of Particles to the Red Blood Cell-Free Layer

In light of the observations seen in Figure 5.1, it is important to consider what mechanisms may cause the density-dependent differences in adhesion in the presence of RBCs. One possible behavior which could result in improved adhesion to the endothelium would be the improved localization of particles to the CFL, resulting in a higher number of particles with an opportunity to bind. In order to investigate this, we utilize a previously described microchannel setup in which fluorescent particles localized to a near-wall focal plane are imaged using a confocal microscope.[5,7] This setup decouples particle localization from the ligand/receptor adhesion to determine how the presence of RBCs affects only localization to the near-wall region. As an upright confocal microscope was used, particles localized near the upper wall of the flow chamber are imaged.

Figure 5.3A shows the near-wall (within 2 μm distance from top wall) localization of PS, Si, and Ti particles from RBC-in-buffer flow in a microchannel under the same conditions as the adhesion experiment represented by Figure 5.1B (inverted). On average, the Si particles localized the highest, followed by PS and then Ti particles (differences were not significant). Then, it is of interest to compare the particle localization in RBCs-in buffer flow to the near-wall localization in the absence of RBCs (Figure 5.3B). Interestingly, the addition of RBCs results in a 13% increase in the amount of Si spheres localized to the near-wall region compared to particles in buffer flow, while adding RBCs results in a 12% and 4% *decrease* in the amount of near-wall localized PS and Ti spheres relative to buffer flow.

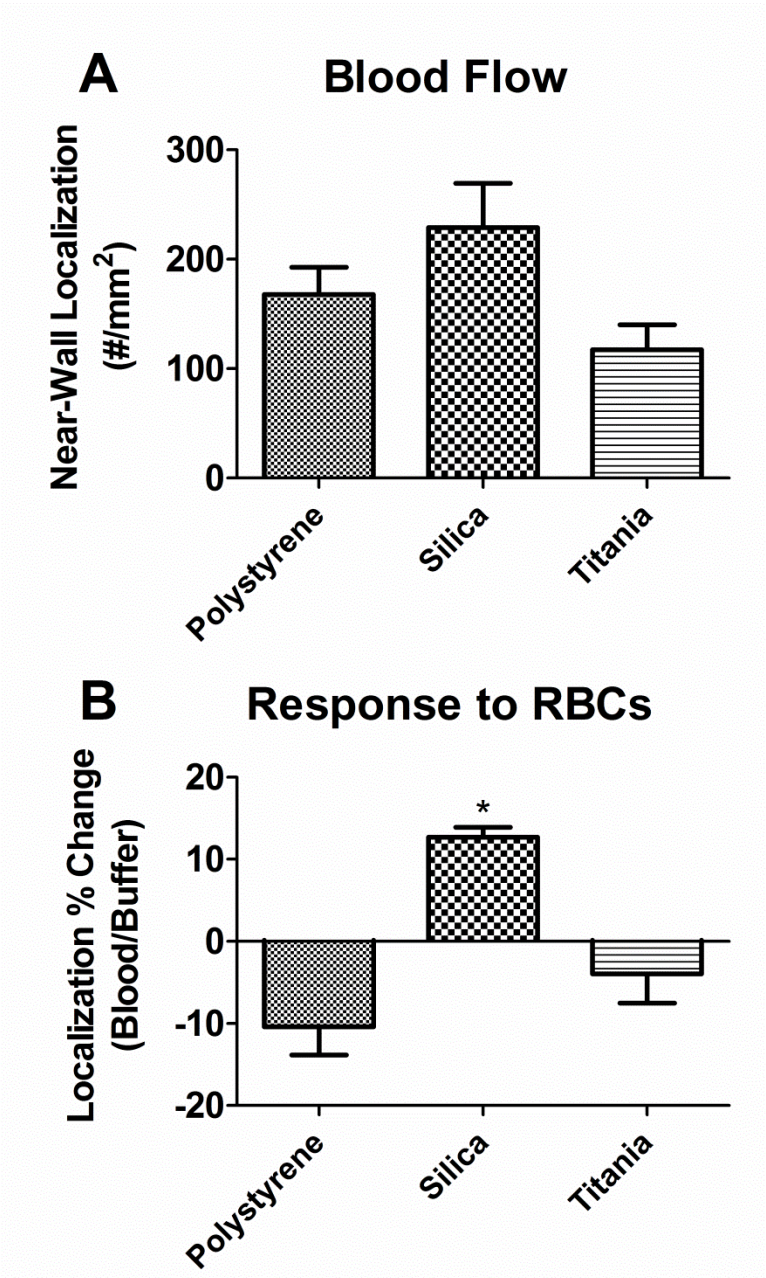

Figure 5.3 (A) Localization of PS, Si, and Ti spheres (500 nm diameter) to within 2 μm of the upper wall of a microchannel from particle-loaded RBC-in-buffer flow ($5x10^5$ particles/mL total volume) at 500 s^{-1}, and (B) percent change in the particle localization between particle-loaded buffer flow and particle-loaded RBC-in-buffer flow under the same conditions. Student t-test was performed comparing *particle localization and localization % change to that of PS. A p-value < 0.05 was considered statistically significant.

5.2.3 Effect of Shear Rate on Adhesion of Dense Particles

Based on the results shown in Figure 5.1 and Figure 5.3, we see evidence that Si spheres have higher adhesion from RBC-in-buffer flow than Ti spheres because Si are more effective at localizing to the CFL in the presence of RBCs. Another factor which must be considered in the adhesion experiment once particles are in the CFL is the binding kinetics between the targeting ligands on the particle and the targeted receptors, countered by the fact that these particles carry translational momentum that the ligand/receptor interaction must overcome to result in firm adhesion. At a given shear rate and ligand surface coverage, a Ti particle would need to overcome a higher force than a Si particle to firmly adhere. Figure 5.4A shows the adhesion level of Si and Ti spheres to inflamed endothelium at a range of laminar shear rates (from 50-1000 s^{-1}) for a fixed experiment time of 5 min. Also, data is normalized to the number of particles used per experiment (Figure 5.4B), so that the "adhesion efficiency" of particles at different shear rates can be properly compared. At the lowest shear rates investigated (50, 100 s^{-1}), Si and Ti display the same adhesion and thus, adhesion efficiency. At increasing shear rates of 200 and 500 s^{-1}, the adhesion of Si spheres increases to a maximum at 500 s^{-1}; followed by a significant decrease in adhesion at 1000 s^{-1}. At shear rates above 100 s^{-1}, the Ti particles do not show a similar increase in adhesion as was seen for Si particles; and likewise, the adhesion efficiency decreases more than Si particles especially at 200 and 500 s^{-1}. At 1000 s^{-1}, the adhesion efficiency of Si spheres decreases to a level not significantly different from that of Ti spheres. Also, we can compare adhesion efficiency between particles at conditions when the momentum should be the approximately equal between Si and Ti spheres (Si at 100 s^{-1} versus Ti at 50 s^{-1}, for instance). At low shear, we do see that the heavier Ti spheres have better adhesion efficiency to the bottom of the chamber than Si spheres when the momentum is fixed.

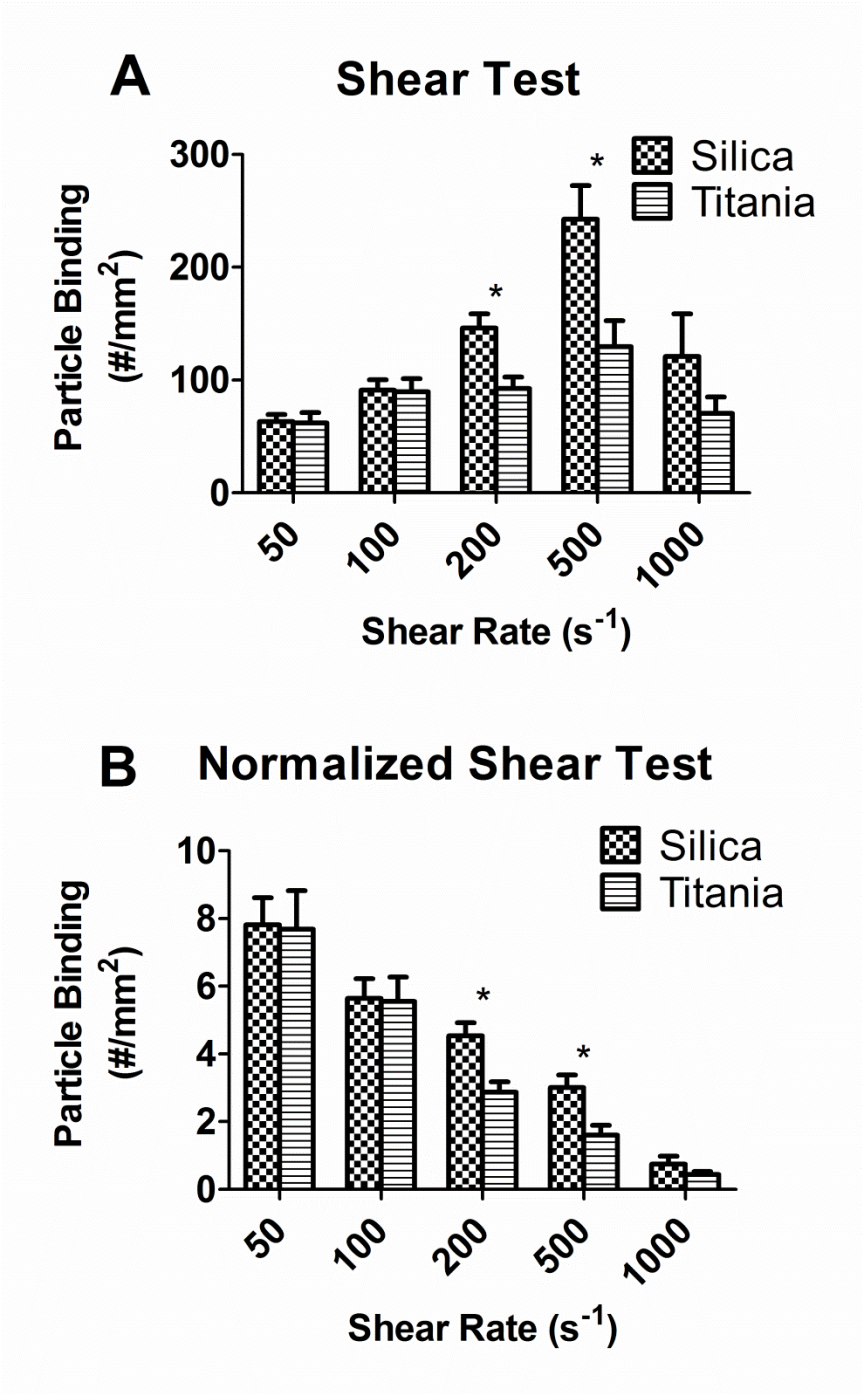

Figure 5.4 Adhesion of sLe^a-coated Si and Ti spheres (500 nm ESD) to inflamed endothelium after 5 minutes of particle-loaded RBC flow ($5x10^5$ particles/mL blood) at various shear rates. Experiments were done with the endothelial monolayer at the bottom of the chamber. Student t-tests were performed comparing *Si and Ti adhesion at a given shear rate. A p-value < 0.05 was considered statistically significant.

5.2.4 Recirculation Flow: Effect of Induced Eddy on Adhesion

Some chronic inflammatory diseases including atherosclerosis are known to form in areas of the vasculature characterized by disturbed flow profiles (recirculating eddy flow or oscillating pulsatility) caused by curvature or bifurcations in the vessel.[43,44] The presence of a permanent recirculating eddy in the flow introduces density-dependent centrifugal force, which may alter the adhesion profile in these areas. We investigate this type of disturbed blood flow pattern using a modified PPFC setup, in which a vertical step in the channel causes a recirculation eddy to form immediately downstream of the step.[45] Further down from the step is the a reattachment point (a point of flow separation) where a portion of the flow streamline moves downstream toward steady laminar flow, and a far downstream region is defined where the flow is redeveloped into a steady laminar profile. We then can observe the particle adhesion profile to a layer of inflamed endothelium adjacent to this recirculation eddy, as well as in the far downstream region.

Figure 5.5 shows the adhesion of targeted PS, Si, and Ti spheres to activated HUVEC from blood flow with an imposed recirculation eddy. At this shear rate (200 s^{-1}, as calculated from the expanded section of the chamber), the recirculation eddy is roughly 225 μm from the step to the stagnation point (the point at which flow separates). It is apparent, particularly for Si and Ti particles, that adhesion then is a function of distance downstream of the step. Adhesion within the recirculation region is increased for Si and Ti particles compared to PS, whether the chamber is in the upright or inverted orientation. The adhesion for Si and Ti spheres is also higher than for PS spheres in the far downstream region when the chamber is upright (gravity acting in the direction of the HUVEC layer), but there is no significant difference between particle types far downstream when the chamber is inverted. Also, the adhesion of Si and Ti in

the recirculating flow pattern and further downstream is not significantly different, suggesting that the two particles are redistributed to the wall area about the same.

It should be noted that the adhesion in the recirculation channel is not compared directly to the laminar flow experiments in Figure 5.1 because those experiments are done at a higher shear rate and in a channel with a smaller height. A separate set of laminar flow assays were done at the same shear rate and channel height (200 s^{-1}, 508 μm) as the recirculation flow assay, in order to elucidate the effect of the recirculation eddy on adhesion in the far downstream region of the channel (Figure 5.6). In the recirculation region and in the far downstream region in an upright channel, adhesion for Si and Ti spheres is roughly twice that of the adhesion in steady laminar flow in a straight channel, while PS spheres is about the same regardless of flow type. When the chamber is inverted, there is no difference in particle adhesion from laminar flow with upstream recirculation and laminar flow in a straight channel.

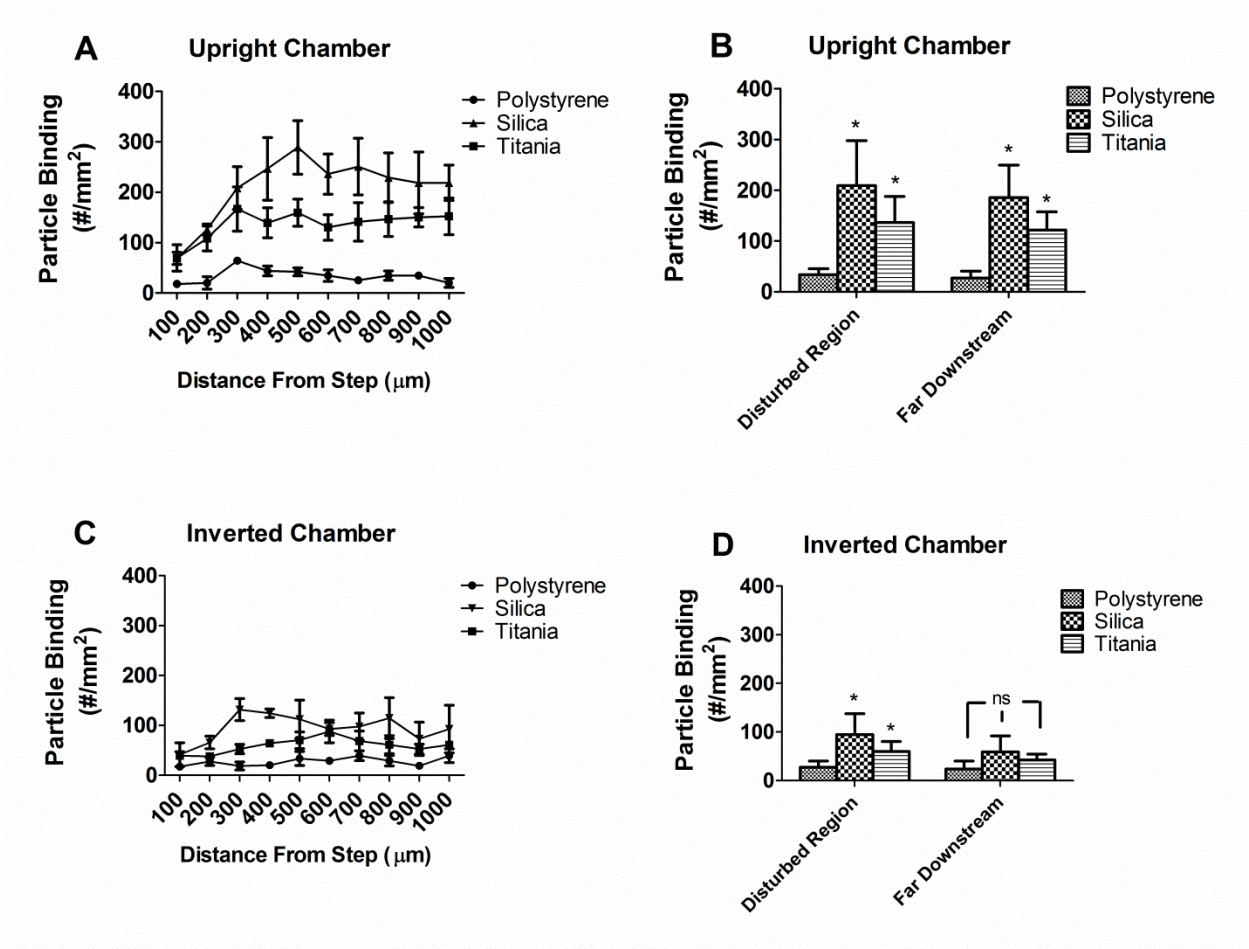

Figure 5.5 Adhesion of sLe^a-coated PS, Si, and Ti spheres (500 nm ESD) to inflamed endothelium after 5 mins of particle-loaded RBC flow ($5x10^5$ particles/mL blood) at 200 s^{-1}. Experiments were done in a recirculation flow PPFC setup with the endothelial monolayer at the bottom (A,B) or top (C,D) of the chamber. Student t-test were performed comparing particle adhesion to *PS and $^{\#}$Si at the same chamber orientation. A p-value < 0.05 was considered statistically significant.

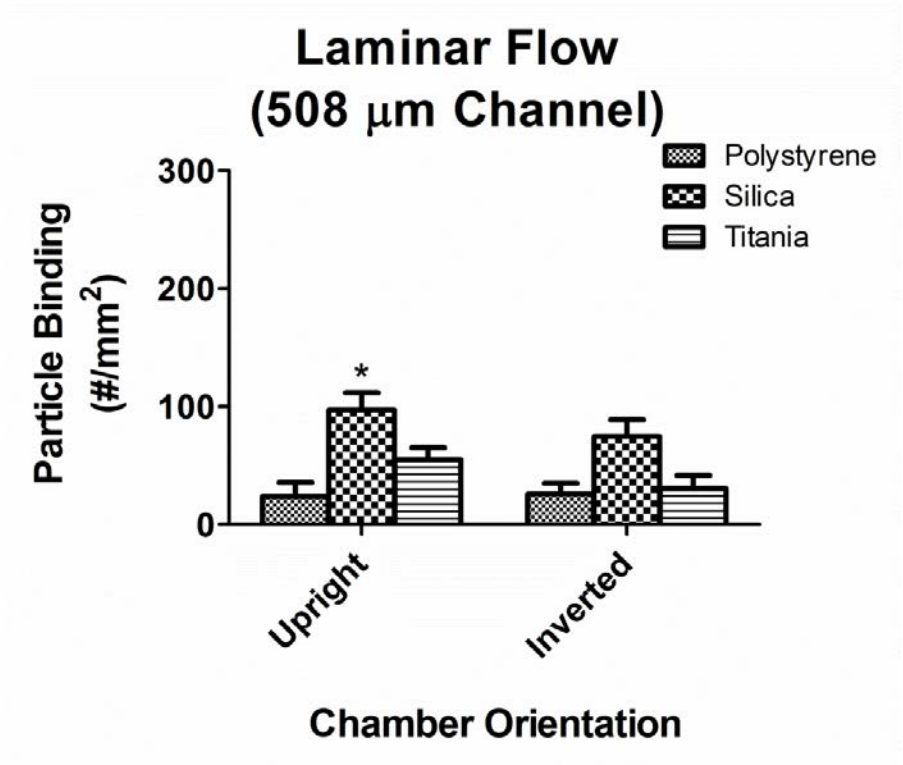

Figure 5.6 Adhesion of sLe^a-coated PS, Si, and Ti spheres (500 nm diameter) to inflamed endothelium after 5 min of steady laminar particle-loaded ($5x10^5$ particles/mL total volume) RBC-in-buffer flow at a shear rate of 200 s^{-1}. The chamber had a height of 508 μm and the orientation was varied.

Since the improved adhesion in recirculation flow diminishes in an inverted channel, it may be that the negative gravity component overrides the benefit of the recirculation eddy. Then, it is of interest to examine whether the adhesion in the inverted channel will improve if the magnitude of the centrifugal force is increased. To test this we examined the adhesion of PS, Si, and Ti particles from recirculation blood flow at a higher shear rate of 625 s^{-1}. Indeed, we find that at this higher shear rate, the Si spheres appear to be less sensitive to gravity force due to the chamber being inverted compared to at 200 s^{-1} (Figure 5.7). Inverted the chamber at 200 s^{-1} results in a 55% and 68% decrease in binding of Si spheres in the disturbed region and far downstream, respectively, compared to the upright chamber. At 625 s^{-1}, these decreases in Si adhesion are only 25% and 28%, suggesting that the increased shear makes adhesion less dependent on chamber orientation. The PS particles which are essentially neutrally-buoyant show no dependence on chamber orientation, while the Ti particles only show decreased binding in the far downstream region of the inverted chamber.

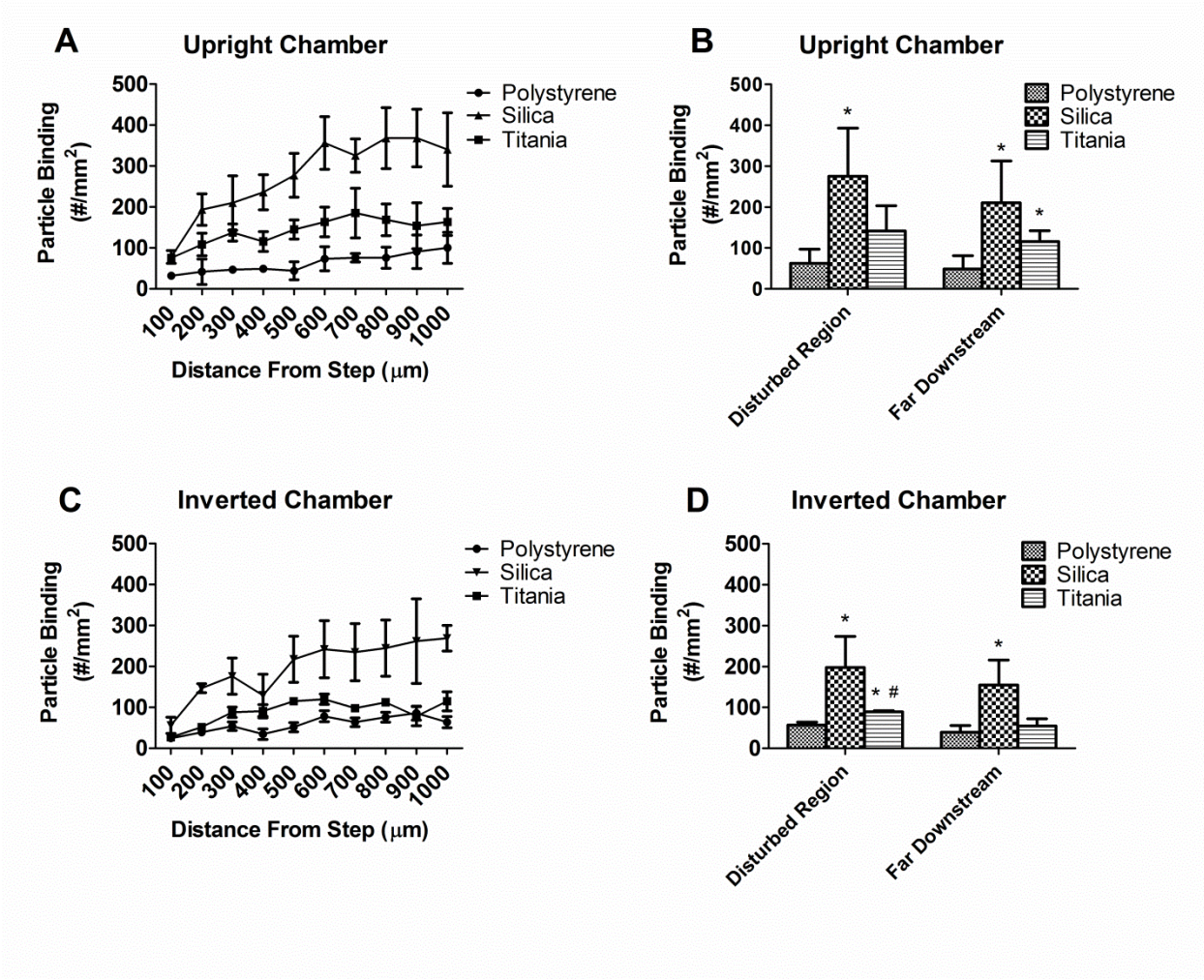

Figure 5.7 Adhesion of sLe^a-coated PS, Si, and Ti spheres (500 nm diameter) to inflamed endothelium after 5 minutes of particle-loaded RBC flow ($5x10^5$ particles/mL total volume) at 625 s^{-1}. Experiments were done in a recirculation flow PPFC setup with the endothelial layer at the bottom (A,B) or top (C,D) of the chamber. A Student t-test was used to compare particle adhesion to *PS adhesion at the same chamber orientation. A p-value < 0.05 was considered statistically significant.

5.3 Discussion

The design of vascular targeted carriers (VTCs) has garnered significant attention recent years because of the potential to achieve highly localized delivery to diseased tissues. It has become clear that the physical parameters, such as particle size and shape, are important in determining the ability of VTC to marginate and adhere to the vascular wall from blood flow.[1–3,5–7,46,47] In light of the wide variety of carrier types proposed, particle density is a relevant parameter to explore for its potential effects on margination and adhesion. Particle density has been shown in simple buffer flow to affect margination[40], however it remains unclear how particle density affects margination in blood flow. Sub-micron sized particles which are neutrally buoyant have been shown to marginate inefficiently in the presence of RBCs, making them sub-optimal as VTCs.[1–3,5–7,46,47] In this work, we attempt to directly compare the margination in blood and adhesion to HUVEC of neutrally buoyant particles with particles that are twice and four times as dense to determine the effect density has on targeting.

The results of this study show that despite having the same coating of targeting ligands, particles of different density display differences in targeting ability in buffer flow and particularly in the presence of RBCs. The fact that we see adhesion increase with particle density in pure buffer flow is an initial indication that gravity may play a role in particle margination at this particle size. This is in contrast to a previous study which showed that in buffer flow, increased density had a negative effect on margination of nanospheres with diameters ranging from 60-65 nanometers.[40] However, these contrasting results are potentially due to the different particle sizes used for experiments. The gravity component for the 65 nm spheres is neglected and the decreased margination is attributed to the increased particle momentum competing with Brownian motion toward the chamber wall. The 500 nm

nanospheres used here will have a larger gravity force, which could contribute to their margination to the bottom of the chamber compared to the smaller (60-65 nm) nanospheres rather than being negligible.

The addition of RBCs results in the increased adhesion of each particle type compared to buffer, which is not surprising, as RBCs are known to improve adhesion kinetics for cells/particles by providing an additional force normal to the endothelium which helps counteract the shear force imparted by blood flow that would act to remove adherent cells from the surface.[48] What we find here, however, is that this RBC effect on adhesion is not the same for particles with different densities, as Si spheres display significantly greater adhesion than either PS or Ti spheres, despite Ti spheres displaying the greatest adhesion in buffer flow. One possibility for this increased adhesion is a difference in the number of particles *localized* to channel wall, providing more particles an opportunity to bind. Indeed, Si spheres on average localized close to the wall in higher amounts than either PS or Ti spheres (though differences were not significantly different). Also, the addition of RBCs elicited increased localization of Si spheres compared to in buffer flow, while RBCs actually decreased the localization of both PS and Ti spheres. Overall, the combination of improved localization along with the RBC-aided adhesion potentially explains why the Si spheres in Figure 5.1B exhibited disproportionately higher adhesion than both PS and Ti spheres. It is known that parameters such as shape, size, and membrane rigidity can affect induced migration of particles/cells in blood; and we see here evidence that density may play a role as well. The question that remains is why are Ti particles exhibiting lower localization (and hence lower adhesion) than Si particles despite their significantly higher density? Recent reports by Kumar and Graham show that heterogeneous collisions between deformable RBCs and more rigid cells and particles contributes to the

margination of such cells/particles to the CFL, where the rigid particles experience a substantial displacement upon collision with the larger deformable RBCs.[49–51] It is possible that density neutral and slightly dense particles such as PS and Si are easily displaced in this manner with the latter of the two experiencing a greater displacement due to larger momentum. However, the Ti particles (which are 4 times as dense) may require larger force from RBC impact to displace it from its original trajectory.

Another possibility is the presence of inertial lift forces acting on particles within microchannel flow. It is well described that even in parallel plate microchannels with relatively low Reynolds numbers, inertial lift forces arising from the parabolic flow profile (as is present in our setup) can result in the lateral migration of particles across streamlines.[52] We suspect that these forces may be at play in our setup, though the situation is made more complex by the presence of RBCs. An estimate of the migration velocity of a particle away from the center of flow can be made using the Equation 5.1:[53]

Equation 5.1 Particle migration velocity due to inertial lift force.

$$U_P = \frac{\rho U_m^2 a^3}{3\pi\mu D_h^2} f_c$$

where U_P is the particle migration velocity, ρ is fluid density, U_m is the maximum channel velocity, a is the particle diameter, μ is fluid viscosity, D_h is the hydraulic diameter, and f_c is a lift coefficient which can be assumed ~0.5 for flow through parallel plates.[53] Using Equation 5.1 and assuming particles in simple buffer flow in our flow chamber at a WSR of 500 s^{-1}, the lateral migration velocity should be on the order of nanometers/sec which seems negligible, however if occurring within the CFL could potentially result in migrations toward the endothelium. Also acting on the particles is a wall induced lift force that acts to push particles away from the wall

when the particle is sufficiently close. Therefore particle motion in the CFL may be governed by a combination on inertial and wall lift force, gravity forces, momentum, and collisions with RBCs acting to keep particles in the CFL. The particle Reynolds number is a metric that can indicate the importance of inertial lift forces in determining particle behavior, which is calculated using Equation 5.2, where ν is the fluid kinematic viscosity.

Equation 5.2 Particle Reynolds number in flow chamber setup

$$R_p = \frac{U_m a^2}{\nu D_h}$$

Particle motion is dominated by inertial lift when the particle Reynolds number is on the order of 1, however in our setup the particle Reynolds number is much less than 1 (as is the case with nanoparticle flow in most microscale channels) suggesting that inertial lift forces may be negligible in this setup[53]. The Stokes number is a metric which will indicate the propensity of particles to move across streamlines, as it compares particle inertia with viscous dissipation via the fluid. The Stokes number is calculated for our situation using Equation 5.3, where ρ_p is the particle density and U is the average velocity of the flow.[54]

Equation 5.3 Stokes number of particle in microchannel flow

$$St = \frac{\rho_p a^2 U}{18 \mu D_h}$$

As particles with different density will have different Stokes numbers, and thus different propensities to move across streamlines, it is possible that particles will have different tendencies to collide with the endothelium once in the CFL (though the Stokes numbers calculated within our channel are still < 1 indicating a propensity to follow streamlines). Overall, it seems the major difference causing differences in adhesion lies with the interactions with RBCs causing

different localization levels to the CFL, while differences in motion once in the CFL may provide an additional impact on the adhesion efficacy.

Another factor to consider is the fact that particles with different density will carry different translational momentum which could affect the ligand/receptor adhesion. We know from previous works that there exists a "critical shear rate" (CSR), above which the resulting particle adhesion decreases with increasing shear rate – due to transition of particle binding into a reaction-limited regime.[3] This CSR is highly dependent on particle diameter, as increasing particle size increases the shear removal force felt by a particle in blood flow. For a given particle size, there is a shear rate above which adhesion is limited by the adhesion kinetics being overwhelmed by the shear removal forces. We see evidence in this work that this CSR may be density-dependent as well. This makes sense, as at a given shear rate and ligand surface coverage, a Ti particle would need to overcome a higher force than a Si particle to firmly adhere. We do see that the adhesion efficiency for both particle types was found to consistently decrease with increasing shear rate, which is likely because of the corresponding increase in translational momentum competing with adhesion forces. Ti particles may be more susceptible to this phenomenon than Si spheres, resulting in the observed difference in apparent CSR. This difference in the adhesion profile for particles with different density is an interesting observation, particularly when considering that the vasculature contains a wide range of local shear rates and blood flow profiles. Thus, it may well be that the optimal targeting of specific areas of the vasculature requires a particle type with a specific density, depending on the local hemodynamics and blood flow profile. It is also important to note that the apparent CSRs observed in this study are specific to the experimental protocol used, and that CSR could change

based on experimental variables that could affect the hemodynamics or reaction kinetics such as targeting ligand density, channel height, hematocrit, flow profile, *etc*.

The addition of centrifugal force via an induced recirculation eddy had noticeable effects on non-neutrally buoyant particles as well, particularly within the disturbed flow region in the immediate vicinity of the recirculation eddy. In a previous work, we use this setup to examine the adhesion pattern of neutrally-buoyant spheres and rods and found no improvement due to shape within the recirculation region (Chapter 3).[7] Interestingly, we do see increased adhesion in this region due to density of these particles. This increase in adhesion is most pronounced when gravity is also acting on the particles in the direction of the HUVEC monolayer. The fact that we still see higher adhesion of Si and Ti particles compared to PS in the disturbed region with gravity opposite the direction of the HUVEC suggests that the presence of the recirculation eddy is causing increased redistribution of Si and Ti particles to the CFL and thus the HUVEC monolayer. This observation is further supported by the observation that non-neutrally buoyant particles exhibit increased adhesion in the recirculation flow compared to laminar flow (comparing Figure 5.5 to Figure 5.6). In an inverted channel, this effect is diminished in the far downstream region – showing that gravity effects still persist. By increasing the shear rate (Figure 5.7), thus increasing the contribution due to centrifugal force, we find the adhesion of Si spheres is significantly less dependent on chamber orientation. The results in this study suggest that the combination of particle density-dependent gravity and centrifugal forces can both affect localization and subsequent adhesion to the endothelium depending on local hemodynamics, which vary drastically depending on which area of the vasculature is targeted.

This study shows evidence that particle density may be a useful parameter for optimizing the performance of vascular-targeted carriers. In this study the densities investigated range from

1.05 - 3.9 g/cm^3, however the density range of proposed drug carriers is even wider. Buoyant microbubbles as well as high density metal based particles including iron oxide (~5 g/cm^3) and gold (~19 g/cm^3). The wide range of particle densities along with tunable particle shape, size, and surface properties provides a vast parameter space which can be explored to improve site specific targeting.

References

1. Tilles, A. W. & Eckstein, E. C. The near-wall excess of platelet-sized particles in blood flow: its dependence on hematocrit and wall shear rate. *Microvasc. Res.* **33,** 211–223 (1987).

2. Eckstein, E. C., Tilles, A. W. & Millero 3rd, F. J. Conditions for the occurrence of large near-wall excesses of small particles during blood flow. *Microvasc Res* **36,** 31–39 (1988).

3. Charoenphol, P., Huang, R. B. & Eniola-Adefeso, O. Potential role of size and hemodynamics in the efficacy of vascular-targeted spherical drug carriers. *Biomaterials* **31,** 1392–1402 (2010).

4. Charoenphol, P. *et al.* Targeting therapeutics to the vascular wall in atherosclerosis-Carrier size matters. *Atherosclerosis* **217,** 364–370 (2011).

5. Namdee, K., Thompson, A. J., Charoenphol, P. & Eniola-Adefeso, O. Margination propensity of vascular-targeted spheres from blood flow in a microfluidic model of human microvessels. *Langmuir* **29,** 2530–2535 (2013).

6. Namdee, K. *et al.* In vivo evaluation of vascular-targeted spheroidal microparticles for imaging and drug delivery application in atherosclerosis. *Atherosclerosis* **237,** 279–286 (2014).

7. Thompson, A. J., Mastria, E. M. & Eniola-Adefeso, O. The margination propensity of ellipsoidal micro/nanoparticles to the endothelium in human blood flow. *Biomaterials* **34,** 5863–5871 (2013).

8. Lee, T.-R. *et al.* On the near-wall accumulation of injectable particles in the microcirculation: smaller is not better. *Sci. Rep.* **3,** 2079 (2013).

9. Eniola-Adefeso, O., Heslinga, M. J. & Porter, T. M. Design of nanovectors for therapy and imaging of cardiovascular diseases. *Methodist Debakey Cardiovasc J* **8,** 13–17 (2012).

10. Unger, E., Porter, T., Lindner, J. & Grayburn, P. Cardiovascular drug delivery with ultrasound and microbubbles. *Adv. Drug Deliv. Rev.* **72,** 110–126 (2014).

11. Ting, C. Y. *et al.* Concurrent blood-brain barrier opening and local drug delivery using drug-carrying microbubbles and focused ultrasound for brain glioma treatment. *Biomaterials* **33,** 704–712 (2012).

12. Bull, J. L. The application of microbubbles for targeted drug delivery. *Expert Opin. Drug Deliv.* **4,** 475–493 (2007).

13. Nance, E. *et al.* Brain-Penetrating Nanoparticles Improve Paclitaxel Efficacy in Malignant Glioma Following Local Administration. *ACS Nano* (2014). doi:10.1021/nn504210g

14. Shuvaev, V. V. *et al.* Endothelial targeting of antibody-decorated polymeric filomicelles. *ACS Nano* **5,** 6991–6999 (2011).

15. Kamaly, N., Xiao, Z., Valencia, P. M., Radovic-Moreno, A. F. & Farokhzad, O. C. Targeted polymeric therapeutic nanoparticles: design, development and clinical translation. *Chem. Soc. Rev.* **41,** 2971 (2012).

16. Muro, S. *et al.* Endothelial targeting of high-affinity multivalent polymer nanocarriers directed to intercellular adhesion molecule 1. *J. Pharmacol. Exp. Ther.* **317,** 1161–1169 (2006).

17. Allen, T. M. Long-circulating (sterically stabilized) liposomes for targeted drug delivery. *Trends Pharmacol. Sci.* **15,** 215–220 (1994).

18. Allen, T. M. & Cullis, P. R. Liposomal drug delivery systems: From concept to clinical applications. *Adv. Drug Deliv. Rev.* **65,** 36–48 (2013).

19. Liong, M. *et al.* Multifunctional inorganic nanoparticles for imaging, targeting, and drug delivery. *ACS Nano* **2,** 889–896 (2008).

20. Huang, H.-C., Barua, S., Sharma, G., Dey, S. K. & Rege, K. Inorganic nanoparticles for cancer imaging and therapy. *J. Control. Release* **155,** 344–57 (2011).

21. Park, J. H. *et al.* Magnetic Iron Oxide Nanoworms for Tumor Targeting and Imaging. *Adv Mater* **20,** 1630–1635 (2008).

22. Samokhin, G., Smirnov, M., Muzykantov, V., Domogatsky, S. & Smirnov, V. Effect of flow rate and blood cellular elements on the efficiency of red blood cell targeting to collagen-coated surfaces. *J. Appl. Biochem.* **6,** 70–75 (1984).

23. Muzykantov, V. R. Drug delivery by red blood cells: vascular carriers designed by Mother Nature. *Expert Opin. Drug Deliv.* **7,** 403–427 (2011).

24. Park, J. Il *et al.* Microbubbles loaded with nanoparticles: A route to multiple imaging modalities. *ACS Nano* **4,** 6579–6586 (2010).

25. Anselmo, A. C. & Mitragotri, S. Cell-mediated delivery of nanoparticles: Taking advantage of circulatory cells to target nanoparticles. *J. Control. Release* (2014). doi:10.1016/j.jconrel.2014.03.050

26. Geers, B. *et al.* Self-assembled liposome-loaded microbubbles: The missing link for safe and efficient ultrasound triggered drug-delivery. *J. Control. Release* **152,** 249–256 (2011).

27. Lee, S. Y., Ferrari, M. & Decuzzi, P. Shaping nano-/micro-particles for enhanced vascular interaction in laminar flows. *Nanotechnology* **20,** 495101 (2009).

28. Jurney, P. *et al.* The Effect of Nanoparticle Size on Margination and Adhesion Propensity in Artificial Micro-Capillaries. *Proc. Asme Micro/Nanoscale Heat Mass Transf. Int. Conf. 2012* 109–115 (2012). at <<Go to ISI>://WOS:000324346800015>

29. Migliorini, C. *et al.* Red blood cells augment leukocyte rolling in a virtual blood vessel. *Biophys. J.* **83,** 1834–1841 (2002).

30. Nash, G. B., Watts, T., Thornton, C. & Barigou, M. Red cell aggregation as a factor influencing margination and adhesion of leukocytes and platelets. in *Clin. Hemorheol. Microcirc.* **39,** 303–310 (2008).

31. Nobis, U., Pries, A. R., Cokelet, G. R. & Gaehtgens, P. Radial distribution of white cells during blood flow in small tubes. *Microvasc Res* **29,** 295–304 (1985).

32. Nicolas, J., Mura, S., Brambilla, D., Mackiewicz, N. & Couvreur, P. Design, functionalization strategies and biomedical applications of targeted biodegradable/biocompatible polymer-based nanocarriers for drug delivery. *Chem. Soc. Rev.* **42,** 1147–235 (2013).

33. Petros, R. A. & DeSimone, J. M. Strategies in the design of nanoparticles for therapeutic applications. *Nat. Rev. Drug Discov.* **9,** 615–627 (2010).

34. Parveen, S., Misra, R. & Sahoo, S. K. Nanoparticles: A boon to drug delivery, therapeutics, diagnostics and imaging. *Nanomedicine Nanotechnology, Biol. Med.* **8,** 147–166 (2012).

35. Muro, S. *et al.* Control of endothelial targeting and intracellular delivery of therapeutic enzymes by modulating the size and shape of ICAM-1-targeted carriers. *Mol Ther* **16,** 1450–1458 (2008).

36. Muro, S. Challenges in design and characterization of ligand-targeted drug delivery systems. *J. Control. Release* **164,** 125–37 (2012).

37. Adriani, G. *et al.* The preferential targeting of the diseased microvasculature by disk-like particles. *Biomaterials* **33,** 5504–5513 (2012).

38. Chacko, A. M., Hood, E. D., Zern, B. J. & Muzykantov, V. R. Targeted nanocarriers for imaging and therapy of vascular inflammation. *Curr. Opin. Colloid Interface Sci.* **16,** 215–227 (2011).

39. Gentile, F., Curcio, A., Indolfi, C., Ferrari, M. & Decuzzi, P. The margination propensity of spherical particles for vascular targeting in the microcirculation. *J. Nanobiotechnology* **6,** 9 (2008).

40. Toy, R., Hayden, E., Shoup, C., Baskaran, H. & Karathanasis, E. The effects of particle size, density and shape on margination of nanoparticles in microcirculation. *Nanotechnology* **22,** 115101 (2011).

41. Polanowskagrabowska, R., Raha, S. & Gear, A. R. L. Adhesion Efficiency, Platelet Density and Size. *Br. J. Haematol.* **82,** 715–720 (1992).

42. Doshi, N. & Mitragotri, S. Designer biomaterials for nanomedicine. *Adv. Funct. Mater.* **19,** 3843–3854 (2009).

43. Malek, A. M., Alper, S. L. & Izumo, S. Hemodynamic shear stress and its role in atherosclerosis. *JAMA* **282,** 2035–2042 (1999).

44. Nguyen, N. D. & Haque, A. K. Effect of hemodynamic factors on atherosclerosis in the abdominal aorta. *Atherosclerosis* **84,** 33–39 (1990).

45. Charoenphol, P., Onyskiw, P. J., Carrasco-Teja, M. & Eniola-Adefeso, O. Particle-cell dynamics in human blood flow: implications for vascular-targeted drug delivery. *J Biomech* **45,** 2822–2828 (2012).

46. Charoenphol, P. *et al.* Targeting therapeutics to the vascular wall in atherosclerosis--carrier size matters. *Atherosclerosis* **217,** 364–370 (2011).

47. Lee, T. R. *et al.* On the near-wall accumulation of injectable particles in the microcirculation: smaller is not better. *Sci Rep* **3,** 2079 (2013).

48. Migliorini, C. *et al.* Red blood cells augment leukocyte rolling in a virtual blood vessel. *Biophys. J.* **83,** 1834–1841 (2002).

49. Kumar, A. & Graham, M. D. Mechanism of margination in confined flows of blood and other multicomponent suspensions. *Phys. Rev. Lett.* **109,** (2012).

50. Kumar, A. & Graham, M. D. Margination and segregation in confined flows of blood and other multicomponent suspensions. *Soft Matter* **8,** 10536 (2012).

51. Kumar, A. & Graham, M. D. Segregation by membrane rigidity in flowing binary suspensions of elastic capsules. *Phys. Rev. E - Stat. Nonlinear, Soft Matter Phys.* **84,** (2011).

52. Di Carlo, D. Inertial microfluidics. *Lab Chip* **9,** 3038–3046 (2009).

53. Di Carlo, D., Irimia, D., Tompkins, R. G. & Toner, M. Continuous inertial focusing, ordering, and separation of particles in microchannels. *Proc. Natl. Acad. Sci. U. S. A.* **104,** 18892–18897 (2007).

54. Wu, Z., Willing, B., Bjerketorp, J., Jansson, J. K. & Hjort, K. Soft inertial microfluidics for high throughput separation of bacteria from human blood cells. *Lab Chip* **9,** 1193–1199 (2009).

CHAPTER 6: IN VIVO TARGETING AND BIODISTRIBUTION OF TARGETED SUB-MICRON SPHERES OF DIFFERENT MATERIAL AND DENSITY

ABSTRACT

We have seen *in vitro* that particle density, as with particle size and shape, can affect the margination and adhesion of vascular-targeted carriers in the presence of red blood cells. Naturally, it is of interest whether these effects will translate to better targeting ability in the more complex *in vivo* environment, which will include interactions with blood plasma, white blood cells, and platelets. Also, the hemodynamic conditions throughout the vasculature vary dramatically, which may affect the areas in which particles of different density are best suited for targeting. In this study, vascular-targeted PS, Si, and Ti spheres with 500 nm diameter are administered to mice with systemic inflammation; and the ability to target inflamed aorta is compared. Also, biodistribution studies are performed to determine in which major organs the targeted or non-targeted particles tend to accumulate. We find that on average, Si spheres adhere to inflamed aorta at higher levels than either PS or Ti spheres. Specifically, we find Si (and in some regions Ti) spheres bound at significantly higher levels compared to PS at upper segments of the aorta including the aortic arch, brachiocephalic artery, left common carotid artery – areas characterized by complex hemodynamics and known to be prone to atherosclerosis.

Further down the aorta, we find similar adhesion of PS and Si spheres while Ti sphere adhesion was minimal. Non-targeted control particles displayed no adhesion to the aorta, demonstrating the targeting specificity of the ligands used. Non-targeted and targeted particles of all types accumulated in significant amounts in the liver and spleen, while only targeted particles displayed significant accumulation in the lungs – consistent with targeting to systemic inflammation.

6.1 Introduction

A wide variety of material types are proposed for use as vascular targeted carriers. As such, it is of interest to investigate how different carrier types behave *in vivo* due to their physical characteristics. We have shown *in vitro* that particle density may have an effect on overall targeting ability due to density-dependent forces in flow and particle/RBC interactions. It is then of interest as to whether these effects will remain evident in a more complex physiological environment. In addition to interacting with RBCs, particles *in vivo* are also be subject to opsonization of plasma proteins, interactions with circulating phagocytes, and innate filtration mechanisms which would remove foreign particles from circulation.[1–6] Also, the local hemodynamics vary drastically throughout the vasculature.[7] The vessel diameter, vessel branching, local shear rate, hematocrit, and flow type (steady, pulsatile, oscillating) can be quite different depending on which area of the vasculature is being targeted, and these parameters all have been shown to have effects on the ability of particles to adhere to endothelium.

Many different types of vascular-targeted vehicles for drug delivery or imaging have been tested for their efficacy in targeting diseased tissue *in vivo*, including microbubbles[8–10], liposomes[11–13], polymer nanoparticles[14–16], dendrimers[17–19], and inorganic nanoparticles[20,21]. Often, studies have compared the targeting ability of vascular-targeted particles to non-targeted control particles, displaying the efficacy of the targeting system; or have compared the efficacy of drug-loaded particle administration to that of free-drug administration to show improved treatment with targeted drug-loaded particles. Polymeric and inorganic particles have been tested in vascular-targeting studies *in vivo*[22–27]; however to our knowledge, no studies have been done to compare how these particles target and biodistribute with focus on different particle density. We have shown previously that PS spheres with 500 nm diameters do not adhere as

efficiently as microparticles in a mouse model of atherosclerosis[15,28] following the same trend observed for the same particles binding *in vitro* in human blood[29–31]. In this study, we investigate whether more dense particles are more effective at adhering to inflamed aorta compared to PS spheres, which have density very close to that of blood. Using a mouse model of systemic inflammation, polystyrene (PS), silica (Si), and titania (Ti) particles dual-targeted to E-selectin and VCAM-1 are administered to compare directly the ability of particles having different densities to target inflammation *in vivo*. Specifically we look for differences in adhesion along sections of the aorta, as well as biodistribution in major organs.

6.2 Results

Vascular-targeted PS, Si and Ti nanospheres were prepared and injected into wild-type male mice at 20 weeks of age as previously described.[15,28] Briefly, targeted particles are surface coated with sLe^a and anti-VCAM-1 to target E-selectin and VCAM-1, respectively, and non-targeted control particles are coated with a non-specific isotype control antibody. Wild-type mice are pre-treated with TNF-α for 24 hours to induce systemic inflammation. Particles are then administered via tail-vein injection and allowed to circulate for 30 min before mice are sacrificed. The aorta is isolated and imaged to quantify the adhesion density along each section of the aorta. Also, the lung, liver, spleen, and kidney are harvested to quantify biodistribution in major organs.

6.2.1 Particle Adhesion to Inflamed Mouse Aorta

Figure 6.1 shows the adhesion level of dual-targeted PS, Si, and Ti spheres to whole mice aortae. Similar to the trends seen in the *in vitro* assays, Si spheres adhered to whole mouse aortae at significantly higher levels than PS spheres. The adhesion of Ti and PS spheres were not significantly different, despite the Ti spheres displaying enhanced adhesion compared to PS

under certain conditions *in vitro*. Spheres coated with an isotype control antibody did not adhere at any appreciable level for all particle types investigated, displaying the targeting specificity of the ligands used.

Figure 6.2 shows the adhesion normalized to the area of various sections of the aorta, and Figure 6.3 shows the overall particle adhesion (not normalized) to each section of the aorta. The adhesion pattern for the different particles varies along different sections of the aortic tree. Si spheres display significantly greater adhesion density (normalized to the area of each section) than PS spheres particularly in the "upper" segments of the aorta. The aortic arch and first major branchings, including the brachiocephalic artery (and subsequent right common carotid and right subclavian) and left common carotid artery, which are known to be particularly prone to atherosclerosis[28], all display significantly more adhesion of Si particles than PS. The thoracic aorta and abdominal branches also display higher Si binding, while in the "lower" segments of the descending aorta ending with the iliac branches, the PS and Si adhesion are not different and the adhesion of Ti was significantly lower. On average, we see a higher normalized adhesion for PS and Si spheres near the aortic bifurcation and iliac arteries at the terminal end of the aorta compared to the ascending aorta and the thoracic and abdominal segments of the descending aorta.

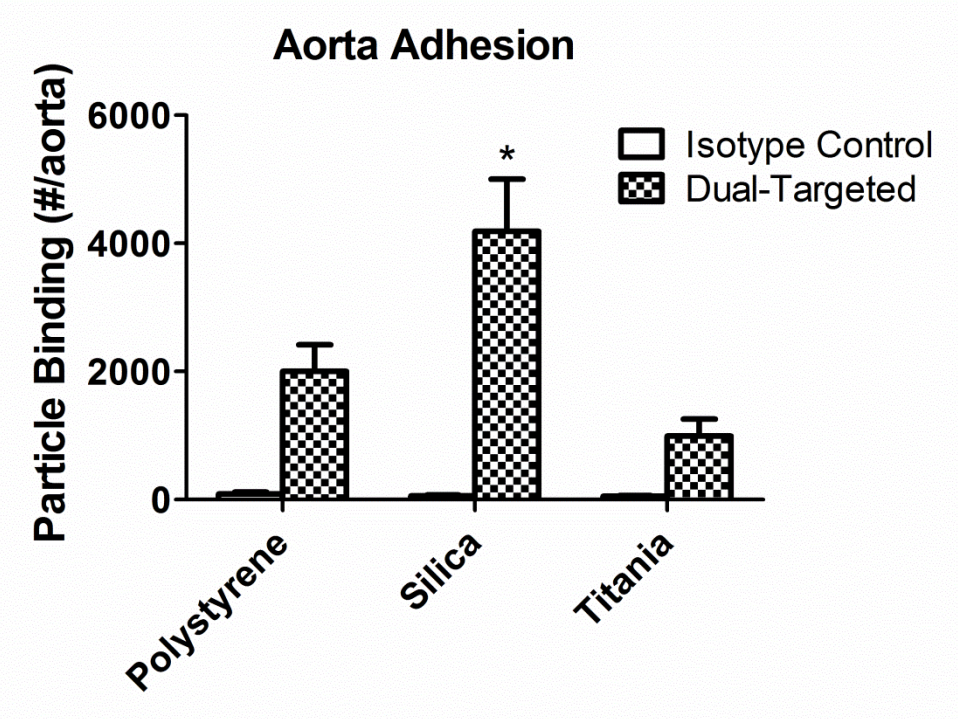

Figure 6.1 Adhesion of dual-targeted or isotype control PS, Si and Ti spheres to the inflamed aorta of wild-type mice pretreated with TNF-α cytokine for 24 hours. Particles were injected via tail-vein ($4x10^7$ particles/mouse) and allowed to circulate for 30 mins. One-way ANOVA with Bonferroni post-test was used to compare particle adhesion to *PS adhesion at the same chamber orientation. A p-value < 0.05 was considered statistically significant.

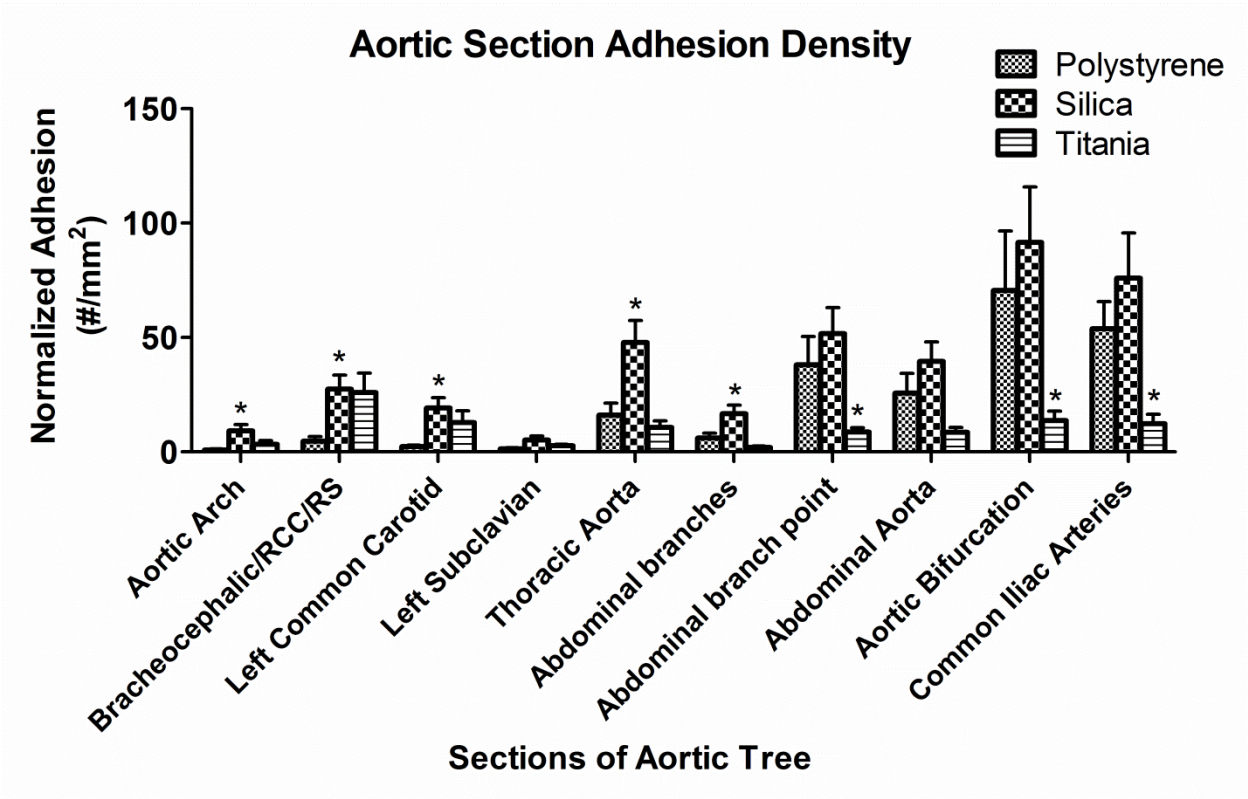

Figure 6.2 Normalized adhesion density of dual-targeted or isotype control PS, Si and Ti spheres to each section of the inflamed aorta of wild-type mice pretreated with TNF-α cytokine for 24 hours. Particles were injected via tail-vein ($4x10^7$ particles/mouse) and allowed to circulate for 30 mins. One-way ANOVA with Bonferroni post-test was used to compare particle adhesion to *PS adhesion at the same chamber orientation. A p-value < 0.05 was considered statistically significant.

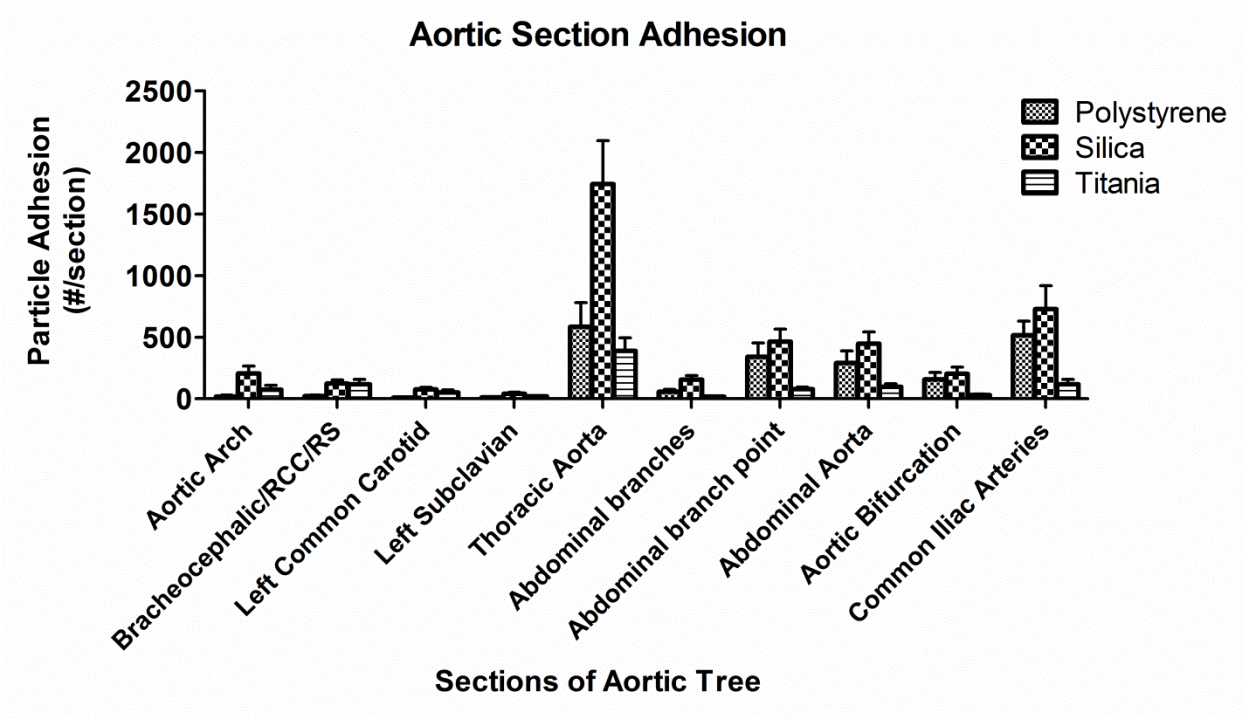

Figure 6.3 Average particle adhesion of dual-targeted or isotype control PS, Si and Ti spheres to each section of the inflamed aorta of wild-type mice pretreated with TNF-α cytokine for 24 hours. Particles were injected via tail-vein ($4x10^7$ particles/mouse) and allowed to circulate for 30 mins. One-way ANOVA with Bonferroni post-test was used to compare particle adhesion to *PS adhesion at the same chamber orientation. A p-value < 0.05 was considered statistically significant.

6.2.2 Particle Biodistribution in Major Organs

Figure 6.4 and Figure 6.5 show the biodistribution of targeted and non-targeted PS, Si, and Ti spheres to major organs (lung, kidney, spleen and liver) in inflamed wild-type mice. We find that presence of targeting ligands on the particles results in increased accumulation of all particle types in the lungs compared to the isotype control, likely due to molecular interaction of the targeted particles with inflamed endothelium in the lung microvasculature. Both targeted and non-targeted particles displayed minimal accumulation in the kidney, which is expected since these particles are larger than what is typically removed from the blood via glomerular filtration. The spleen and liver predictably show significant particle accumulation. Targeted Si spheres accumulated less in the spleen and liver than non-targeted Si, however, this specific trend is not apparent for PS or Ti particles. Still, we find in the absence of targeting molecules, the majority of each of the particles end up in organs of the RES (liver and spleen).

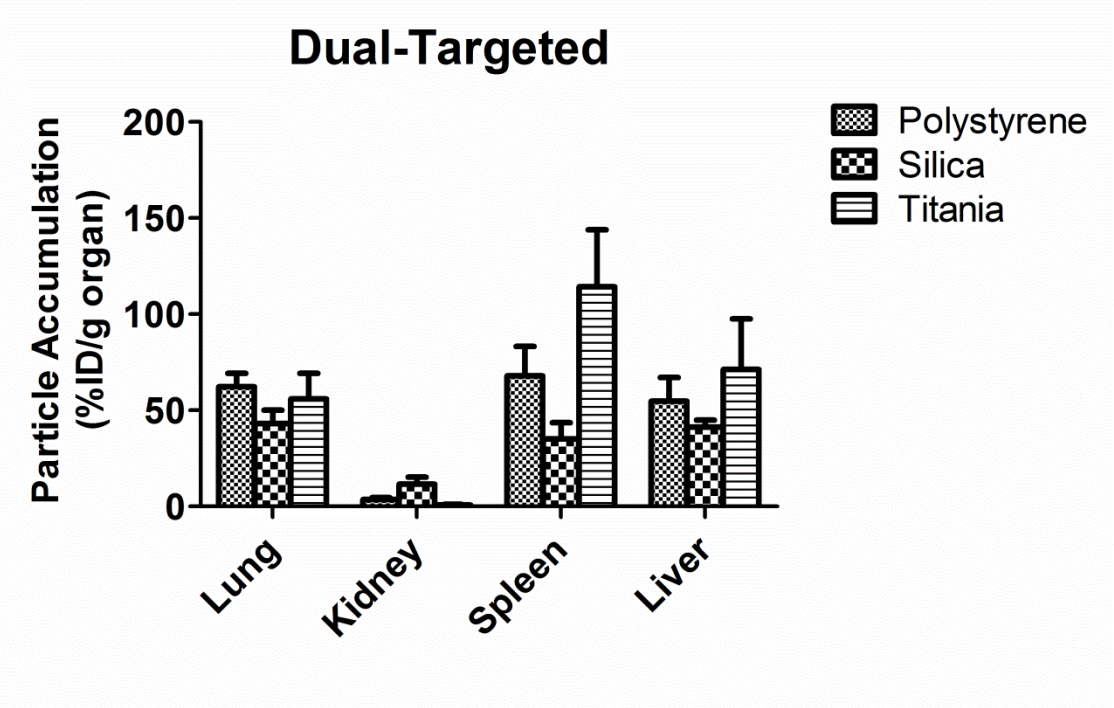

Figure 6.4 Accumulation in major organs of dual-targeted PS, Si, and Ti particles with 500 nm ESD. Accumulation is plotted as % injected dose per gram organ.

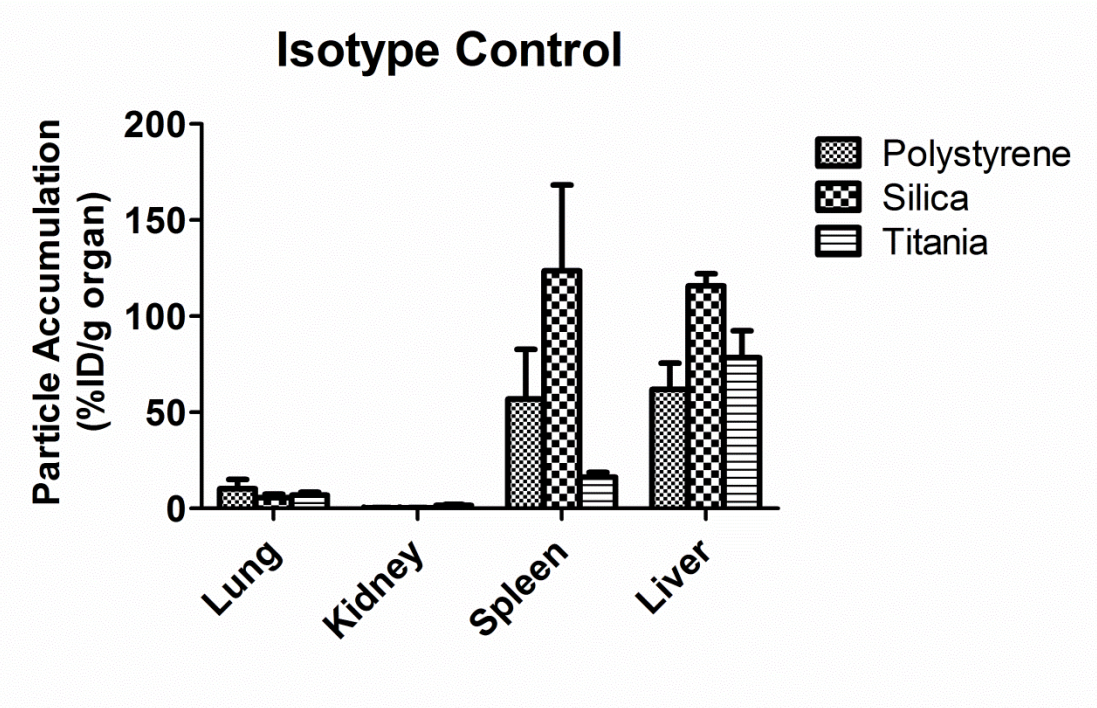

Figure 6.5 Accumulation in major organs of isotype control IgG coated PS, Si, and Ti particles with 500 nm ESD. Accumulation is plotted as % injected dose per gram organ.

6.3 Discussion

The adhesion trends seen in the *in vitro* assays shown in Chapter 5 translated reasonably well to the *in vivo* environment, as Si spheres adhered to inflamed mouse aorta at higher levels than either PS or Ti spheres. The differences in the adhesion patterns of particles along the aorta are potentially linked to the hemodynamic conditions and vessel diameter in each section. For instance, dense particles displayed greater adhesion in the upper segments of the aorta with high curvature and shear rates, potentially aided by additional centrifugal forces improving particle margination as was seen in *in vitro* recirculation assays. Neutrally-buoyant PS particles display low binding density in this area, unaffected by density-dependent forces and less likely to bind in a vessel with large diameter and high peak shear. However, we do see a higher normalized adhesion for PS and Si spheres near the terminal end of the aorta compared to in the upper segments of the aorta (a result that has been observed previously for PS spheres)[32]. It is possible that particles of this size are more likely to adhere in the lower aorta sections where the vessel diameters are smaller and peak shear rates are lower, resulting result in the observed increase in adhesion near the iliacs.[7,32] Aside from in the brachiocephalic (and subsequent right carotid and subclavian artery) and left common carotid sections, we see minimal adhesion of Ti spheres throughout the rest of the aorta. It is possible that Ti spheres have difficulty adhering in areas of the aorta characterized by more continuous laminar shear, while still able to bind in the two sections where high vessel curvature is present. Also there is the possibility that plasma protein absorption may negatively affect Ti particle adhesion, as particles of different material may attract different types/amounts of plasma proteins.[33]

The observed accumulation of targeted particles in the lung is unsurprising, as inflammation will also be present on lung endothelium as well as the aorta. Also, the lungs are

the site of the highest density of capillaries within the vasculature, providing a large area for particle adhesion in vessels which are favorable for adhesion. The results shown here follow previous research which also shows the enhanced accumulation of inflammation-targeting particles in the lungs when systemic inflammation is present.[15,34] Without the presence of the targeting ligand, the particles show minimal accumulation in the lung, as they are small enough to navigate the capillary beds without mechanical entrapment.

Regardless of particle type or surface coating, a large portion of the dosage ends up in organs of the RES (liver and spleen). Similar results have been shown *in vivo* for similar particles made from the same materials used in this study.[6,35–43] We see clearly that targeted Si spheres accumulated less in the spleen and liver than non-targeted Si, likely due to the increased adhesion on the aorta, in the lung, and elsewhere in the vasculature. However, it is unclear why this trend is not apparent for PS or Ti spheres. A previous work shows that silica and titania particles show distinct differences in the plasma protein corona that forms when introduced to plasma despite displaying similar surface charge/zeta potential.[33] Since specific opsonins are known to affect biodistribution and may enhance/diminish uptake by organs of the RES, it is possible that the different particle types may attract protein coronas with enough variation to shift the biodistribution profiles, despite the particle surfaces being saturated with the same ligands.[6] Still, the biodistribution of non-targeted Ti particles follows what was previous shown for titania particles of comparable size injected into rats[36] and mice[35], where the majority of the dose is retained in the liver, followed by the spleen, lung, and kidney.

Overall, the presented *in vivo* data also suggests with a better understanding of the local hemodynamics *in vivo* at a specific target site and the implications of material type on

biodistribution, there is opportunity to use carrier density and material type as tools for improving disease targeting specificity.

References

1. Allen, T. M. & Cullis, P. R. Drug delivery systems: entering the mainstream. *Science* **303,** 1818–1822 (2004).

2. Sanhai, W. R., Sakamoto, J. H., Canady, R. & Ferrari, M. Seven challenges for nanomedicine. *Nat. Nanotechnol.* **3,** 242–244 (2008).

3. Pantic, I. Nanoparticles and modulation of immune responses. *Sci. Prog.* **94,** 97–107 (2011).

4. Stolnik, S., Illum, L. & Davis, S. S. Long circulating microparticulate drug carriers. *Adv. Drug Deliv. Rev.* **64,** 290–301 (2012).

5. Li, S. D. & Huang, L. Pharmacokinetics and biodistribution of nanoparticles. in *Mol. Pharm.* **5,** 496–504 (2008).

6. Aggarwal, P., Hall, J. B., McLeland, C. B., Dobrovolskaia, M. A. & McNeil, S. E. Nanoparticle interaction with plasma proteins as it relates to particle biodistribution, biocompatibility and therapeutic efficacy. *Adv. Drug Deliv. Rev.* **61,** 428–437 (2009).

7. Huo, Y., Guo, X. & Kassab, G. S. The flow field along the entire length of mouse aorta and primary branches. *Ann. Biomed. Eng.* **36,** 685–699 (2008).

8. Weller, G. E. R. *et al.* Ultrasound imaging of acute cardiac transplant rejection with microbubbles targeted to intercellular adhesion molecule-1. *Circulation* **108,** 218–224 (2003).

9. Andonian, S., Coulthard, T., Smith, A. D., Singhal, P. S. & Lee, B. R. Real-time quantitation of renal ischemia using targeted microbubbles: in-vivo measurement of P-selectin expression. *J. Endourol.* **23,** 373–378 (2009).

10. Schumann, P. A. *et al.* Targeted-microbubble binding selectively to GPIIb IIIa receptors of platelet thrombi. *Invest. Radiol.* **37,** 587–593 (2002).

11. Hirai, M. *et al.* Accumulation of liposome with Sialyl Lewis X to inflammation and tumor region: Application to in vivo bio-imaging. *Biochem. Biophys. Res. Commun.* **353,** 553–558 (2007).

12. Gabizon, A. *et al.* In Vivo Fate of Folate-Targeted Polyethylene-Glycol Liposomes in Tumor-Bearing Mice. *Clin. Cancer Res.* **9,** 6551–6559 (2003).

13. Allen, T. M. & Cullis, P. R. Liposomal drug delivery systems: From concept to clinical applications. *Adv. Drug Deliv. Rev.* **65,** 36–48 (2013).

14. Yu, D. H., Lu, Q., Xie, J., Fang, C. & Chen, H. Z. Peptide-conjugated biodegradable nanoparticles as a carrier to target paclitaxel to tumor neovasculature. *Biomaterials* **31,** 2278–2292 (2010).

15. Namdee, K. *et al.* In vivo evaluation of vascular-targeted spheroidal microparticles for imaging and drug delivery application in atherosclerosis. *Atherosclerosis* **237,** 279–286 (2014).

16. Danhier, F. *et al.* Targeting of tumor endothelium by RGD-grafted PLGA-nanoparticles. *Methods Enzymol.* **508,** 157–175 (2012).

17. Konda, S. D., Aref, M., Wang, S., Brechbiel, M. & Wiener, E. C. Specific targeting of folate-dendrimer MRI contrast agents to the high affinity folate receptor expressed in ovarian tumor xenografts. *MAGMA* **12,** 104–113 (2001).

18. Singh, P., Gupta, U., Asthana, A. & Jain, N. K. Folate and folate-PEG-PAMAM dendrimers: Synthesis, characterization, and targeted anticancer drug delivery potential in tumor bearing mice. *Bioconjug. Chem.* **19,** 2239–2252 (2008).

19. Chandrasekar, D., Sistla, R., Ahmad, F. J., Khar, R. K. & Diwan, P. V. The development of folate-PAMAM dendrimer conjugates for targeted delivery of anti-arthritic drugs and their pharmacokinetics and biodistribution in arthritic rats. *Biomaterials* **28,** 504–512 (2007).

20. Reuveni, T., Motiei, M., Romman, Z., Popovtzer, A. & Popovtzer, R. Targeted gold nanoparticles enable molecular CT imaging of cancer: an in vivo study. *Int. J. Nanomedicine* **6,** 2859–2864 (2011).

21. Benezra, M. *et al.* Multimodal silica nanoparticles are effective cancer-targeted probes in a model of human melanoma. *J. Clin. Invest.* **121,** 2768–2780 (2011).

22. Passarella, R. J. *et al.* Targeted nanoparticles that deliver a sustained, specific release of paclitaxel to irradiated tumors. *Cancer Res.* **70,** 4550–4559 (2010).

23. Muro, S. *et al.* Control of endothelial targeting and intracellular delivery of therapeutic enzymes by modulating the size and shape of ICAM-1-targeted carriers. *Mol. Ther.* **16,** 1450–1458 (2008).

24. Muro, S. *et al.* Endothelial targeting of high-affinity multivalent polymer nanocarriers directed to intercellular adhesion molecule 1. *J. Pharmacol. Exp. Ther.* **317,** 1161–1169 (2006).

25. Kumar, A., Zhang, X. & Liang, X.-J. Gold nanoparticles: emerging paradigm for targeted drug delivery system. *Biotechnol. Adv.* **31,** 593–606 (2013).

26. Shao, X. *et al.* 125I-labeled gold nanorods for targeted imaging of inflammation. *ACS Nano* **5,** 8967–8973 (2011).

27. Akerman, M. E., Chan, W. C. W., Laakkonen, P., Bhatia, S. N. & Ruoslahti, E. Nanocrystal targeting in vivo. *Proc. Natl. Acad. Sci. U. S. A.* **99,** 12617–12621 (2002).

28. Charoenphol, P. *et al.* Targeting therapeutics to the vascular wall in atherosclerosis--carrier size matters. *Atherosclerosis* **217,** 364–370 (2011).

29. Charoenphol, P., Huang, R. B. & Eniola-Adefeso, O. Potential role of size and hemodynamics in the efficacy of vascular-targeted spherical drug carriers. *Biomaterials* **31,** 1392–1402 (2010).

30. Namdee, K., Thompson, A. J., Charoenphol, P. & Eniola-Adefeso, O. Margination propensity of vascular-targeted spheres from blood flow in a microfluidic model of human microvessels. *Langmuir* **29,** 2530–2535 (2013).

31. Thompson, A. J., Mastria, E. M. & Eniola-Adefeso, O. The margination propensity of ellipsoidal micro/nanoparticles to the endothelium in human blood flow. *Biomaterials* **34,** 5863–5871 (2013).

32. Charoenphol, P. *et al.* Targeting therapeutics to the vascular wall in atherosclerosis-Carrier size matters. *Atherosclerosis* **217,** 364–370 (2011).

33. Deng, Z. J. *et al.* Differential plasma protein binding to metal oxide nanoparticles. *Nanotechnology* **20,** 455101 (2009).

34. Muro, S. *et al.* Control of endothelial targeting and intracellular delivery of therapeutic enzymes by modulating the size and shape of ICAM-1-targeted carriers. *Mol Ther* **16,** 1450–1458 (2008).

35. Xie, G., Wang, C., Sun, J. & Zhong, G. Tissue distribution and excretion of intravenously administered titanium dioxide nanoparticles. *Toxicol. Lett.* **205,** 55–61 (2011).

36. Fabian, E. *et al.* Tissue distribution and toxicity of intravenously administered titanium dioxide nanoparticles in rats. *Arch. Toxicol.* **82,** 151–157 (2008).

37. Xie, G., Sun, J., ZhonG., G., Shi, L. & ZhanG., D. Biodistribution and toxicity of intravenously administered silica nanoparticles in mice. *Arch. Toxicol.* **84,** 183–190 (2010).

38. Landsiedel, R. *et al.* Toxico-/biokinetics of nanomaterials. *Arch. Toxicol.* **86,** 1021–1060 (2012).

39. Umbreit, T. H. *et al.* Tissue distribution and histopathological effects of titanium dioxide nanoparticles after intravenous or subcutaneous injection in mice. *J. Appl. Toxicol.* **32,** 350–357 (2012).

40. Decuzzi, P. *et al.* Size and shape effects in the biodistribution of intravascularly injected particles. *J. Control. Release* **141,** 320–7 (2010).

41. Huang, X. *et al.* The shape effect of mesoporous silica nanoparticles on biodistribution, clearance, and biocompatibility in vivo. *ACS Nano* **5,** 5390–5399 (2011).

42. He, Q., Zhang, Z., Gao, F., Li, Y. & Shi, J. In vivo biodistribution and urinary excretion of mesoporous silica nanoparticles: Effects of particle size and PEGylation. *Small* **7,** 271–280 (2011).

43. Cho, M. *et al.* The impact of size on tissue distribution and elimination by single intravenous injection of silica nanoparticles. *Toxicol. Lett.* **189,** 177–183 (2009).

CHAPTER 7: CONCLUSIONS AND FUTURE DIRECTIONS

7.1 Conclusions

Improving and optimizing the design of vascular-targeted carriers is important as this technology moves forward toward widespread clinical use. Physical characteristics including size, shape, density, surface coating, rigidity, etc. must all be considered, as each can potentially be a tool for improving targeting performance. In addition, the hemodynamics and vessel geometry present in the must be considered, as targeting to various areas throughout the vasculature will likely require unique particle types with specific physical characteristics for optimal targeting. In this work we find that particle shape and particle density both can affect the performance of VTCs in blood flow.

In Chapter 3 we find a coupled effect of particle shape and size in determining the adhesion efficiency of targeted particles in the presence of RBCs. We find that within the parameter space investigated, particle size remains an important factor in determining particle localization and adhesion as, other parameters equal, 2 μm ESD particles display more adhesion than 500 nm or 1 μm ESD particles regardless of shape. However, particle shape can indeed to be used to improve adhesion compared to an equivalent spherical particle, given that the particle volume and particle aspect ratio are both of sufficient magnitude. Both rod and disk shaped particles with ESD $\geq$ 1 μm displayed improved adhesion compared to equivalent spheres, though

particles 500 nm ESD remain limited by their ability to localize to the CFL in the presence of RBCs.

In Chapter 4, we find that that the trends observed in Chapter 3 translate to improved plaque targeting ability *in vivo* using a mouse model of atherosclerosis. The targeting ability of 500 nm ESD rods and spheres are limited by their size (thus inefficient margination), while particles with 2 μm ESD display significantly higher compared to smaller particles. We find that 2 μm rods with AR4 adhere to plaques significantly more than equivalent spheres, demonstrating their superior utility as a vascular-targeted carrier towards atherosclerosis. We also find, however, that the improved adhesion also translates to increased accumulation of rods in the lungs due to systemic inflammation, noting the need for careful choice of specific targeting ligands to prevent unwanted delivery away from the target site.

In Chapter 5, we see that particle density affects the adhesion of nanoparticles (500 nm diameter) in both buffer flow and in the presence of RBCs. Silica spheres, which have a density roughly twice that of blood, exhibit improved adhesion to inflamed endothelium compared to polystyrene or titania spheres in the presence of RBCs, regardless of the direction in which gravity is acting. Titania spheres (4 times more dense than blood) adhere at levels higher than polystyrene, but only in conditions when gravity or centrifugal force acts in the direction of adhesion. As expected, neutrally-buoyant polystyrene spheres appear to be unaffected by density-dependent forces.

In Chapter 6, we find that the results obtained in Chapter 5 translate reasonably well to an *in vivo* mouse model of systemic inflammation. Overall, silica spheres displayed increased adhesion to inflamed aorta compared to polystyrene or titania spheres. Titania spheres also

displayed increased adhesion compared to PS in specific sections of the aorta, while displaying significantly less adhesion toward the terminal end of the aorta, potentially related to the different hemodynamic conditions present in these areas. Particles targeted toward inflammation display enhanced accumulation in the lungs due to molecular interactions, while a significant portion in the targeted and non-targeted dosage accumulates in the spleen and liver.

In conclusion, we find that along with particle size, particle shape and density are indeed parameters which should be considered when designing vascular-targeted carriers. By optimizing the physical characteristics of VTCs, we can improve the treatment and diagnosis of many diseases by providing highly localized, highly site-specific delivery. With a robust understanding the effects that physical parameters have on targeting, we may be able to eventually provide disease-specific or even patient-specific vascular-targeted carrier systems.

7.2 Future Directions

In light of the results presented in this dissertation and the current state of the field of vascular-targeting, there are several areas of interest for further research to help drive the improvement of vascular-targeted carriers.

(1) Explore the vastly wider parameter space in terms of particle shape and density. Advancements in fabrication methods provide the ability to produce monodisperse populations of a various particle shapes which could produce differences in adhesion patterns. Non-spherical particles with high relatively density, such as gold nanorods or carbon nanotubes, can also be investigated since theoretically the lateral drift magnitude for such particles should be higher than for neutrally-buoyant particles. Direct comparisons between particles of equivalent volume or shape are important to determine which physical parameters are most important in prescribing targeting efficacy.

(2) Identify whether the adhesion of differently shaped particles is affected by plasma protein interactions. It is known that surface curvature can elicit different responses in terms of plasma protein corona, however, how these differences affect active targeting remains unclear. This may also have implications on the long term fate of particles administered *in vivo*, after the initial margination/adhesion step has occurred.

(3) Compare the effects of particle size/shape/density for particles with ESD in the range of tens of nanometers. It has been shown that large nanoparticles and sub-micron particles can be inhibited by the presence of the RBC core, preventing their accumulation in the CFL. However, by definition, the CFL is a region of highly enriched plasma. Therefore, by using very small particle sizes, it is possible that

particles can then behave as soluble molecules, possibly also becoming enriched in the CFL region rather than being inhibited by RBC core entrapment.

(4) Specifically match numerous hemodynamic conditions *in vitro* to specific sites within the *in vivo* vasculature, in order to assess the extent to which different areas of the vasculature will require a carrier with different physical characteristics to result in optimal targeting. In this way we can move toward predetermining what carrier design will be ideal for targeting a specific disease or possibly within a specific patient.

(5) Investigate the ability to direct post-adhesion outcome of vascular-targeted carriers on a longer time scale. By using a continuous, closed system experimental setup, an *in vitro* model of the vasculature can be used to identify the ability of targeted carriers to persist on the endothelium, become internalized, deliver relevant drug concentrations, etc, in the presence of physiological shear. These *in vitro* results can then be compared to *in vivo* findings in which the time-dependent outcome of VTC administration is investigated.